EVALUATION OF MINIMUM MISCIBILITY PRESSURE AND EFFECTIVE DIFFUSION COEFFICIENTS FOR DESIGN OF GAS ASSISTED RECOVERY IN UNCONVENTIONAL LIQUID-RICH SHALE RESERVOIRS

A Thesis

by

RAYSHA ALIFFA PRAWIRA

Submitted to the Office of Graduate and Professional Studies of
Texas A&M University
in partial fulfillment of the requirements for the degree of

MASTER OF SCIENCE

Chair of Committee,	Maria A. Barrufet
Committee Members,	David S. Schechter
	Thomas A. Blasingame
Head of Department,	Jeff Spath

May 2021

Major Subject: Petroleum Engineering

ABSTRACT

In recent years, the rapid decline in the production trend of liquid-rich shale reservoirs calls attention to enhance oil recovery (EOR) methods. One of the most promising EOR methods in unconventional reservoirs is a miscible gas injection with soaking, but this requires a more extensive reservoir fluid characterization than for conventional reservoirs to consider the confined behavior of fluids in nanopores. The Peng-Robinson Equation of State (PR-EOS) is coupled with the Young-Laplace capillary pressure model to include the nanopore confinement effect into the fluid behavior model. The study's general objective is to predict the performances of different gas-assisted EOR methods in unconventional liquid-rich reservoirs with a more compatible and reliable thermodynamic-based model. We extend the features of in-house developed pressure-volume-temperature (PVT) simulator to calculate minimum miscibility pressure (MMP), an essential property to design a miscible gas injection, and to model a gas injection process by molecular diffusion using the appropriate effective diffusion coefficient in a tight-shale oil reservoir.

Previous work on conventional reservoirs has proven that injecting at or above the MMP can significantly increase recovery. However, the nanopore confinement effect in MMP estimation has not been well-documented, and there is no consensus in the modeling approaches. Numerical MMP estimation is more computationally efficient than molecular simulation and produces faster results than laboratory experiments. In this study, we developed an MMP calculation that includes the nanopore confinement effect. Since phase equilibria calculations have been coupled to the Young-Laplace capillary pressure model, a feasible MMP calculation method for this study is the Multiple-Mixing Cells method that calls for flash

calculations for each of the mixing cells to obtain dynamic multiple-contact miscibility. MMP predictions without confinement effect were compared with results from a commercial PVT simulator to test the accuracy. After modifying the MMP calculation, we examined multiple MMP estimations with varying fluid components, pore sizes, and reservoir conditions.

Other than fluid miscibility, the flow mechanism in unconventional ultralow permeability plays dominated by molecular diffusion significantly impacts oil production from gas-assisted recovery process. To simulate this, we need to select the appropriate effective diffusion coefficient. We solved the diffusion equation with and without the swelling-induced convection term numerically in the PVT simulator. The oil production was calculated based on the excess swollen volume of the solvent-oil mixture. Then, we matched the recovery factor with the existing experimental data by adjusting the effective diffusion coefficient. Thus, this study provides a tool that can describe the recovery process quantitatively and qualitatively.

ACKNOWLEDGEMENTS

I would first like to thank my advisor and a great mentor, Dr. Maria Barrufet for introducing me and piquing my interest into reservoir fluids study during my undergraduate study and for her full support, patience, guidance, and expertise during my graduate study. She would always find the time to help and advise throughout my study. Her encouragements have pushed me to keep learning and improving.

I would also like to thank my committee members. I am blessed to attend courses taught by Dr. Thomas Blasingame for the in-depth lectures, insights, and setting the standards in work. I would also thank Dr. David Schechter for his time and expertise in the research projects related to this thesis and his research group in supporting the data for this thesis.

I would thank to all the faculties, professors, and staff at Texas A&M University, especially in the Department of Petroleum Engineering, for providing me the hub for great sources of knowledge through the courses, seminars, curriculums, and organizations.

I would like to thank Crisman Institute for Petroleum Research for funding my graduate study and for providing the opportunity in the development of this research.

Last but foremost, I would like to thank my family for their endless support and prayers throughout my studies.

CONTRIBUTORS AND FUNDING SOURCES

Contributors

This thesis was supervised by committee members consisting of Professor Maria A. Barrufet of the Department of Petroleum Engineering and the Department of Chemical Engineering, Dr. David Schechter of Department of Petroleum Engineering, and Dr. Thomas A. Blasingame of the Department of Petroleum Engineering and Department of Geology.

Funding Sources

This research and my graduate study were generously supported through graduate research assistantship from Department of Petroleum Engineering and the Crisman Institute for Petroleum Research.

NOMENCLATURE

Symbols	Definition
A^j	Polynomial EOS constant of phase *j*
a_i	EOS attraction parameter of component *i*, ft^6 psi/$lbmol^2$
$a\alpha^j$	EOS attraction parameter of phase *j*, ft^6 psi/$lbmol^2$
B^j	Polynomial EOS constant of phase *j*
b_i	EOS co-volume parameter of component *i*, ft^3/lbmol
b^j	EOS co-volume parameter of phase *j*, ft^3/lbmol
c	Concentration of solvent in liquid phase (mol/cm^3)
c_i	Initial concentration of solvent in liquid phase (mol/cm^3)
c_0	Concentration of solvent in liquid phase at the interface (mol/cm^3)
D	Binary diffusion coefficient in liquid phase, cm^2/s
D_{eff}	Pseudo-binary effective diffusion coefficient in liquid phase in porous medium, cm^2/s
D_{ij}	Diffusion coefficient in liquid phase of solute *i* and solvent *j*, cm^2/s
d	Pore diameter, nm
f	Swelling factor
f_i^j	Fugacity of component *i* in phase *j*, psia
h	Height of porous media, cm
J	Diffusive flux mol/(m^2-s)
K_i	Vapor-liquid equilibrium constant (K-value)
M_i	Molar mass of component *i*, lbm/lbmol
M^j	Molar mass of phase *j*, lbm/lbmol
N	Number of contacts
n	Number of moles, mg-mol
N_c	Number of components
N_{cell}	Number of cells for discretization
p_{cap}	Capillary pressure, psia

P_i	Parachor of component i, dyne$^{1/E}$ cm$^{3-1/E}$/gmol
p^j	Pressure of phase j, psia
$p_{c,i}$	Critical pressure of component i, psia
R	Gas constant, 10.731 ft^3 psi/lbmol R
r	Pore radius, nm (for EOS) or radial distance, cm (for diffusion)
r_i	Spherical radius of solute i, cm
r_0	Reference radius of a porous medium, cm
s_i	Volume shift parameter of component i
T	Temperature, °F
$\mathcal{I}L$	Tie-line length
$T_{c,i}$	Critical temperature of component i, °F
$T_{r,i}$	Reduced temperature of component i
t	Time, s
u	Velocity in r or x directions (cm/s)
V_m^j	Molar volume of phase j, ft^3/lbmol
$\tilde{V}_m^j$	Corrected molar volume of phase j, ft^3/lbmol
$V_{s,total}$	Total oil-solvent mixture volume expanded in a porous medium, cm^3
$V_{sol,stored}$	Volume of solvent stored in the matrix, cm^3
V_p	Pore volume, cm^3
w	Width of a porous medium, cm
x	Distance in porous medium, cm
$\bar{x}$	Dimensionless distance in porous medium
x_0	Reference length of a porous medium, cm
x_i	Liquid mole fraction of component i (for EOS)
x_i^j	Mole fraction of component i in phase j (for EOS)
y_i	Vapor mole fraction of component i (for EOS)
Z^j	Compressibility factor of phase j
$Z_{c,i}$	Critical compressibility factor of component i
z_i	Overall mole fraction of component i

Greek Symbols	**Definition**
α_i	EOS scaling factor
β	Fraction of total moles in vapor phase

δ_{ik}	Binary interaction parameter between components i and j
ΔV_e	Volume expansion of the oil phase (cm^3)
ε	Diffusive tortuosity of porous medium
η_j	Viscosity of solvent j, cP
θ	Contact angle, degrees
κ_i	EOS characteristic constant of component i
$\tilde{\rho}^j$	Corrected mass density of phase j, lbm/ft^3
σ	Interfacial tension, dyne/cm
τ	Dimensionless time
ϕ	Porosity of the porous medium
$\hat{\phi}_i^j$	Fugacity coefficient of component i in phase j
ϕ_j	Single component fugacity coefficient of phase j
ψ_i^j	EOS mixture parameter of component i in phase j, ft^6 $psi/lbmol^2$
ω_i	Acentric factor of component i

Subscripts	**Definition**
g	Gas phase
i	Cell i (for diffusion)
k	Component k
max,prod	Solvent-oil mixture at its maximum solvent concentration
o	Oil phase
oil,inital	Initial amount of original oil
oil,prod	Original oil produced
res	Reservoir condition
SC	Standard condition
sol,prod	Solvent produced

Superscripts	**Definition**
j	Phase j
l	Liquid phase
v	Vapor phase

Abbreviations	**Definition**
EOS	Equation of state

GOR	Gas-oil ratio, SCF/STB
MMP	Minimum miscibility pressure, psia
PR	Peng-Robinson
PVT	Pressure-volume-temperature
SCF	Standard cubic feet
STB	Stock tank barrel
VLE	Vapor-liquid equilibrium

TABLE OF CONTENTS

Page

LIST OF FIGURES

Page

LIST OF TABLES

Page

CHAPTER I

INTRODUCTION

Since the innovation of horizontal and multilateral well technology combined with multistage hydraulic fracturing in the late 1990s the oil and gas industry in the United States can now effectively produce from shale reservoirs with nano-scale pore sizes. With the price drop in natural gas in 2008, the focus has shifted from shale gas to shale oil reservoirs. However, this poses new challenges in the engineering practices in the oil and gas industry. The production trend in shale oil reservoirs declines more rapidly than in conventional reservoirs and can become uneconomical within three years or less. To increase the recovery factor, mature fields in conventional reservoirs have adopted enhanced oil recovery (EOR) methods using solvent gas injection. The application of EOR on shale oil reservoirs, however, still requires more research and has very limited field data.

In the EOR design plan, reservoir fluid study is a crucial component. However, the fluid behavior model that has been used in conventional reservoirs cannot accurately describe the fluid behavior in unconventional oil reservoirs. Although some empirical methods are practical to specific cases, a more reliable physics-based model is needed to predict the solvent gas injection performance. The most common approaches to examine fluid phase behavior are laboratory experiments and simulation. We focus on the latter.

One of the most successful EOR methods in conventional reservoirs is miscible gas injection. Injecting gas at or above the minimum miscibility pressure (MMP) has

shown higher oil recovery than injecting below the MMP in conventional reservoirs. Thus, the MMP prediction is important for optimization. Although numerical MMP prediction methods have been well-studied in conventional reservoirs, the nanopore confinement in shale reservoir can alter the MMP estimation. This study involves adding the MMP calculation feature into our in-house PVT simulator applicable for fluids in bulk and confined spaces and observing the deviation in MMP results in confinement.

While miscibility is achieved, the recovery mechanism needs to be evaluated. The highly heterogenous and ultra-low permeability reservoir changes the dynamics between fluid-rock interactions and fluid-fluid interactions where Darcy's Law assumptions are no longer applicable. One of the violations is that the dominant flow is not a function of pressure gradient (convective). Thus, molecular diffusion becomes the main recovery mechanism in the matrix of shale reservoir. The diffusion process for gas injection design in a tight-shale reservoir can be simulated. The problem is in measuring an effective (or equivalent) diffusion coefficient to solve the diffusion-convection equation. Diffusion coefficients can mostly be obtained through laboratory experiments that are not compatible for tight oil reservoirs because they are usually done under low pressure and would require a long time to get sufficient data (Jia et al. 2019). Tovar et al. (2018a) conducted core flooding experiments that mimic the gas huff-n-puff injection on a hydraulically fractured rock. Therefore, we suggest a different method to find the effective diffusion coefficient.

This study is an attempt to analyze the performance of various scenarios of gas-assisted recovery in tight oil reservoirs. The analysis includes the effect of reservoir and

injection fluid components, fracture spacing, and injection mode on oil production. These factors may change the MMP and the effective diffusion coefficient prediction. The focus of this study is to improve the capabilities of our PVT simulator particularly for EOR projects in tight reservoirs. The outcome of this research is to assist in designing EOR projects in liquid-rich shale reservoirs.

1.1 Research Objectives

The overall objective of this study is to evaluate the performance of gas-assisted recovery methods in unconventional liquid-rich reservoirs using the calibrated fluid phase behavior model. Our goal is to create a mechanistic predictive model with a minimum number of adjustable parameter but physically verifiable. We utilize the coupled equation of state (EOS) to include the nanopore confinement effect in this study. To satisfy the main objective, we:

1. Develop an algorithm to calculate the minimum miscibility pressure (MMP) for fluids under bulk condition and confinement
2. Simulate the diffusion-convection process with an effective (gas-oil) diffusion coefficient to estimate oil production in low permeability porous media
3. Validate the estimated MMP and the effective diffusion coefficient with published experimental data
4. Provide analyses on various injection schemes with the estimated parameters mentioned above and their impact on the oil recovery

1.2 Description of Chapters

Chapter I states the problem and the research objectives.

Chapter II summarizes the published literature on the current progress within the topic of gas-assisted recovery projects in unconventional reservoirs. It starts from the broader topic of unconventional reservoir to the specific topic of fluid transport and phase behavior.

Chapter III discusses the theoretical background the driving mechanism of multiple-contacts miscibility and the MMP estimation method. The discussion of the results from the MMP estimation simulation is included in this chapter.

Chapter IV includes the theoretical background of Fickian diffusion and the oil expansion effect (swelling) to the diffusion model used in the study. The discussion of the results from the simulation of the diffusion process is included in this chapter.

Chapter V covers the validity and the practical application of the MMP calculation and the diffusion model.

Chapter VI consists of composition of the fluids mentioned in the thesis and the binary interaction coefficients.

Chapter VII explains the conclusions and future work recommendations.

CHAPTER II

LITERATURE REVIEW

2.1 Unconventional Reservoirs

Since the rise in horizontal drilling technology and multi-stage hydraulic fracturing in the early 2000's, the rock commonly known as source rock could become a reservoir rock. This type of reservoir is an unconventional reservoir because it requires the assistance of specific recovery techniques to be produced at economic rates. There are several types of unconventional reservoirs, including coalbed methane, heavy oil, gas hydrates, and tight oil and gas shale reservoirs. In this study, we focus on tight oil-rich reservoirs. Tight oil shale reservoir is a type of sedimentary rock with ultra-low matrix permeability in nanodarcies scale, low matrix porosity, very heterogenous, and usually high total organic content (TOC). The most productive tight oil reservoirs in the United States are the Permian Basin, Eagle Ford shale in Western Gulf Basin, and Bakken shale in Williston Basin. In 2019, Eagle Ford Shale play alone had 4.3 billion barrels of tight oil proved reserves and approximately contributed 20% of the U.S. crude oil production from tight plays (EIA 2019). These basins usually come from marine depositional environment and are shaped like the source rocks as shown in **Fig. 2. 1** with discontinuous producible layers and natural fractures. The natural fractures and the laminated rock type contribute to the high heterogeneity, which is one of the challenges in predicting the recovery in unconventional reservoirs. Other challenges may include the tackling the low recovery factor, predicting the complex fracture geometry, and optimizing completion method.

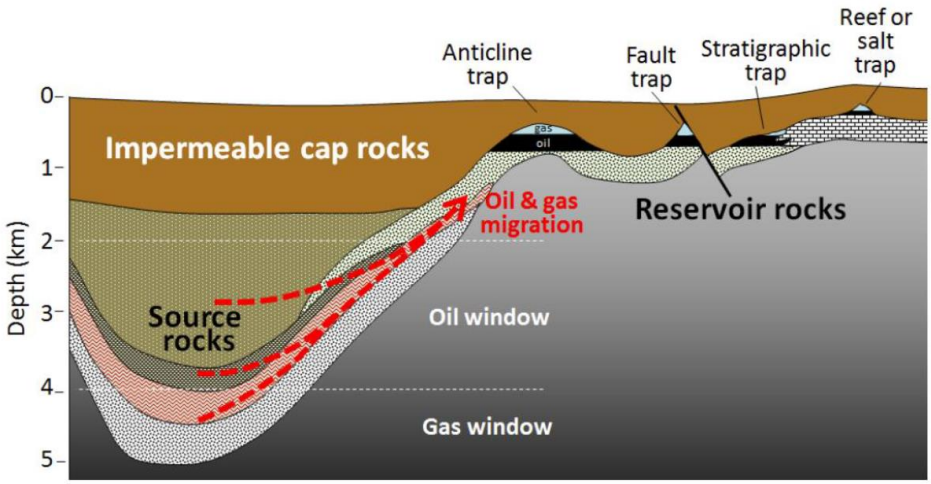

Fig. 2. 1—The difference between source rock and reservoir rock in a petroleum play. Reprinted from *Physical Geology* by Earle (2015), licensed under CC BY-4.0.

2.2 Enhanced Oil Recovery in Tight Oil Reservoirs

One of the problems in unconventional reservoirs are the low recovery factor and short production life. The attention has shifted to Enhanced oil recovery (EOR) projects to solve the problem in unconventional reservoirs. Many EOR projects have been tested on conventional reservoirs for several decades. According to Jia et al. (2019), the best EOR scheme for ultra-low permeability shale reservoir with matrix permeability smaller than 0.01 millidarcy is the huff-n-puff gas injection scheme. The huff-n-puff method utilizes a single well for injection and production. It requires a soaking period in each injection cycle that allows the gas to enter the matrix. Meanwhile, continuous gas flooding restricts the gas to penetrate into the matrix from the fracture network and leads to early gas breakthrough.

In addition to the challenges in predicting recovery performance in unconventional reservoirs, the transport phenomena and phase behavior of the solvent and reservoir fluid in tight porous media are not well understood. Historically, miscible injection is favorable in conventional reservoirs. Multiple-contact miscibility between the solvent and oil occurs at a certain pressure and temperature. Therefore, estimating MMP is a crucial step to ensure miscible injection occurs.

While the solvent gas and oil could be miscible or form a single phase in the overall compositions, their rate of mixing within the matrix is governed by diffusive transport in tight permeability rocks. The limiting assumptions of Darcy's Law cannot be applied in unconventional reservoirs due to the very low matrix permeability and heterogeneity. This condition causes the flow velocity to be significantly lower than for the convective flow which is no longer the dominant recovery mechanism. In fractured tight-oil reservoirs, convective flow still occurs in the fracture system while molecular diffusion happens predominantly within the matrix system. The connectivity between the fracture and the matrix also poses more uncertainty on the solvent-oil interaction. The natural fractures can increase the surface area for the diffusion process to take place from the fracture to the matrix.

2.2.1 Gas Injection to Improve Oil Recovery

This research focuses on gas injection methods to improve oil recovery. In conventional reservoirs, several gas injection methods that have been proven to successfully increase the ultimate recovery in the field, including continuous, water-

alternating-gas, and huff-n-puff schemes. Some of the common solvents used in the field are carbon dioxide (CO_2), nitrogen (N_2), methane (CH_4), hydrocarbon-rich gas, or a mixture of these components. Most of the successful gas injection projects are under miscible state that can be achieved through multiple-contacts between the solvent gas and the oil. Achieving a fully-miscible state promotes swelling of the oil volume and lowering the oil viscosity. In fractured tight oil reservoirs, the solvent diffuses into the fractures from pressure gradient and into the matrix from concentration gradient, as depicted in **Fig. 2. 2**. Ideally, the solvent expands the oil volume and produces the excess from the diffusion process.

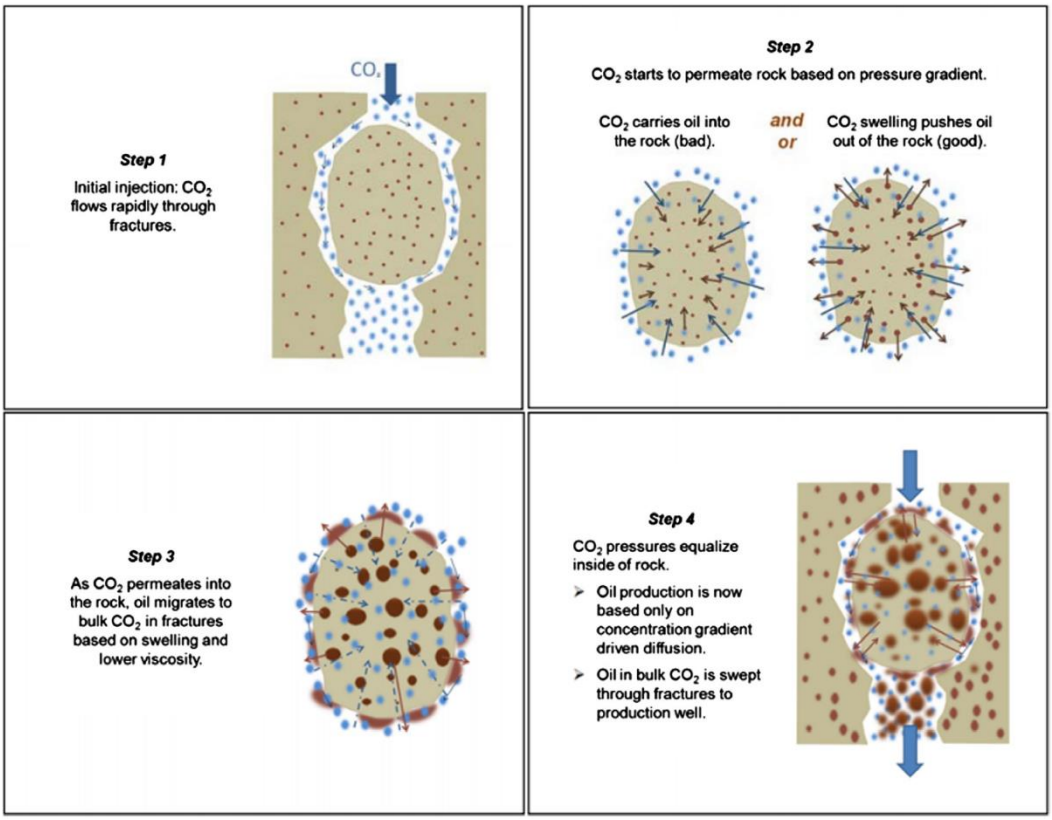

Fig. 2. 2—Solvent injection process through the fractures using CO_2 as the solvent. Reprinted from *Hydrocarbon Mobilization Mechanisms from Upper, Middle, and Lower Bakken Reservoir Rocks Exposed to CO_2* by Hawthorne et al. (2013).

2.3 Thermodynamics in Confined Spaces

Confinement changes the fluid phase behavior from its bulk state, especially in nanoscale pore size. Molecular simulations have shown the confinement effect in nanoscale pore radius where bubble point pressure is suppressed and heavier components are increased (Baek & Akkutlu 2019; Zhang et al. 2016). Stimpson and Barrufet (2016) also found that there was a phase envelope suppression under confinement based on our PVT Simulator results. This suppression means that liquid saturation is higher, leading to higher oil production in unconventional liquid reservoirs (Stimpson & Barrufet 2016).

Given their analysis, hypothetically, the MMP is most likely be lower with lower bubble-point pressure under confinement.

Leverett (1941) analyzed static equilibrium and dynamic flow of immiscible fluids in porous media caused by capillary forces. Stimpson (2017) added the nanopore confinement model into our existing PVT simulator. Peng-Robinson Equation of State model is coupled with the Young-Laplace capillary pressure model. **Fig. 2. 3** shows the capillary pressure equation. Pore size and contact angle, or wettability, are additional input parameters needed in the PVT simulator to include the confinement effect. The modification lies in the fugacity equation, where the liquid and vapor pressure are not the same under confinement. The vapor pressure becomes the sum of liquid pressure and capillary pressure, as shown in **Fig. 2. 3**. The vapor-liquid equilibrium calculation procedure with the capillary pressure model increases the complexity and computational effort because it requires a longer iterative process. This study aims to improve the existing PVT simulator and expand this work specifically to be applied in enhanced oil recovery projects.

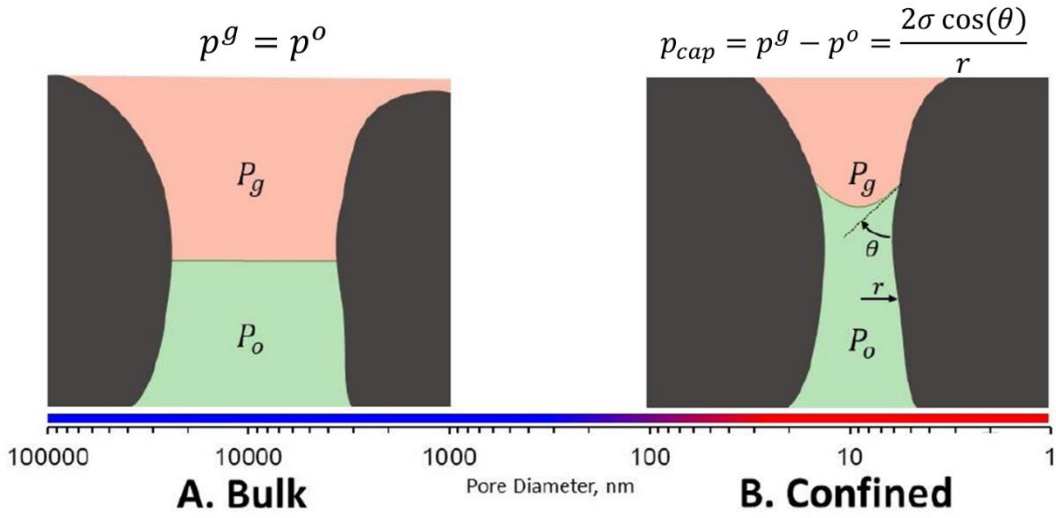

Fig. 2. 3—The difference between bulk and confined pore throat filled with gas in red and oil in green. Reprinted from a thesis by Czernia (2018).

2.3.1 Nanopore Confinement Effect on Fluid Properties

In addition to analysis by Stimpson (2017), this chapter includes a brief analysis of the effect of nanopore confinement by coupling the capillary pressure equation with the Peng-Robinson equation of state with volume translation. It entails the deviation of K-values, liquid and gas phase fraction, densities, and viscosities in confined state from bulk condition. The fluid properties in confinement prove that the liquid composition becomes lighter and enriched with lighter components and that the gas composition becomes slightly heavier under confinement. This phenomenon causes a decrease in liquid density and viscosity and an increase in gas density and viscosity. It can be explained by the K-values and liquid and gas mole fraction of the components of the fluid. The fluid used in this analysis is found from the literature and is listed in **Table 6. 4**, which is a simplified version of Eagle Ford volatile oil from **Table 6. 3** to emphasize hydrocarbon components. We use an in-house PVT Simulator to run flash calculations to obtain the equilibrated

fluid properties. This analysis consistently uses 10 nm of pore diameter and 30° of contact angle for the confined case. We use unit slope as a reference to visualize the deviation in confined fluid properties from the bulk state.

In **Fig. 2. 4**, liquid densities in confined state are lower while gas densities in confined state are higher than those in bulk state at pressures of 500, 1,000, and 1,500 psia and at a temperature of 250°F. **Fig. 2. 5** shows that liquid viscosities are lower in confined state while gas viscosities are higher in confined state than those in bulk state at all pressures. Lower liquid density and liquid viscosity for fluid in confinement imply that the liquid becomes lighter and contains more lighter components under confinement. On the other hand, the higher gas density and gas viscosity for fluid in confinement signify that the gas composition becomes enriched with heavier components. To support this observation, we inspect K-values and liquid and gas mole fraction of each component.

We compare K-values and liquid and gas mole fraction of each fluid component from **Table 6. 4** at 500 psia and 1,500 psia and a temperature of 250°F. **Fig. 2. 6** and **Fig. 2. 7** show the K-values for fluid in bulk and confined state at 1,500 psia and 500 psia, respectively. The K-values in confinement deviates more from the bulk state at lower pressure, as depicted in Figure 4, because capillary pressure is higher at lower oil pressure of 500 psia. Both figures show that the changes in K-values are more significant on lighter components and that K-values are lower under confinement. The lower K-values could be caused by either increasing liquid mole fraction, x_i, or decreasing gas mole fraction, y_i. **Fig. 2. 7** indicates that K-values are lower on lighter components and slightly higher on heavier components for fluid under confinement, revealing the slightly increasing gas

viscosity and gas density with confinement. **Fig. 2. 8** and **Fig. 2. 9** show gas and liquid mole fraction of each component in fluid from Table 6. 4 at pressures of 1,500 psia and 500 psia, respectively. As seen in both figures, the gas mole fraction of each component under confinement does not deviate from the unit slope as much as the liquid mole fraction. Therefore, the liquid composition is more affected by nanopore confinement than gas composition. **Fig. 2. 9** signifies that there are more lighter hydrocarbons and less heavier hydrocarbons in liquid composition in confinement. This phenomenon explains decreasing liquid density and liquid viscosity in confinement, as seen in **Fig. 2. 4** and **Fig. 2. 5**.

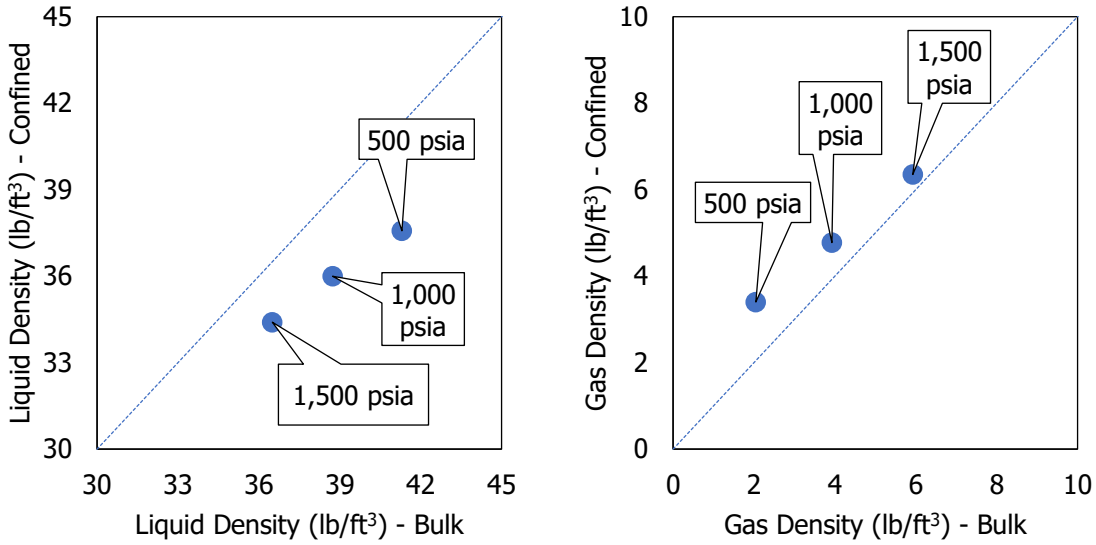

Fig. 2. 4—Liquid and gas density of simplified fluid in Table 6. 4 for bulk and confined condition at 250°F. Confined case has 10 nm of pore diameter and 30° contact angle.

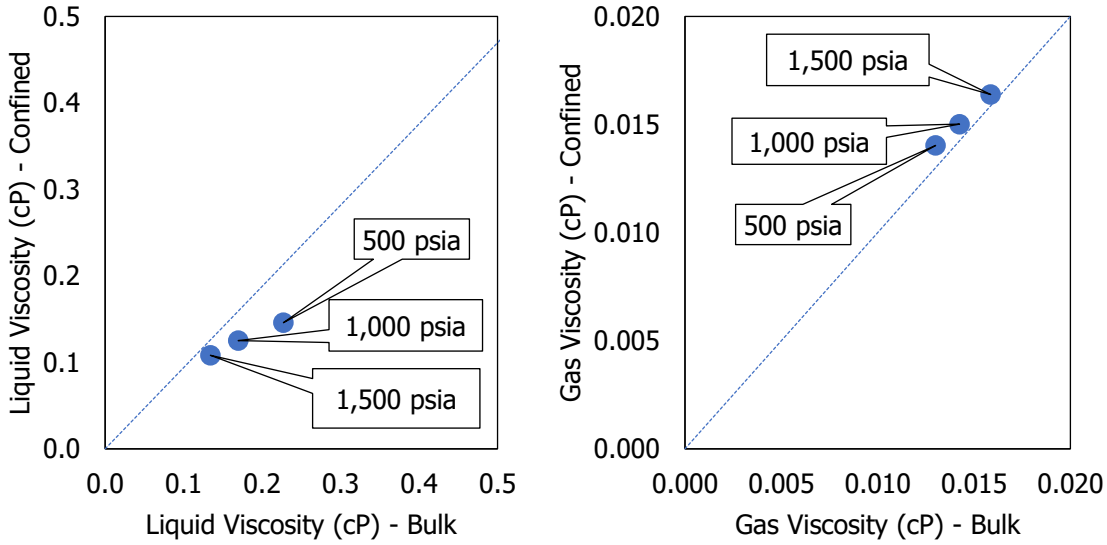

Fig. 2. 5—Liquid and gas viscosity of simplified fluid in Table 6. 4 for bulk and confined condition at 250°F. Confined case has 10 nm of pore diameter and 30° contact angle.

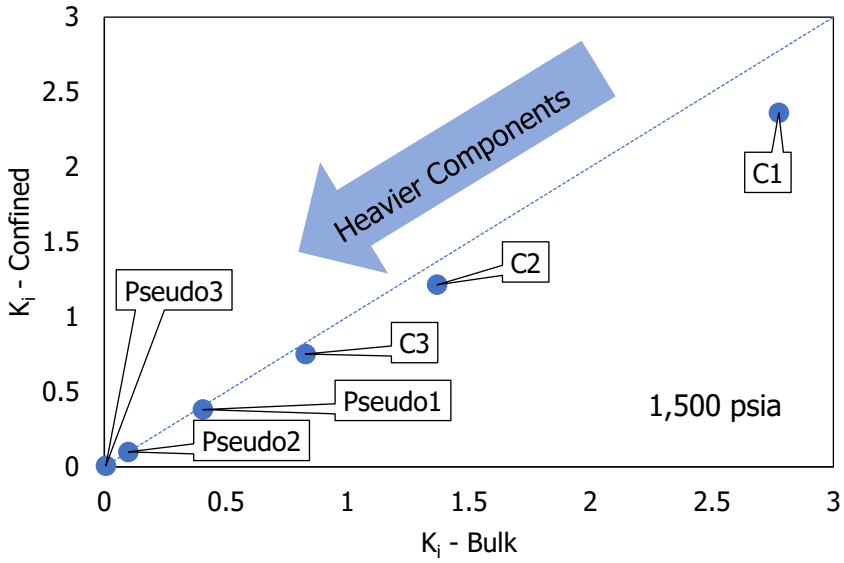

Fig. 2. 6—K-values of each component for fluid from Table 6. 4 at 1,500 psia and 250°F in bulk and confined state. Confined case has 10 nm of pore diameter and 30° contact angle.

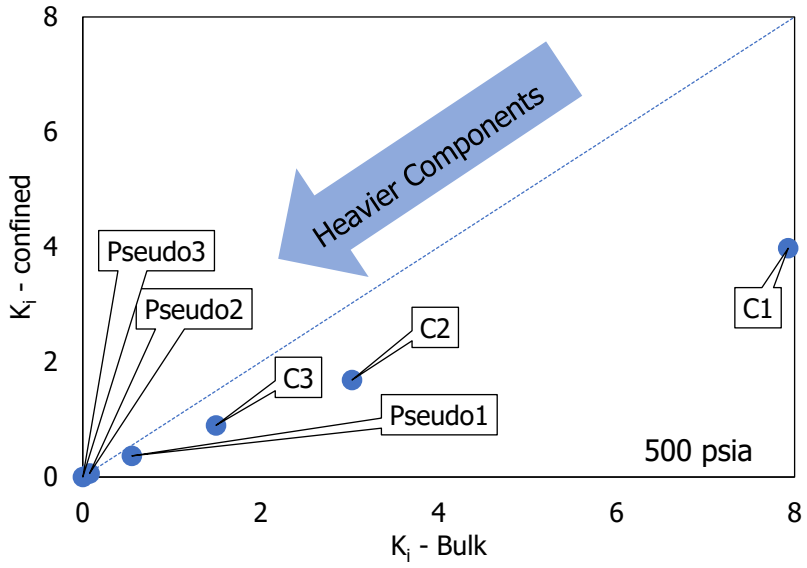

Fig. 2. 7—K-values of each component for fluid from Table 6. 4 at 500 psia and 250°F in bulk and confined state. Confined case has 10 nm of pore diameter and 30° contact angle.

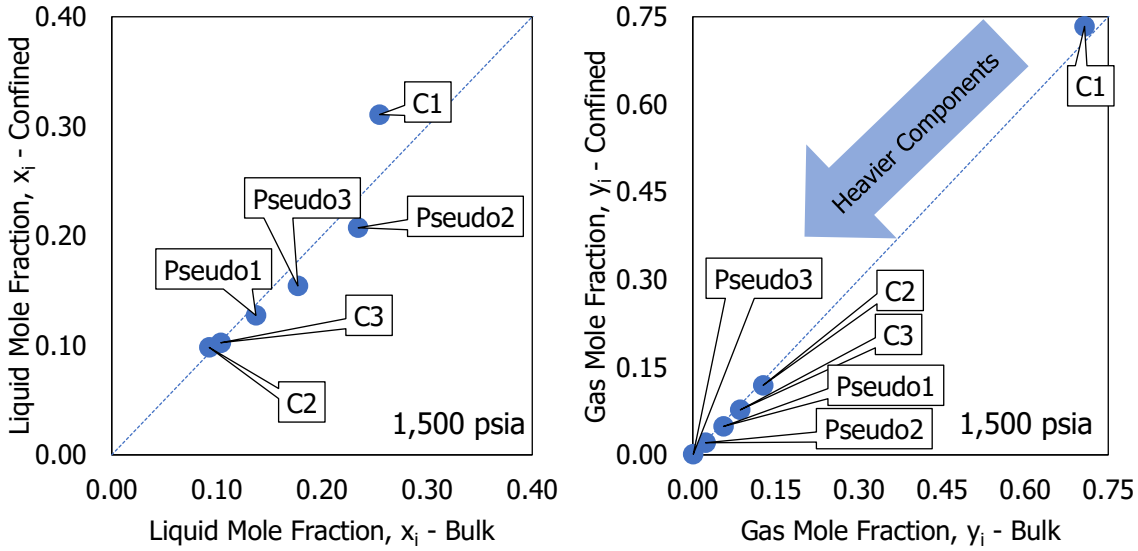

Fig. 2. 8—Liquid mole fraction, x_i, (left) and gas mole fraction, y_i, (right) of each component in Eagle Ford fluid from Table 6. 4 at 1,500 psia and 250°F in bulk and confined state. Confined case has 10 nm of pore diameter and 30° contact angle.

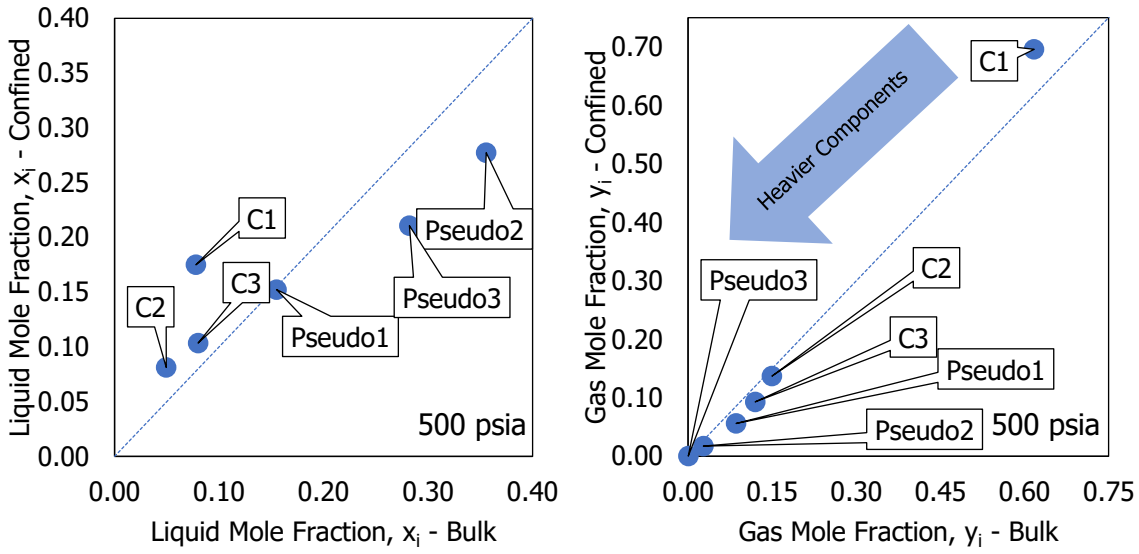

Fig. 2. 9—Liquid mole fraction, x_i, (left) and gas mole fraction, y_i, (right) of each component in Eagle Ford fluid from Table 6. 4 at 500 psia and 250°F in bulk and confined state. Confined case has 10 nm of pore diameter and 30° contact angle.

2.4 Minimum Miscibility Pressure Estimation Methods

One of the most successful EOR methods in conventional reservoirs is miscible gas injection. Miscibility is defined when the overall composition of the mixture has formed a single phase (Metcalfe et al. 1972). Injecting gas at or above the minimum miscibility pressure (MMP) has shown higher oil recovery than injecting below the MMP in conventional reservoirs. However, injecting at very high pressure may not be the most economical and not operationally feasible for specific fluid components and reservoir conditions (Tovar et al. 2018a, 2018b). Thus, predicting MMP is important for optimization.

Several methods have existed to estimate the MMP using laboratory experiments, analytical or numerical computations, or correlations. Correlation is the most practical to

MMP prediction but it is valid for very specific case (Enick et al. 1988). Analytical computation captures the dynamic miscibility or multiple-contact miscibility where the combined condensing and vaporizing gas displacement exists (R.T. Johns et al. 1993; Orr et al. 1993). Tovar et al. (2018b) showed the existence of both displacements from the CT scan analysis of the core sample after the core huff-n-puff experiment. Since we aim to honor thermodynamics, we focused on the understanding of the basis of the laboratory measurement methods and on the computational methods.

Although various MMP prediction methods have been well-studied, they are only proven for fluids in conventional reservoirs. Since the bubble point pressure has shown to be lower under confinement (Stimpson & Barrufet 2016), we also expect the MMP to be lower under confinement than those in bulk condition. To capture the deviation, this study involves adding the MMP calculation feature into the PVT simulator applicable for fluids in bulk and confined spaces. The new MMP calculation must be integrated with the modified equation of state (EOS) model to consider the nanopore confinement effect.

2.4.1 Laboratory Experimental Methods

The most common laboratory experiment to measure MMP is slim-tube experiment (Metcalfe et al. 1972). The setup usually requires a long tube with small diameter that is packed with glass beads and is saturated with oil at reservoir temperature. Next, the solvent gas is injected into the coiled tube, filled with packed sands, at a pressure. Several experiments need to be conducted at different pressure while the recovery is recorded to obtain the correlation between the recovery and pressure. Miscibility occurs

when the recovery factor increases dramatically or above 90% after injecting 1.2 PV of solvent gas. However, slim-tube experiment uses glass beads and packing that are usually limited to high porosity and high permeability. Other laboratory measurements worth mentioning are rising-bubble-apparatus (RBA) (Christiansen & Haines 1987; Jessen & Orr 2008) and vanishing-interfacial-tension (VIT) (Rao 1997) experiments. RBA utilizes a flat glass tube to view the gas bubble of the injected gas disappears into the oil, indicating multiple-contact miscibility condition. The disappearance of the gas bubble also means that the interfacial tension between the gas and oil also vanishes. VIT experiment involves measuring the interfacial tension as a function of pressure and extrapolating them to zero to find the MMP. Teklu et al. (2014) also attempted to simulate VIT method using the capillary pressure theory and indicated the lowering MMP in confinement. Although RBA and VIT methods are relatively faster than slim-tube experiments, they have their disadvantages. RBA and VIT does not use porous column to measure the MMP. Thus, the validity of VIT and RBA are questionable for unconventional reservoirs. Also, the data obtained from RBA is qualitive and subject to different interpretation by the observer and VIT method can overestimate the MMP at zero interfacial tension (Jessen & Orr 2008).

2.4.2 Computational Methods

Estimating MMP computationally is faster than measuring MMP through laboratory experiments. However, some calibration including the behavior of oil-solvent mixtures is necessary prior proceeding to the estimation of MMP. These may include volumetric measurements of miscible mixtures, swelling test, and saturation pressures.

Some of the most common MMP calculation methods are: slim-tube simulation, Method of Characteristics (MOC), and mixing cells. The slim-tube experiment previously described can be simulated by discretizing the tube into several time steps and cells loaded with oil. For one pressure stage, the total amount of injected gas is usually set to 1.2 pore volume (PV), converted to a number of moles at the specified pressure and temperature. The total moles of injected gas divided by the number of time steps is added into the first cell in each time step. Assuming the oil and gas reach equilibrium mixing instantaneously, the VLE calculation is applied in the first cell to obtain the equilibrium phase compositions and the phase volumes. The mechanism involves moving the excess oil or gas volume from the first cell to the next cell and repeating the VLE calculation for all the cells. Depending on the transport mechanism mode, the transfer of the excess volume can depend on the oil swelling, phase mobilities, or phase viscosities, as illustrated in **Fig. 2. 10**. However, phase mobility transport requires additional data of relative permeability and phase viscosities. The recovered oil for one pressure stage is the excess oil in the last cell accumulated from all time steps. The recovery factor per stage is the cumulative recovered oil volume in standard condition per stage divided by the original oil volume in standard condition. This process is repeated for several pressure stages. MMP occurs at the minimum pressure when oil recovery factor reaches a plateau. The MMP point can be observed on recovery versus pressure plot where the change in slope is significant. One of the uncertainties in this method is that the transport mechanism is only valid for high permeability porous media. Another disadvantage is the effect of numerical dispersion

that depends on number of cells and time steps. Very low permeability requires smaller time step size where numerical dispersion effect is higher.

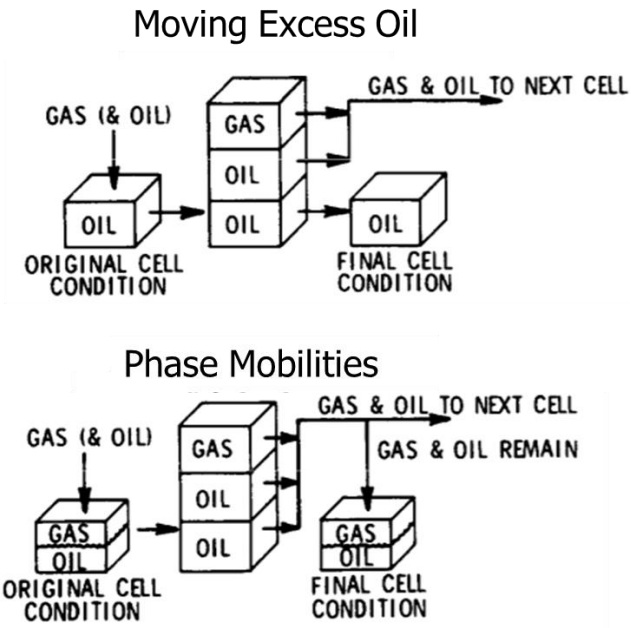

Fig. 2. 10—Transport mechanisms in slim-tube experiment simulation. Adapted from *A Multicell Equilibrium Separation Model for the Study of Multiple Contact Miscibility in Rich-Gas Drives* by Metcalfe et al. (1972).

MMP can also be computed analytically using Method of Characteristics (MOC). MOC is a mathematical approach to solve a hyperbolic partial differential equation in Eq. (2. 1) (Jessen et al. 1998; R.T. Johns et al. 1993; Orr et al. 1993; Wang & Orr 1997). It is a 1-D dispersion-free conservation equation in dimensionless form. A sequence of negative flash calculation, proposed by Whitson and Michelsen (1989), is required to obtain the phase composition for the overall fractional flux of component *i* (F_i) and the

overall volume fraction of the component *i* (C_i) and to construct the phase equilibrium tie-lines. This equation uses the fractional flow theory that depends on the phase saturation.

$$\frac{\partial C_i}{\partial t} + \frac{\partial F_i}{\partial x} = 0 \qquad i = 1,2,3 \ldots, N_c \tag{2. 1}$$

The MOC finds the velocity profile of the given composition and the shocks in the solution paths that connect between two tie-lines. The extension of these connected tie-lines must intersect to be considered as crossover tie-lines. The solution path is where the original oil and solvent gas composition connects. The steps in finding the key tie lines and crossover tie-lines at a pressure are repeated as the trial pressure is increased until it reaches the MMP, as shown in **Fig. 2. 11**. The MMP is the minimum pressure at which one of the key crossover tie lines becomes the critical tie line and has zero length. Although this method is rigorous and more robust than slim-tube simulation, the fractional flow equation and saturation (volume fraction) dependency can be too complex and increase computational power for low permeability rock when we include the capillary pressure.

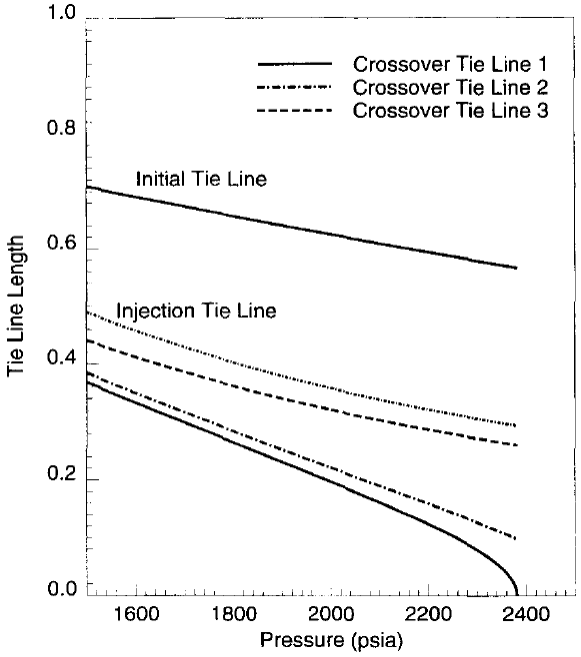

Fig. 2. 11—An example of key tie line lengths for CO_2 displacement of oil at 160°F. The MMP is 2,380 psia where the tie line length is zero on Crossover Tie Line 1 (Wang & Orr 1997).

Another method that is semi-analytical is mixing cell method. The method involves a single or multiple PVT cells where equal amount of solvent gas and original oil in mole fraction are mixed and obtaining the equilibrium phase compositions through VLE calculation at a specified pressure, starting below the MMP, and temperature. Then, the tie-line length in each contact, or mixing cell, is calculated based on the phase composition at a trial pressure. The MMP is the lowest pressure to approach zero tie-line length within a tolerance (Jensen & Michelsen 1990). In a single mixing-cell, there can only be either forward or backward contact miscibility. The forward contact mixing-cell is made from adding gas into the PVT cell filled with original oil and obtain the equilibrium gas composition. This new gas composition is added into the original oil again for the next

contact. This step is repeated until the composition does not change with more contacts. The process is the same for backward contacts but the equilibrium oil composition is being added into the cell filled with original gas composition. Flash calculations and tie-line length calculations for all contacts are repeated at a trial pressure. The tie-line length approaches zero as the trial pressure is increased, approaching the MMP. Since this method only consider the forward contacts or the backward contacts, it is likely to be overestimate MMP.

The multiple-mixing-cells method include both forward and backward contacts, or combined vaporizing/condensing gas drive mechanism. Ahmadi and Johns (2011) developed the Multiple-Mixing-Cell simulation method to estimate MMP for conventional reservoir fluid. The Multiple-Mixing-Cell method is considered more accurate than other numerical MMP estimation methods, such as slim-tube simulation. This method is similar to slim-tube simulation under moving-excess mechanism although it does not depend on recovery and cell volume, which it minimizes numerical dispersion effects. In addition, the mixing-cell method to estimate MMP is less computationally expensive than the analytical method of characteristics (MOC) because mixing cell method does not depend on fractional flow theory (Ahmadi & Johns 2011). Multiple-Mixing Cell essentially consists of mixing equal parts of the reservoir and injection fluid in mole fraction and calculating the equilibrium phase compositions in each of the mixing cell. The new gas composition is contacted with the original oil as forward contact while the new oil composition is contacted with the solvent gas as backward contact, capturing both the vaporizing/condensing gas drive mechanism. This method is practical for the

integration of the nanopore confinement model with the MMP calculation algorithm. Thus, we focus on applying Multiple-Mixing Cells method by Ahmadi and Johns (2011) method to calculate MMP for fluids under confinement and bulk condition for this study.

2.5 Molecular Diffusion as Predominant Recovery Mechanism

The term diffusion has extensive usage in transport phenomena. Some of the causes that result in diffusion are pressure gradients, thermal gradients, and concentration gradients (Reid et al. 1977). We focus on the diffusion caused by concentration gradients. The conventional advective transport, like Darcy's Law, cannot be applied in very low permeability reservoirs. Several studies have visualized molecular self-diffusion as the main transport mechanism within the matrix in ultra-tight rocks (Fernø et al. 2015; Hawthorne et al. 2013). Within the huff-n-puff process, the soaking period mainly relies on the molecular diffusion process.

The rate of diffusion depends on the diffusion coefficient. In predicting the recovery performance, we need to determine the diffusivity coefficient that can be a function of the pressure, temperature, and phase composition. There are several common practices to determine the diffusion coefficient through laboratory measurements and through empirical correlations.

2.5.1 Diffusivity Model

Theoretically, the binary-liquid diffusivity can be described by the Stokes-Einstein equation in Eq. (2. 2) although it has limited application (Reid et al. 1977).

Multicomponent gas-to-liquid mixtures theory, in which the diffusivity is also composition dependent, has been used to model diffusion in fractured reservoir (Hoteit & Firoozabadi 2009). The multicomponent diffusion is described by the Stefan-Maxwell equation. When there are no pressure gradients, the driving force is the chemical potential difference. Instead of the compositional gradients, a newer model uses the chemical potential gradient in Fickian diffusion model is claimed to be more appropriate for the phase boundary from fracture to the matrix (Moortgat & Firoozabadi 2013).

$$D_{ij} = \frac{RT}{6\pi\eta_j r_i} \tag{2. 2}$$

There are numerous empirical correlations for diffusion coefficient for limited cases. Some of the most popular ones are the Wilke and Chang (1955) correlation and Scheibel (1954) correlation for binary liquid diffusivities, which are essentially a modification of Stokes-Einstein formula, and Fuller et al. (1966) correlation for binary gas diffusivities at low pressure (Reid et al. 1977). Perkins and Geankoplis (1969) also suggested a correlation for diffusion in multicomponent liquid mixtures. Renner (1988) conducted experiments to measure diffusion coefficients of CO_2 in porous media at up to 850 psia and correlated the data with respect to the liquid properties. Likewise, Wang et al. (1996) correlated CO_2 gas diffusivity in liquid alkanes up to 750 psia based on Chapman-Enskog theory. However, Chapman-Enskog theory is usually applied in binary gas diffusion (Reid et al. 1977). Also, the diffusion coefficient of fluids in shale reservoirs at reservoir condition have been estimated using empirical correlations (Du & Nojabaei 2019). Sigmund correlation (Sigmund 1976) was found to match the most with the

experimental results. The fluid properties, such as density, was calculated using modified EOS with critical shift theory and capillary pressure theory to include nanopore confinement effect. Most of the diffusion coefficients presented in the literature, however, are only pure components binary diffusion coefficients, such as CO_2 with n-decane mixture (Grogan et al. 1988; Reid et al. 1977; Renner 1988; Sigmund 1976). Physics-based studies of the diffusion coefficient under reservoir condition in low permeability reservoirs are also not commonly available (Jia et al. 2019).

2.5.2 Diffusion Coefficient Measurement Methods

The diffusion coefficient can mostly be obtained through laboratory experiments, such as the pressure-decay method, CT-scan method, and PVT cell method. Unfortunately, these methods would not be feasible for tight oil reservoirs because they are usually conducted under low pressure on high permeability rocks and require a long time to obtain sufficient data if done on ultra-low permeability rocks (Jia et al. 2019).

a. Pressure Decay Method

The principle of pressure decay method is displacing the solvent gas into a PVT cell filled with the liquid or oil at a constant volume and temperature as the pressure depletes over time. The amount of solvent gas in liquid phase, or solvent gas lost from the gas phase, is calculated using an EOS from the recorded pressure drops over time and the known remaining volume of the solvent in gas phase to determine the diffusion coefficient value (Araújo 2014; Li & Dong 2009; Renner 1988; Riazi & Dauber 1987). There are variations of experimental set up for the pressure decay technique for gas in liquid

diffusion, such as using capillary tube (Grogan et al. 1988), using core in the diffusion cell (Li & Dong 2009; Renner 1988), or only the diffusion cell. Li and Dong (2009) presented a method to measure the CO_2 effective diffusion coefficient in oil-saturated Barea cores inside the PVT cell under reservoir conditions. They focused on the effect of the swelling-induced convection caused by CO_2-oil fluid interaction, where the oil swelling is measured before the pressure decay experiment. They matched the mathematical model with the pressure decay experimental data to find the binary diffusion coefficient. Then, the diffusion coefficient from the analytical approach can be matched with the experimental data. It is noted that they assume oil and gas are not fully miscible. The diffusion coefficient is assumed constant throughout the pressure decay method to simplify the calculation. Their mathematical model and numerical approach inspired our understanding in the diffusion process in unconventional liquid reservoirs.

b. CT scan Method

The CT scan method utilizes the density difference to trace the components of the oil and the solvent in the porous media. This method requires calibration in CT scan reading depending on the energy level of the materials within the rock. Thus, the CT scan method's accuracy is bound to the imaging capability and quality. The solvent concentration can be obtained from the density of the mixture through CT scan data and density correlation (Araújo 2014).

Tovar et al. (2018a) conducted core flooding experiments to imitate huff-n-puff gas injection on a hydraulically fractured rock. He concluded that the driving mechanism is a peripheral slow-kinetics vaporizing gas drive where the gas vaporizes the oil instead

of displacing the oil. This driving mechanism hinders the fluids from being fully miscible. They also analyzed the CT scan images of the core after the flooding experiment. The changes in the density of the CT scan images show the hydrocarbon vaporization or CO_2 condensation. These images can predict how much the gas penetrates the core and can validate the diffusion coefficient estimation.

CHAPTER III

MINIMUM MISCIBILITY PRESSURE IN CONFINEMENT

3.1 Phase Behavior Modeling

In the phase behavior numerical model, we use the Peng-Robinson equation (Peng & Robinson 1976) of state (EOS) in Eq. (3. 1) with volume shift correction. The mixing rules and the parameters used are defined in Eq. (3. 2) to Eq. (3. 5a).

$$p^j = \frac{RT}{V_m^j - b^j} - \frac{a\alpha^j}{V_m^j\left(V_m^j + b^j\right) + b^j\left(V_m^j - b^j\right)} \tag{3. 1}$$

$$a\alpha^j = \sum_{i=1}^{Nc}\sum_{k=1}^{Nc} x_i^j x_k^j (a_i a_k \alpha_i \alpha_k)^{1/2}(1 - \delta_{ik}) \tag{3. 2}$$

$$a_i = 0.45724\frac{R^2 {T_{c,i}}^2}{p_{c,i}} \tag{3.2a}$$

$$\alpha_i = \left[1 + \kappa_i\left(1 - \sqrt{T_{r,i}}\right)\right]^2 \tag{3.2b}$$

$$\kappa_i = 0.37464 + 1.54226\omega_i - 0.26992{\omega_i}^2,\ \omega_i \le 0.491 \tag{3.2c}$$

$$\kappa_i = 0.37964 + 1.4875\omega_i - 0.16442{\omega_i}^2 + 0.0167{\omega_i}^3,\ \omega_i > 0.491 \tag{3.2d}$$

$$T_{r,i} = \frac{T + 459.67}{T_{c,i} + 459.67} \tag{3.2e}$$

$$b^j = \sum_{i=1}^{Nc} x_i^j b_i \tag{3. 3}$$

$$b_i = 0.07780 \frac{RT_{c,i}}{p_{c,i}} \tag{3.3a}$$

Péneloux et al. (1982) modified the Peng-Robinson EOS by adding the volume translation parameter defined in Eq. (3. 4). The volume shift parameter, s_i, is defined from a correlation by Miqueu et al. (2003). Then, the density can be calculated with the modified molar volume in Eq. (3. 5). The volume translation is calculated after the vapor-liquid phase equilibrium calculation.

$$\tilde{V}_m^j = V_m^j - \sum_{i=1}^{Nc} s_i b_i x_i^j \tag{3. 4}$$

$$s_i = \left|T_{r,i} - 0.628\right|^{2.28} - 0.155 + 0.421\omega_i + 0.590\exp\left[28.40\left(T_{r,i} - 1\right)\right] \tag{3.4a}$$

$$\tilde{\rho}^j = \frac{M^j}{\tilde{V}_m^j} \tag{3. 5}$$

$$M^j = \sum_{i=1}^{Nc} x_i^j M_i \tag{3. 5a}$$

3.1.1 Vapor-Liquid Equilibrium (VLE) Calculation

The VLE or flash calculation is developed by Rachford and Rice (1952) by solving Eq. (3. 6) and determine the vapor phase fraction of the mixture, β. The equilibrium constant, or K-values, is defined in Eq. (3. 7). Eq. (3. 8) and Eq. (3. 9) are the equation for the liquid and vapor phase fraction of each component. Solving the Eq. (3. 6) requires iterative process. So, Wilson (1969) proposed an initial guess for the K-values, as shown in Eq. (3. 11).

$$\sum_{i=1}^{Nc} \frac{(K_i - 1)z_i}{(K_i - 1)\beta + 1} = 0 \tag{3. 6}$$

$$K_i = \frac{y_i}{x_i} \tag{3. 7}$$

$$x_i = \frac{z_i}{(K_i - 1)\beta + 1} \tag{3. 8}$$

$$y_i = x_i K_i \tag{3. 9}$$

$$K_i = \frac{p_{c,i}}{p} \exp\left[5.37(1 + \omega_i)\left(1 - \frac{1}{T_{r,i}}\right)\right] \tag{3. 10}$$

In the flash calculation, the goal is to equate the fugacity equation, which is defined in Eq. (3. 11) and Eq. (3. 12). Since the difference in pressure in gas phase and liquid phase are negligible in bulk condition, the fugacity equation in Eq. (3. 13) becomes Eq. (3. 14). The definition of K-values is described in Eq. (3. 15). Once the K-values are determined, we calculate the molar volumes and end the flash simulation.

$$f_i^l = f_i^v \tag{3. 11}$$

$$f_i^j = x_i \hat{\phi}_i^j p^j \tag{3. 12}$$

$$x_i \hat{\phi}_i^l p^l = y_i \hat{\phi}_i^v p^v \tag{3. 13}$$

$$x_i \hat{\phi}_i^l = y_i \hat{\phi}_i^v \tag{3. 14}$$

$$K_i = \frac{y_i}{x_i} = \frac{\hat{\phi}_i^l}{\hat{\phi}_i^v} \tag{3. 15}$$

However, the large capillary effect changes the fugacity calculation. We start by defining the Young-Laplace capillary pressure in Eq. (3. 16) and Eq. (3. 17). Additional input in the simulation are the interfacial tension (IFT), wettability contact angle, and the pore diameter to consider the capillary pressure. The wettability and pore diameter data comes from laboratory measurements. We use the IFT model in our PVT Simulator in Eq. (3. 18) (Danesh et. al. 1991). Then, we substitute the vapor phase pressure in Eq. (3. 16) into Eq. (3. 19). The K-values equation becomes Eq. (3. 20) with the fugacity defined in Eq. (3. 21). Since the IFT model depends on the molar volume that also depends on the K-values, the iteration and the overall VLE computation become more expensive.

One of the advantages of the capillary pressure model is the simplicity. Unlike molecular simulation, we only need to adjust fewer parameters and less computational power. It includes the fluid and rock interaction based on the wettability and pore size.

$$p^v = p_{cap} + p^l \tag{3. 16}$$

$$p_{cap} = \frac{2\sigma\cos(\theta)}{r} \tag{3. 17}$$

$$\sigma^{1/4} = \sum_{i=1}^{Nc} P_i \left(\frac{x_i}{\tilde{V}_m^l} - \frac{y_i}{\tilde{V}_m^v} \right) = \sum_{i=1}^{Nc} P_i \left(\frac{x_i \tilde{\rho}^l}{{M_w}^l} - \frac{y_i \tilde{\rho}^v}{{M_w}^v} \right) \tag{3. 18}$$

$$x_i \hat{\phi}_i^l p^l = y_i \hat{\phi}_i^v \left(p^l + p_{cap} \right) \tag{3. 19}$$

$$K_i = \frac{y_i}{x_i} = \frac{\hat{\phi}_i^l p^l}{\hat{\phi}_i^v \left(p^l + p_{cap} \right)} = \frac{\hat{\phi}_i^l p^l}{\hat{\phi}_i^v \left(p^l + \frac{2\sigma\cos(\theta)}{r} \right)} \tag{3. 20}$$

$$\ln \hat{\phi}_i^l = \int_0^{p^j} \left(Z^j - \frac{1}{p} \right) dp \tag{3. 21}$$

$$\hat{\phi}_i^l = \exp\left[\frac{b_i}{b^j} (Z^j - 1) - \ln(Z^j - B^j) - \frac{A^j}{2\sqrt{2} B^j} \left(\frac{\psi_i^j}{a\alpha^j} - \frac{b_i}{b^j} \right) \ln\left(\frac{Z^j + \left(1 + \sqrt{2}\right) B^j}{Z^j + \left(1 - \sqrt{2}\right) B^j} \right) \right] \tag{3.21a}$$

$$\psi_i^j = 2 \sum_{k=1}^{Nc} x_k^j (a_i a_k \alpha_i \alpha_k)^{1/2} (1 - \delta_{ik}) \tag{3.21b}$$

3.2 Effect of Capillary Pressure on Phase Behavior in Gas Injection

With our existing PVT simulator, the fluid phase behavior deviation under confinement from the bulk condition can be observed. Although the capillary pressure effect, by definition, requires two phases to exist, the capillary effect still changes the

phase envelope at its equilibrium state. In **Table 3. 1**, the density and viscosity for different pore diameters are obtained at its saturation pressure under confinement. The reservoir fluid used in **Table 3. 1** is an Eagle Ford Shale oil characterized by Ramirez and Aguilera (2014), as listed in **Table 6. 3**. These values are compared to the properties under the bulk condition at the same pressure. It shows that the deviation is higher with lower pore diameter. The difference in density would likely change the swollen volume under confinement and affect the diffusion coefficient. The density and viscosity are lower under confinement, which are favorable conditions for mobility in gas injection processes.

Stimpson and Barrufet (2016) had noted that there is suppression in the phase envelope with the confinement effect. As an early investigation, we apply an injected gas into a Bakken Shale reservoir fluid from published data (Yu et al. 2015) and predict the bubble point pressure. The test involves a pure carbon dioxide (CO_2) gas injection and a mixture of 85% of CO_2 and 15% of nitrogen (N_2) gas injection. As the amount of injection gas increases, the bubble point pressure becomes higher, as seen in **Fig. 3. 1**. The bubble point pressure in confinement is lower than in bulk. Adding nitrogen gas increases the bubble point pressure. The bubble point pressure is very close to the miscibility pressure. We obtained miscibility pressure at the varying amount of injection gas from a commercial simulator and generate saturation pressure with and without confinement effect from our PVT simulator. **Fig. 3. 1** shows that the miscibility pressure and the saturation pressure in bulk condition are very similar. Since the saturation pressure in confinement is lower than in bulk condition, we can expect that the minimum miscibility pressure to be lower under confinement. From the conclusion of **Fig. 3. 2**, we can expect

that the nitrogen gas mixture would increase the minimum miscibility pressure under confinement.

Table 3. 1—Comparison of density and viscosity under the bulk and confined conditions.

Pore Diameter (nm)	Pressure (psi)	Density (lbm/ft^3)			Viscosity (cP)		
		Bulk	Confined	Deviation (%)	Bulk	Confined	Deviation (%)
15	2,181	37.503	36.916	1.57%	0.09300	0.08840	5.11%
10	2,146	37.718	36.814	2.40%	0.09500	0.08780	7.81%

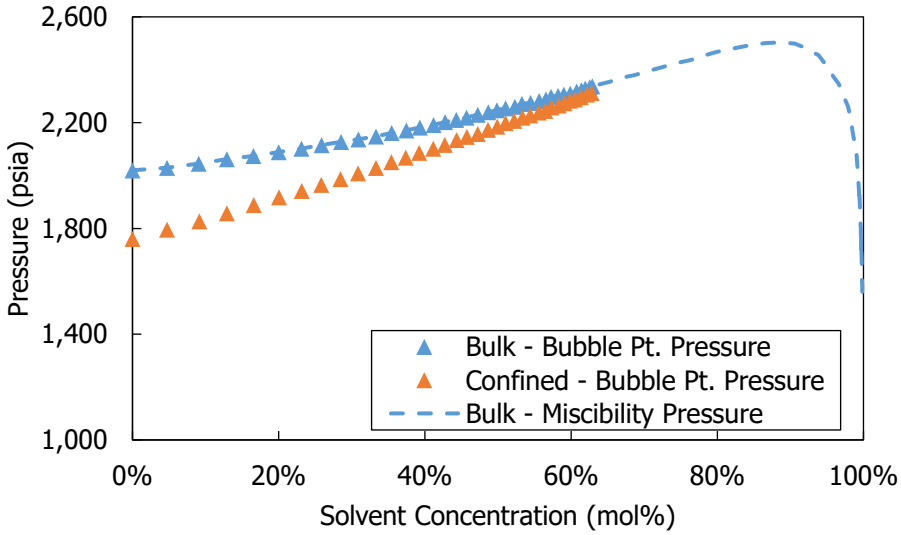

Fig. 3. 1—Miscibility pressure obtained from a commercial simulator and saturation pressure obtained from our PVT simulator at 200 °F using pure CO_2 solvent. The pore diameter is 15 nm and contact angle is 30° for confined state.

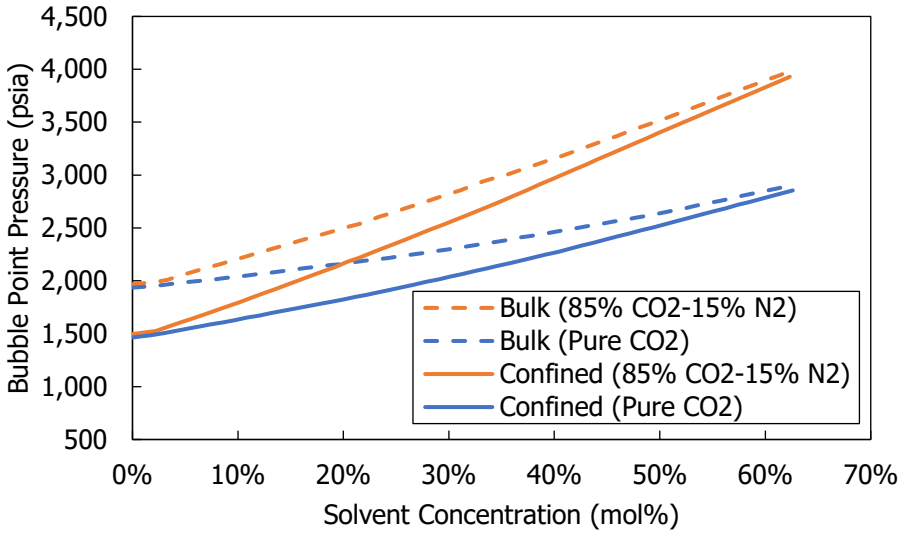

Fig. 3. 2—Saturation pressure at 200 °F for pure CO_2 injection and 85% CO_2-15% N_2 mixture injection under bulk condition (dashed lines) and confinement (solid lines).

3.3 Condensing-Vaporizing Gas Drive

Miscibility occurs when the overall composition forms a single phase (Metcalfe et al. 1972). Multiple-contact miscibility is attainable at a lower pressure than first-contact miscibility. First-contact miscibility requires for the gas and oil to be miscible at the first mixture or contact; thus, it requires higher pressure. The ternary diagram below allows to visualize the multiple-contact miscibility. The ternary diagram shows three pseudo-components of injection gas, intermediate hydrocarbons, and heavy hydrocarbons at a fixed pressure and temperature. The numbers on the sides are the mole fractions of each pseudo-component for the mixtures in dots. Inside the solid purple line is the two-phase region while the dashed purple lines are the equilibrium tie lines with the ends indicating the vapor and the liquid phase composition of the mixture along the tie line. The blue dot

indicates the critical point where the tie line distance is zero. The first contact happens when mixing the injection gas composition in the top most red dot with the original oil composition in liquid phase in bottom most green dot and forms an equilibrium mixture in yellow dot. This equilibrium mixture produces new compositions of vapor phase and liquid phase.

In vaporizing gas drive process, the new vapor phase mixes with the original oil composition in the next contact that forms a new equilibrium mixture with lighter vapor phase and heavier liquid phase. **Fig. 3. 3** only depicts the forward-contacts or vaporizing gas drive. It occurs when the injected gas vaporizes the light to intermediate hydrocarbons and enriches the vapor phase with heavier components in the equilibrium mixture. On the other hand, condensing gas drive process, or backward-contacts, happens when the injected gas is condensed into the liquid phase and enriches the liquid phase with lighter components. These multiple-contacts happen until the vapor phase reaches its maximum enrichment. In **Fig. 3. 3**, the maximum enrichment meets the critical point; thus, it reaches multiple-contact miscibility (Metcalfe et al. 1972). It is possible because the oil composition lies on the left side of the critical point. Otherwise, the injection gas is partially miscible with the oil. We can increase the pressure to shrink the two-phase region with lighter critical point to obtain full-miscibility condition, as shown in **Fig. 3. 4**. The same philosophy applies to the condensing gas drive process.

In a favorable multiple-contact miscibility condition, both condensing and vaporizing gas drive processes happen simultaneously where the injection gas vaporizes the oil at the forward end and condenses into the liquid phase at the backward end. Only

considering one of the driving processes when evaluating the MMP can lead to overestimation of the multiple-contact miscibility pressure (Jensen & Michelsen 1990; R.T. Johns et al. 1993).

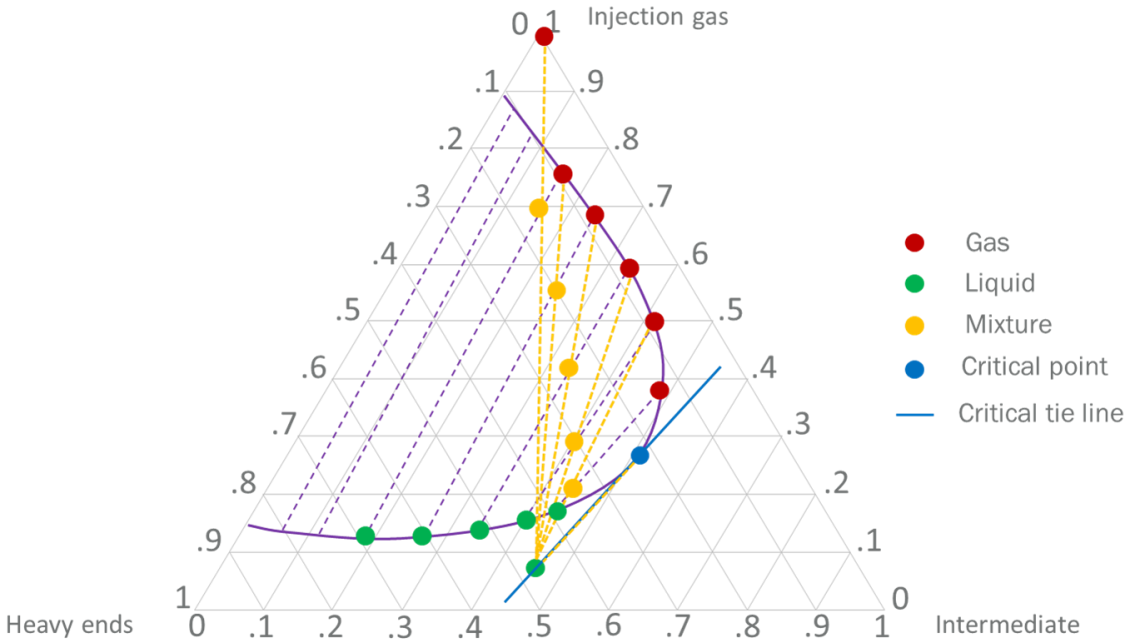

Fig. 3. 3—Ternary diagram of multiple-contact miscibility in vaporizing gas drive, or forward multiple-contact process.

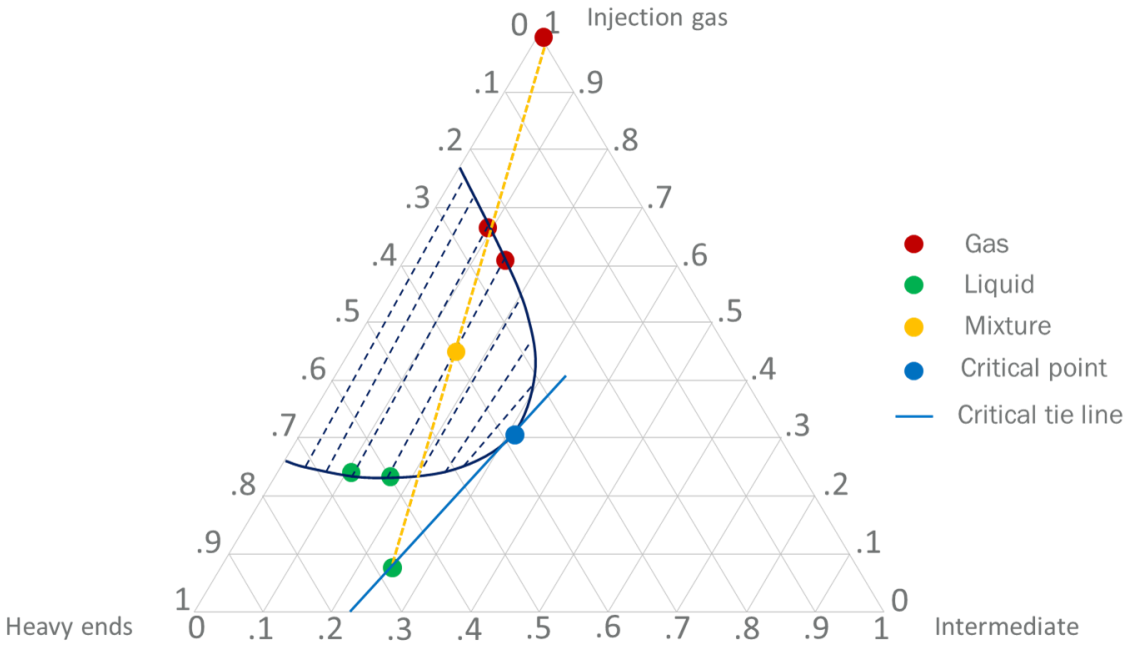

Fig. 3. 4—Ternary diagram of the first contact in vaporizing gas drive process at a higher pressure than in Fig. 3. 3 with smaller two-phase region and heavier oil composition.

3.4 Computational Algorithm

In this research, we are using the Multiple-Mixing-Cells (MMC) method to calculate the MMP. Ahmadi and Johns (2011) developed an MMC model that only relies on the Vapor-Liquid Equilibrium (VLE) calculations without the effect of cell volume. Since the coupled EOS is incorporated into the VLE procedure, the MMC model is compatible to estimate MMP for fluids under confinement.

The MMC method captures vaporizing, condensing gas drive, and a combination of both. **Fig. 3. 5** illustrates the mixing cells between the oil and the solvent gas. We assume the original oil in place is a single liquid phase. The leftmost mixtures are the

condensing gas drive process whereas the rightmost mixtures are the vaporizing gas drive process. The mixing cells in the middle area are combination of condensing and vaporizing gas drive process. Unlike single-mixing-cells method, MMC is advantageous because it considers multiple-contact miscibility and avoids bias from specifying the main driving mechanism. This chapter provides a flow chart of the MMP estimation algorithm in **Fig. 3. 6**.

The first part of the algorithm is reading the input data, such as the oil and injection fluid composition and their EOS parameters. To model the nanopore confinement effect, we also need the pore throat radius in nanometer and the oil contact angle in degrees. The first contact or the first mixing cell is the oil and the solvent combination. Then, the VLE calculation is performed to produce the new vapor and liquid equilibrium composition that would be mixed with the oil and the solvent in the next mixing cells, or contacts, as illustrated in **Fig. 3. 1**. Chapter 3.1 explains the VLE algorithm in the PVT Simulator. This algorithm is slightly modified to produce the K-values and the liquid and vapor mole fractions as the output. The tie-line length calculation requires equilibrium liquid, x_i, and vapor mole fraction, y_i, in each mixing cell, as shown in Eq. (3. 22), where Nc is the number of components. We store the tie-line length in each contact at the specified pressure and determine the minimum value as the gas tie lines, oil tile lines, and crossover tie lines. The oil tie lines indicate vaporizing miscibility while the gas tie lines indicate condensing miscibility. If the minimum tie-line length reaches zero, the pressure is the MMP. Otherwise, we repeat the mixing cells process at higher pressure until we reach

zero minimum tie-line length. After the first three trial pressures, we use linear extrapolation to obtain the next trial pressure.

$$TL = \sqrt{\sum_{i=1}^{Nc} (x_i - y_i)^2} \tag{3. 22}$$

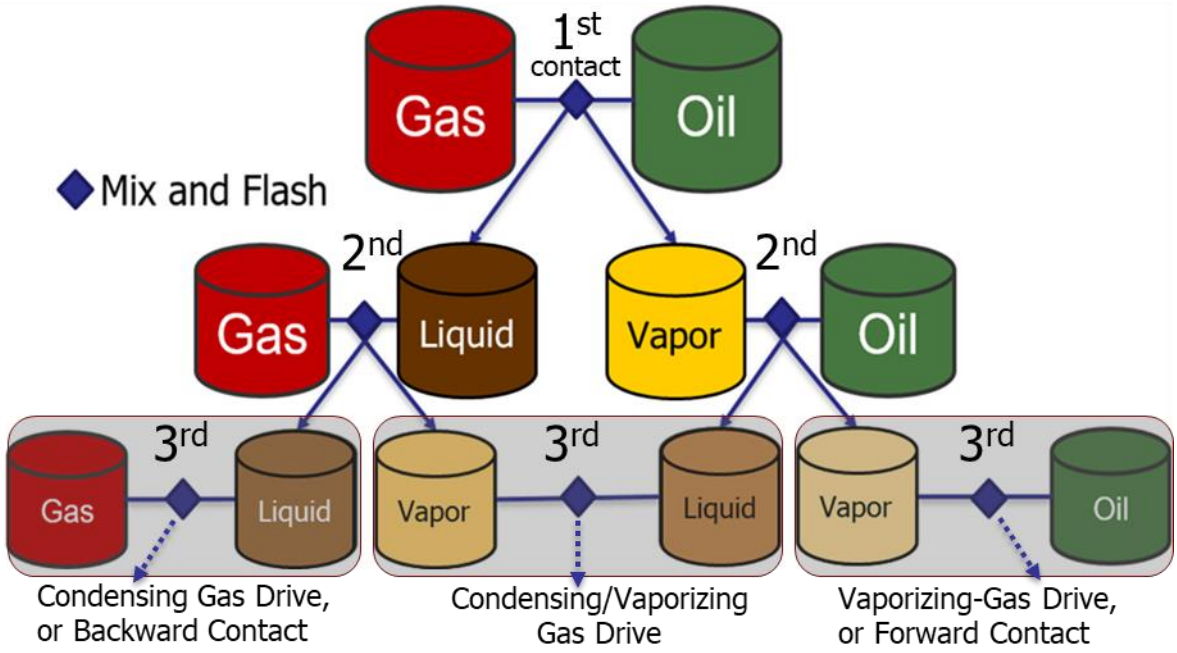

Fig. 3. 5—Illustration of Multiple-Mixing-Cells method after 3 contacts. Each color represents a different composition in the cell resulted from each contact.

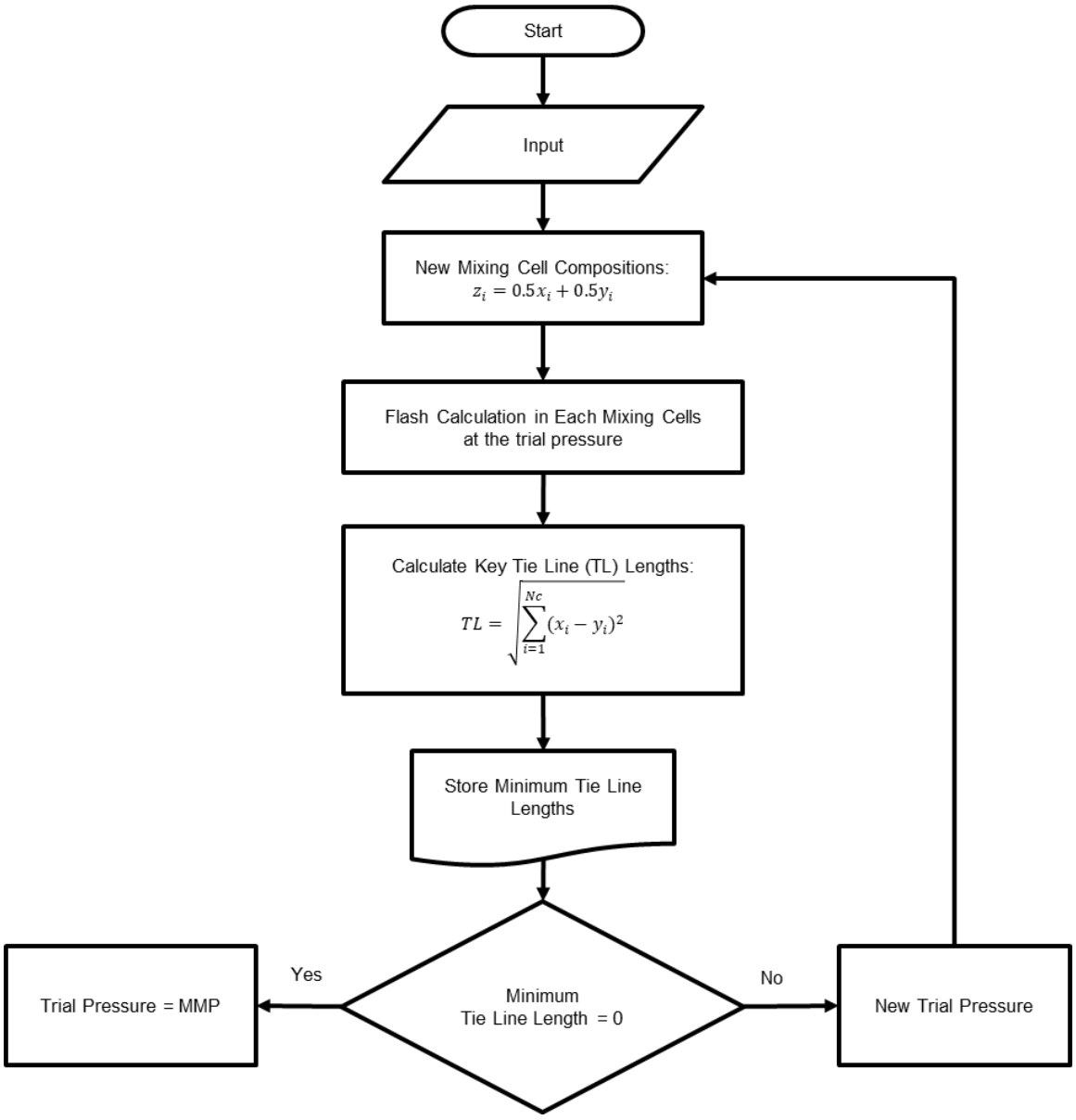

Fig. 3. 6—The flow chart for the MMP estimation algorithm using the Multiple-Mixing-Cells method.

3.5 Results and Discussion

The MMP results from the PVT Simulator are presented below. We use a synthetic oil (Wang & Orr 1997) and an Eagle Ford volatile oil characterized by (Ramirez & Aguilera 2014). The composition of these fluids is described in Chapter VI in **Table 6. 1** and **Table 6. 3**, respectively. We compare the MMP between using pure CO_2 and a mixture of 80 mol% CO_2 and 20 mol% CH_4 as the solvent gas. We used 30° contact angle and 200°F temperature consistently throughout this chapter. The tie line lengths in **Fig. 3. 7** and **Fig. 3. 8** show the oil tie line, gas tie line, and crossover tie line trends. The crossover tie line is where the minimum tie line length lies for the specific pressure and temperature. Fig. 3. 7 and Fig. 3. 8 implies that the minimum tie line lengths closest to zero correspond to the most confined condition, which is at 10 nm pore diameter. It predicts that the MMP is lower at lower pore diameter. The crossover tie line lengths in both figures do not reach zero yet because 1,700 psi is below the MMP. The process of increasing the pressure to obtain MMP is repeated until we reach zero tie-line length, as shown in **Fig. 3. 9**. The pressure stages were set for 15 data points. They are sufficient to extrapolate the MMP. But, as illustrated in 15 nm case in **Fig. 3. 9**, the minimum tie-line length trend converges faster to MMP as it goes closer to MMP value. Thus, using linear extrapolation for the MMP value tends to overestimate the MMP.

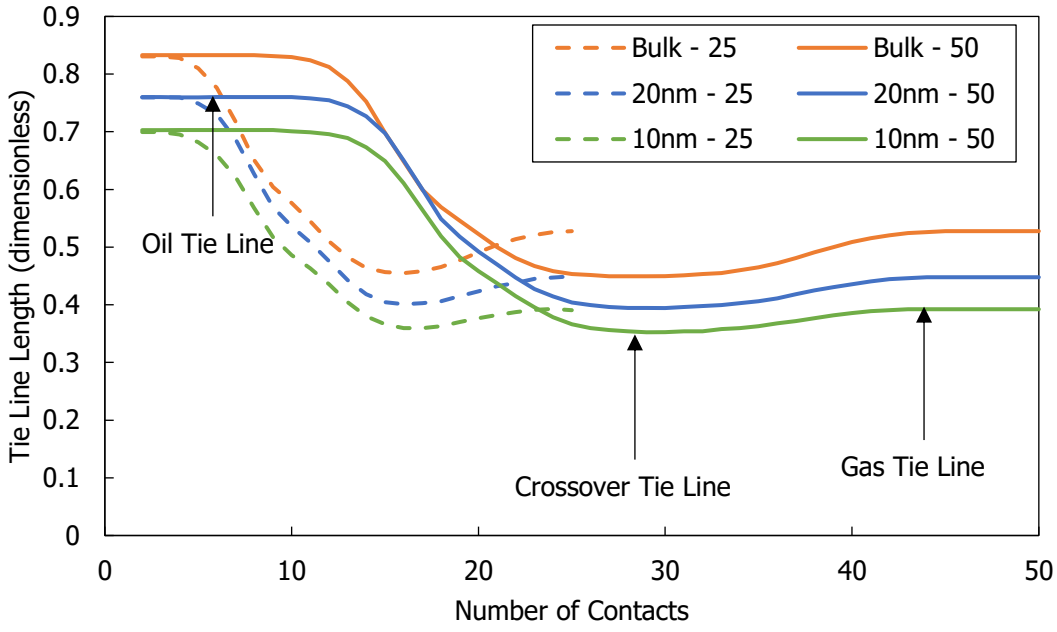

Fig. 3. 7—Tie-line lengths of each contact number or cell using the synthetic oil from Table 6. 1 and pure CO_2 solvent at 1,700 psi and 200°F for pore diameters of 10 nm, 20 nm, and bulk condition and using total number of contacts of 25 and 50.

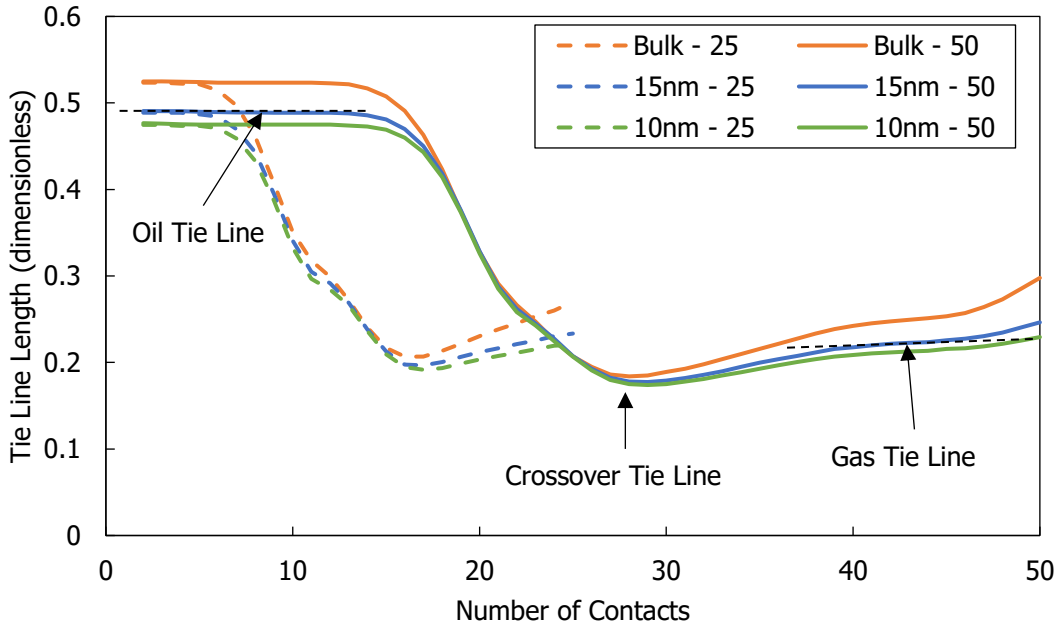

Fig. 3. 8—Tie-line lengths of each contact number or cell using the Eagle Ford oil from Table 6. 3 and pure CO_2 solvent at 1,700 psi and 200°F for pore diameters of 10 nm, 15 nm, and bulk condition and using total number of contacts of 25 and 50.

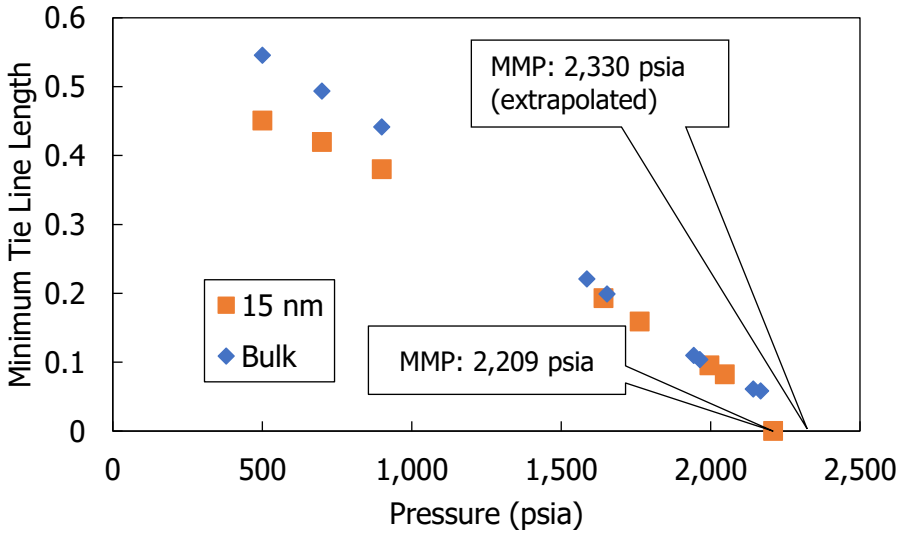

Fig. 3. 9—Minimum tie-line lengths of each trial pressure from 50 contacts for 15 nm and bulk case of Eagle Ford oil (Table 6. 3) displacement by pure CO_2 at 200°F.

We estimate the MMP for pure CO_2 injection on synthetic oil in **Table 3. 2** and on Eagle Ford oil in **Table 3. 3** at 200°F. We also test using the effect of total number of contacts on the accuracy of our MMP results. The results confirm that the MMP is lower at lower pore diameter when capillary pressure is considered. This is expected because the nanopore confinement suppresses the phase envelope, resulting in lowering bubble point pressure and lowering MMP. The deviation from bulk condition is more pronounced in the synthetic oil than in Eagle Ford oil. The synthetic oil has more mole percentage of heavy component than the Eagle Ford oil. The deviation is larger when using the CO_2/CH_4 mixture in **Table 3. 4** with the synthetic oil than using pure CO_2. Table 3. 4 result also does not follow the trend because the MMP in bulk condition in Table 3. 4 is larger than the MMP in bulk condition in **Table 3. 3**, but the MMP in confinement in Table 3. 4 are lower than those in **Table 3. 3**. Thus, we do not have enough data to correlate the degree of deviation to certain fluid components. Since it is highly dependent on the solvent and the oil composition, the PVT study is crucial in EOR design.

Table 3. 2—Comparison of MMP results of the pure CO_2 injection onto the synthetic oil using the specified number of contacts at a given pore diameter at 200°F.

	MMP (psia)	
Pore Diameter (nm)	25 Contacts	50 Contacts
Bulk	2,310	2,268
30	2,030	2,070
15	1,845	1,890

Table 3. 3—Comparison of MMP results of the pure CO_2 injection onto the Eagle Ford oil using the specified number of contacts at a given pore diameter at 200°F.

	MMP (psia)	
Pore Diameter (nm)	25 Contacts	50 Contacts
Bulk	2,430	2,330
30	2,200	2,260
15	2,170	2,210

Table 3. 4—Comparison of MMP results of the solvent mixture of 80 mol% CO_2 and 20 mol% CH_4 onto the synthetic oil using the specified number of contacts at a given pore diameter at 200°F.

	MMP (psia)		
Pore Diameter (nm)	25 Contacts	75 Contacts	100 Contacts
Bulk	2,910	2,810	2,790
30	1,970	1,940	1,930
15	1,840	1,820	1,790

CHAPTER IV

MOLECULAR DIFFUSION FLOW MECHANISM

The focus of the study is to simulate the diffusion process during solvent injection, particularly in modified huff-n-puff processes in liquid-rich shale reservoirs. A practical method is presented to estimate recovery in a gas-assisted recovery process and to determine effective diffusion coefficients from experimental data. When two fluids reach miscibility, the solvent and reservoir fluid become a single-phase and the mixing between the two fluids within the porous media has to be quantified. In the case of tight porous media, the main flow mechanism is molecular diffusion because of the very low permeability condition. This chapter starts with the theoretical background of molecular diffusion. It also explains the derivation of the equation used in the numerical simulation.

4.1 Theory

When we are dealing with very low permeability porous media, the main flow mechanism is the molecular diffusion. Molecular diffusion occurs at the interface between two components or fluid mixtures and its main parameter is the diffusion coefficient. The advective flow occurs when there is a flow velocity difference. A combination of molecular diffusion and advective or convective flow is called dispersion. The Peclet number, a dimensionless number for the ratio of the advective or convective transport rate to the diffusive transport rate, indicates the dominating flow regime (Araújo 2014; Lie 2013). The Peclet number is very small due to the very small pore size and low fluid velocity in

the matrix, which means the diffusive transport is the dominating mechanism in unconventional shale reservoirs.

In modeling a miscible flow between the solvent and oil in the matrix, we need to consider both the diffusion and the oil swelling effect. The oil swelling causes the velocity difference that adds the advective/convective term into the governing equation. The oil swelling effect cannot be neglected because the oil production is based on the excess volume from the oil volume expansion. We also test the relative contribution of the molecular diffusion flow and the advection flow.

For simulating the huff-n-puff process, we use a constant pressure and temperature system without the gravitational force effect. We limit the study only to diffusion of two pseudo-binary liquid-phase fluids. In other words, we assume a condensing gas drive process. This study includes the flow from the fracture to the matrix, but it does not include the flow to the fracture. We simplify the complex fracture geometry into a planar fracture in Cartesian system and the outer radius of the reservoir in radial system as illustrated in **Fig. 4.1** and **Fig. 4.2**. Although the planar fracture in Cartesian system is more common and realistic to simulate field scale, we included radial system to simulate laboratory experiments that usually use cylindrical core samples, such as the huff-n-puff core experiment by Tovar et al. (2018a).

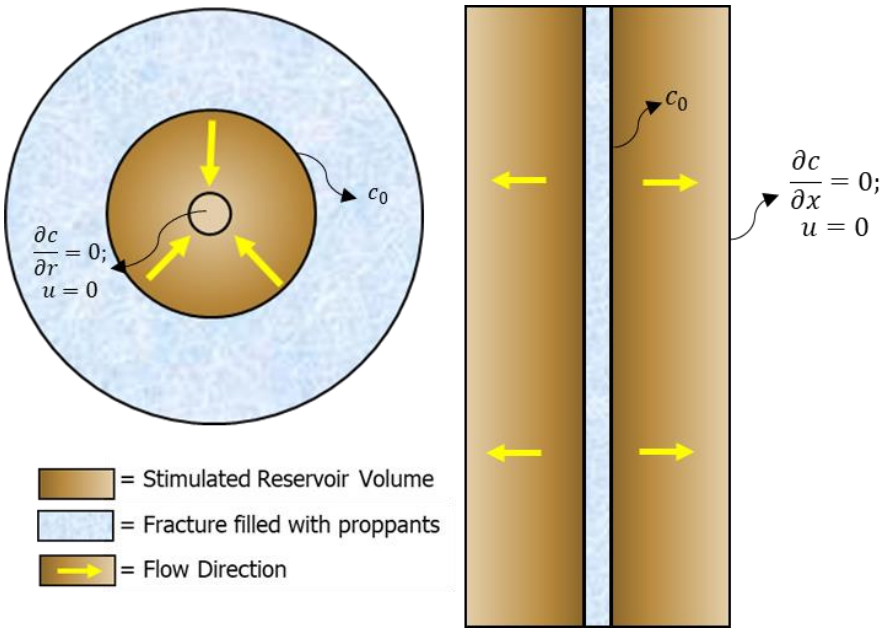

Fig. 4. 1—Radial flow and linear flow of the solvent into the SRV and the assigned boundary conditions.

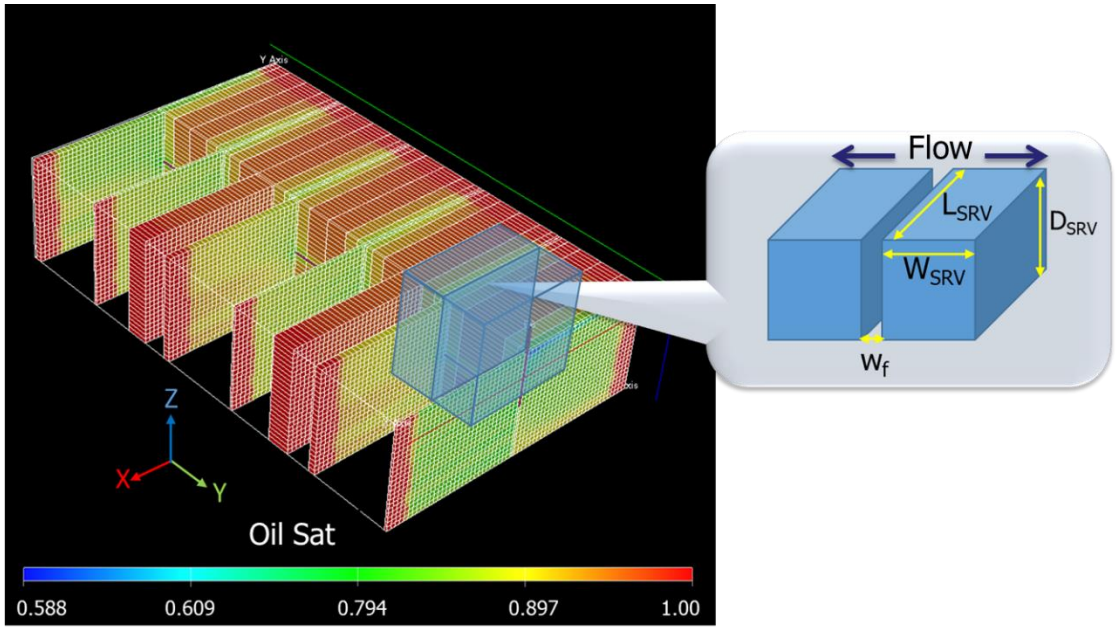

Fig. 4. 2—An example of Stimulated Reservoir Volume (SRV) and fracture model to visualize the simplified geometry for the diffusion model.

4.2 Oil Swelling Effect

The oil swelling depends on the composition and types of component of the fluid occupying the rock and the solvent and the thermodynamic behavior of the two fluid mixtures. Thus, the oil swelling can be simulated using a PVT simulator. In order to use the swelling factor in the diffusion model, we need the swelling factor at varying solvent concentration.

The swelling factor can be obtained through series of flash calculation in our in-house PVT Simulator. Since we consider miscible flow or a single-phase flow, the capillary pressure effect is not included. However, the impact of confinement is that single phase is achieved at lower pressures than in conventional reservoirs with pore sizes >100 nm. Therefore, the flash calculation is performed without the capillary pressure routine. This allows a shorter simulation run time. Traditionally, the swelling factor is calculated using volume at the bubble point pressure as the reference volume. Since we are assuming the pressure of the system does not change over soaking time period, the swelling factor at a constant pressure and temperature, usually in reservoir condition, for this chapter is defined as,

$$\text{Swelling Factor} = \frac{Volume\ of\ oil{-}solvent\ mixture\ at\ P_{res}}{Volume\ of\ original\ oil\ at\ P_{res}} \tag{4. 1}$$

Since we cap the solvent concentration to the maximum solubility of the solvent, we do not consider the solvent that vaporizes the oil. At our pressure range, this only happens at solvent concentration past 75%. Hence, the swelling factor at its constant pressure and temperature increases with solvent concentration as depicted in **Fig. 4. 3**. But

the maximum concentration is lower than 75% for systems at a pressure lower than 1,500 psi. This is possible because miscibility is not reached and the solvent is in a gas phase. The swelling factor increases with temperature as depicted in Fig. 4. 3. However, it does not always increase with higher pressure. The swelling factor is lower at 3,500 psi than that at 2,500 psi. It reveals that increasing the pressure further can form two phases and shrinks the oil volume at some point of pressure because the solvent partially vaporizes the oil, which becomes vaporizing gas drive dominant. However, we do not consider the evaporation of oil into gas phase in our model. From this preliminary result, we expect that the oil production is not significantly higher from increasing the pressure after a certain point with the same diffusion coefficient.

In addition, the effect of nitrogen in the oil swelling is not favorable for gas injection recovery process. **Fig. 4. 4** shows that nitrogen cannot swell the oil as much as carbon dioxide at the same pressure. This is the same effect as using pure CO_2 at pressures lower than 1,500 psi. Nitrogen injection also requires higher miscibility pressure than CO_2. The composition list of original oil used in Fig. 4. 3 and Fig. 4. 4 can be found in **Table 6. 5**.

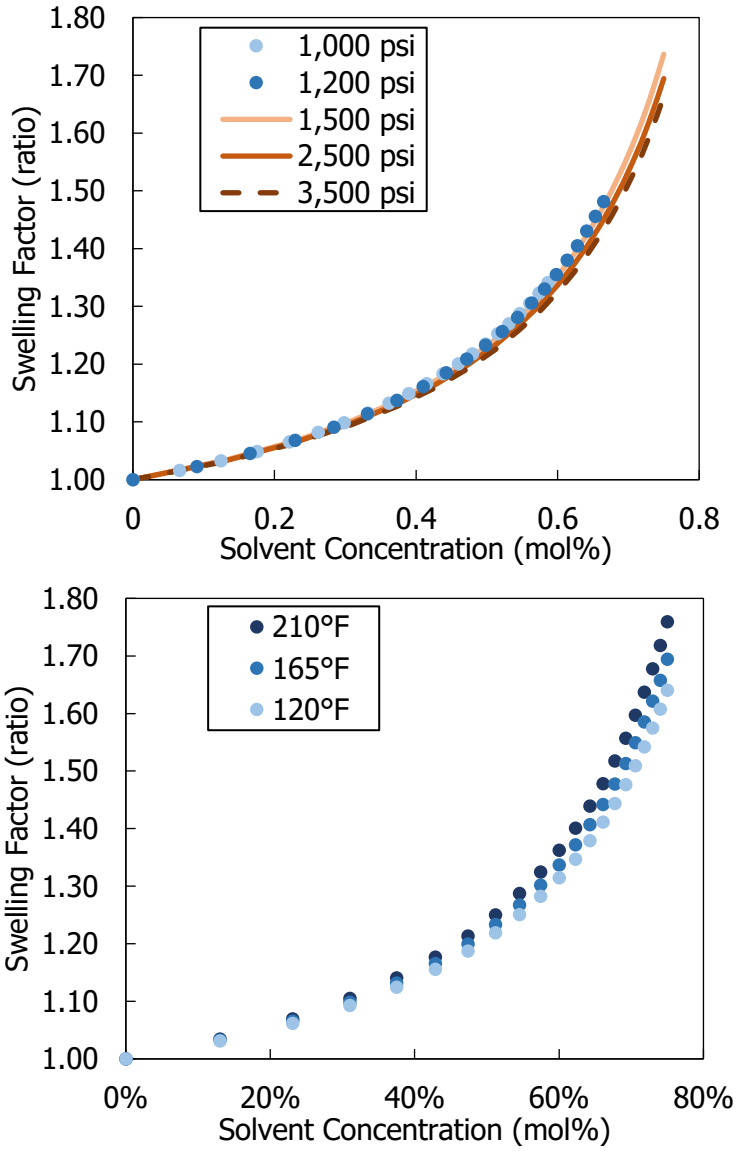

Fig. 4. 3—Swelling factor with increasing solvent concentration in liquid phase in mole fraction for varying pressure at 165 °F (upper) and for varying temperature at 2,500 psia (lower) using Oil 1 from Table 6. 5 as the reservoir fluid and pure CO_2 as the solvent.

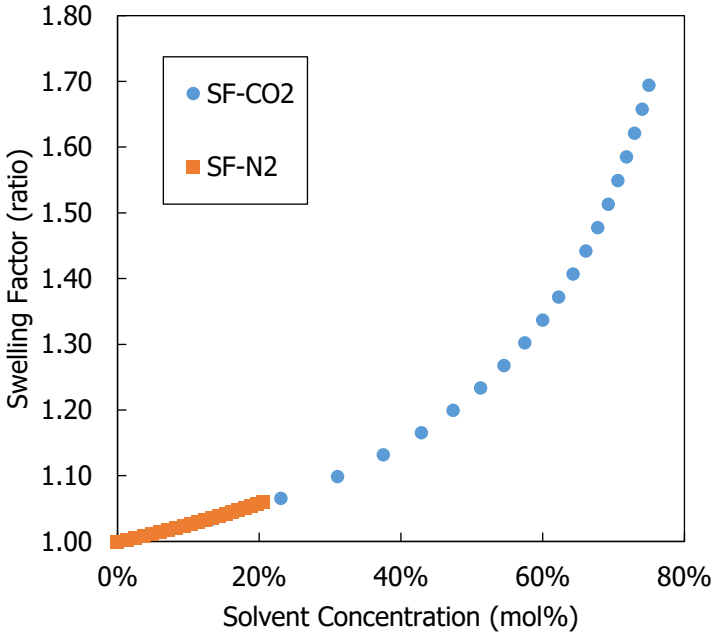

Fig. 4. 4—Swelling factor of the CO_2-Oil 1 mixture in blue markers and N_2-Oil 1 mixture in orange markers. This system is under 2,500 psia and 165 °F.

4.3 Diffusion-Convection Equation

Fick's laws of diffusion describe the equilibrium mixing of two fluids from high to low concentration over the concentration gradient that is driven by the random Brownian motion. The first law describes the diffusional flux,

$$J = -D_{\text{eff}} \nabla \cdot c \tag{4. 2}$$

where J is the diffusional flux, D_{eff} is the effective diffusion coefficient, and C is the solvent concentration. The effective diffusion coefficient is defined by:

$$D_{\text{eff}} = \frac{D}{\varepsilon} \tag{4. 3}$$

D is defined as the diffusion coefficient in bulk liquid phase and ε is the diffusive tortuosity factor of the liquid-saturated porous media. Du and Nojabaei (2019) summarized tortuosity of shale samples, measured by 3D tomographic imaging, with values ranging from 1.5 to 4.5 although shale rock is highly heterogenous that makes the tortuosity estimation more complex. They also suggested to obtain tortuosity and porosity relationship based on the lithology.

Since the diffusion process is in an unsteady-state, Fick's second law below describes the change in concentration with time, *t*.

$$\frac{\partial c}{\partial t} = D_{\text{eff}} \nabla^2 c \tag{4. 4}$$

In this study we only consider the one-dimensional diffusion flow. If we only consider the diffusion process without the velocity fluctuation, the governing differential equation can be expanded into Eq. (4. 5) for cylindrical system and Eq. (4. 6) for Cartesian system. The diffusion equation without the advection term can be solved analytically using separation of variables.

$$\frac{\partial c}{\partial t} = \frac{D_{\text{eff}}}{r} \frac{\partial}{\partial r} \left(r \frac{\partial c}{\partial r} \right) \tag{4. 5}$$

$$\frac{\partial c}{\partial t} = D_{\text{eff}} \frac{\partial^2 c}{\partial x^2} \tag{4. 6}$$

When the convective term is added, Eq. (4. 3) becomes Eq. (4. 7). Using the Fundamental Theorem of Calculus, the equation is expanded to Eq. (4. 8). In this chapter,

we only focus on the derivation using Cartesian system in Eq. (4. 9). The derivation using a cylindrical coordinate system can be found under the Appendix A.

$$\frac{\partial c}{\partial t} = D_{\text{eff}}\nabla^2 c - \nabla \cdot (c\vec{u}) \tag{4. 7}$$

$$\frac{\partial c}{\partial t} = D_{\text{eff}}\nabla^2 c - [c(\nabla \cdot \vec{u}) + \vec{u} \cdot \nabla c] \tag{4. 8}$$

$$\frac{\partial c}{\partial t} = D_{\text{eff}}\frac{\partial^2 c}{\partial x^2} - c\frac{\partial u}{\partial x} - u\frac{\partial c}{\partial x} \tag{4. 9}$$

The volume expansion of oil is calculated based on the cell pore volume and swelling factor within the cell as describe in Eq. (4. 10). The change in velocity in Eq. (4. 11) is defined by the change in flow rate over the cross-sectional area (Li & Dong 2009). This equation is the transmissibility between two cells. We substitute the flow rate into volume and use the definition of change in volume with the previous equation. The velocity is the integral of the change in velocity. In discretized form, the integral becomes a summation in Eq. (4. 12). The term $c_{x+\Delta x}^{t+\Delta t}$ means the concentration at $x + \Delta x$ distance and $t + \Delta t$ time.

$$\Delta V_e = \phi wh\Delta x\left[f\left(\frac{c_{x+\Delta x}^{t+\Delta t} + c_x^{t+\Delta t}}{2}\right) - f\left(\frac{c_{x+\Delta x}^{t} + c_x^{t}}{2}\right)\right] \tag{4. 10}$$

$$\begin{aligned}\Delta u_{x+\Delta x}^{t+\Delta t} &= \frac{\Delta V_e}{wh(x+\Delta x)\Delta t} \\ &= \frac{\phi\Delta x}{(x+\Delta x)\Delta t}\left[f\left(\frac{c_{x+\Delta x}^{t+\Delta t} + c_x^{t+\Delta t}}{2}\right) - f\left(\frac{c_{x+\Delta x}^{t} + c_x^{t}}{2}\right)\right]\end{aligned} \tag{4. 11}$$

$$u_{x+\Delta x}^{t+\Delta t} = \sum_{x=0}^{x+\Delta x} \Delta u_{x+\Delta x}^{t+\Delta t} \tag{4. 12}$$

The boundary condition and initial condition is shown in Eq. (4. 13) and Eq. (4. 14). The illustration of the boundary condition for the two coordinate systems can be found in Fig. 4. 1. The maximum solvent concentration, c_0, is arbitrarily predetermined in the simulation to be 75% solvent concentration in mol percentage at a fixed pressure. The c_0 can also be proposed as the maximum concentration at the bubble point pressure. However, we use the former option in order to be consistent in the study. We assume the maximum solvent concentration is reached at the interface between the fracture and the matrix. The change in solvent concentration and the velocity yields to zero at the furthest from the source.

Boundary Conditions:

$$c = c_0, \text{ at } x = 0$$
$$u = 0, \frac{\partial c}{\partial x} = 0, \text{ at } x = x_0 \tag{4. 13}$$

Initial Conditions:

$$c = c_0 \text{ at } x = 0, t = 0$$
$$c = c_i \text{ at } x > 0, t = 0 \tag{4. 14}$$
$$u = 0 \text{ at } x = x_0, t = 0$$

To solve the diffusion equation, we need to utilize dimensionless variable. The definition of each variables is found in Eq. (4. 15).

$$\bar{x} = \frac{x}{x_0} \qquad \bar{c} = \frac{c - c_i}{c_0 - c_i}$$
$$\bar{u} = \frac{u}{D_{\text{eff}}/x_0} \qquad \tau = \frac{t}{{x_0}^2/D_{\text{eff}}} \tag{4. 15}$$

After we substitute the dimensionless variables into the diffusion equation and the velocity equation in Eq. (4. 9) and Eq. (4. 11), we obtain Eq. (4. 16) and Eq. (4. 17).

$$\frac{\partial \bar{c}}{\partial \tau} = \frac{\partial^2 \bar{c}}{\partial \bar{x}^2} - \bar{c}\frac{\partial \bar{u}}{\partial \bar{x}} - \bar{u}\frac{\partial \bar{c}}{\partial \bar{x}} \tag{4. 16}$$

$$\Delta \bar{u}_{\bar{x}+\Delta\bar{x}}^{\tau+\Delta\tau} = \frac{\phi \Delta \bar{x}}{(\bar{x}+\Delta\bar{x})\Delta\tau}\left[f\left(\frac{\bar{c}_{\bar{x}+\Delta\bar{x}}^{\tau+\Delta\tau} + \bar{c}_{\bar{x}}^{\tau+\Delta\tau}}{2}(c_0 - c_i)\right) - f\left(\frac{\bar{c}_{\bar{x}+\Delta\bar{x}}^{\tau} + \bar{c}_{\bar{x}}^{\tau}}{2}(c_0 - c_i)\right)\right] \tag{4. 17}$$

The initial and boundary condition in Eq. (4. 13) and Eq. (4. 14), become Eq. (4. 18) and Eq. (4. 19). The dimensionless equation is then discretized and solved using finite difference method. Further details can be found in the Appendix. The work flow to solve the diffusion model in the PVT Simulator is explained in **Fig. 4. 5**.

Dimensionless Boundary Conditions:

$$\bar{c} = 1, \text{ at } \bar{x} = 0$$
$$\bar{u} = 0, \frac{\partial \bar{c}}{\partial \bar{x}} = 0, \text{ at } \bar{x} = 1 \tag{4. 18}$$

Dimensionless Initial Conditions:

$$\bar{c} = 1 \text{ at } \bar{x} = 0, \tau = 0$$

$$\bar{c} = 0 \text{ at } \bar{x} > 0, \tau = 0 \tag{4. 19}$$

$$\bar{u} = 0 \text{ at } \bar{x} = 1, \tau = 0$$

The swollen volume under reservoir condition at time *t* is calculated as Eq. (4. 20) for Cartesian system. The swelling factor is a function of the solvent concentration, defined by $f(c_i^t)$. This is the amount of excess volume that is produced with the solvent in the solution. Eq. (4. 21) describes the volume of solvent stored in the matrix by integrating the solvent concentration. For this study, we do not estimate the amount of solvent adsorbed from the stored solvent.

$$V_{s,total}(P_{res}, T_{res})(t) = \sum_{i=1}^{Ncell} \left(f\left(c_i^t\right) - 1\right)\Delta x_i * V_p \tag{4. 20}$$

$$V_{sol,stored}(P_{res}, T_{res}) = \int_0^1 c(\bar{x})d\bar{x} * V_p \tag{4. 21}$$

Since we are assuming that the volume produced have the maximum solvent concentration (c_0), the solvent produced in moles ($n_{sol,prod}$) is $V_{s,total}(P_{res}, T_{res})$ multiplied by $c_0(P_{res}, T_{res})$, which can also be expressed in Eq. (4. 22) and Eq. (4. 23). The volumes at reservoir condition are converted to moles.

$$n_{max,prod} = \frac{V_{s,total}(P_{res}, T_{res})}{\tilde{V}_{m,max}^{l}(P_{res}, T_{res})} \tag{4. 22}$$

$$n_{sol,prod} = n_{max,prod} \times z_{c_0} \tag{4. 23}$$

$$n_{oil,prod} = n_{mix,prod} - n_{sol,prod} \tag{4. 24}$$

Thus, recovery factor can simply be expressed as in Eq. (4. 25) since the reservoir pressure and temperature are assumed constant. By calculating the swollen volume this way, higher swelling factor produces higher recovery factor. Eq. (4. 26) shows the definition of gross solvent utilization at standard condition of 14.7 psia and 60°F.

$$Recovery\ Factor = \frac{n_{oil,prod}}{n_{oil,initial}} \tag{4. 25}$$

$$Gross\ Utilization = \frac{V_{sol,prod}(P_{SC}, T_{SC}) + V_{sol,stored}(P_{SC}, T_{SC})}{V_{oil,prod}(P_{SC}, T_{SC})} \tag{4. 26}$$

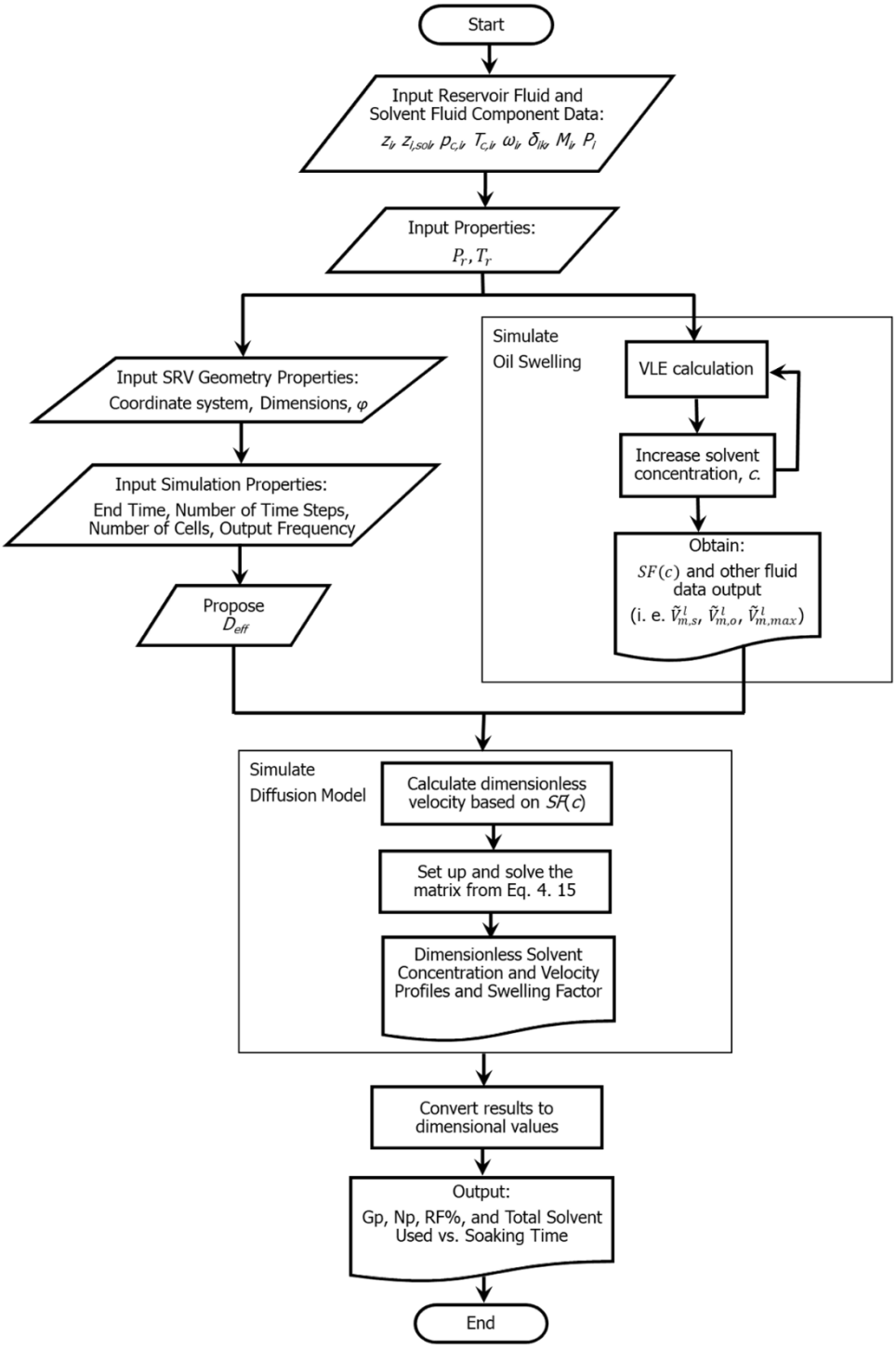

Fig. 4. 5—Flow chart of diffusion model simulation in the PVT Simulator

4.4 Results and Discussion

The results presented in this section are based on the numerical simulation using Oil 1 as the in-situ fluid and pure carbon dioxide (CO_2) as the solvent. The fluid composition of Oil 1 based on Tovar's huff-soak-puff core experiment is listed in **Table 6. 5** within Chapter VI. In **Fig. 4. 6** to **Fig. 4. 11**, the diffusion time is set to be for 24 hours and the effective diffusion coefficient is 5.0E-6 cm^2/s for a consistent analysis. Also, Oil 1 and solvent mixture swelling data is obtained at 2,500 psia and 165°F.

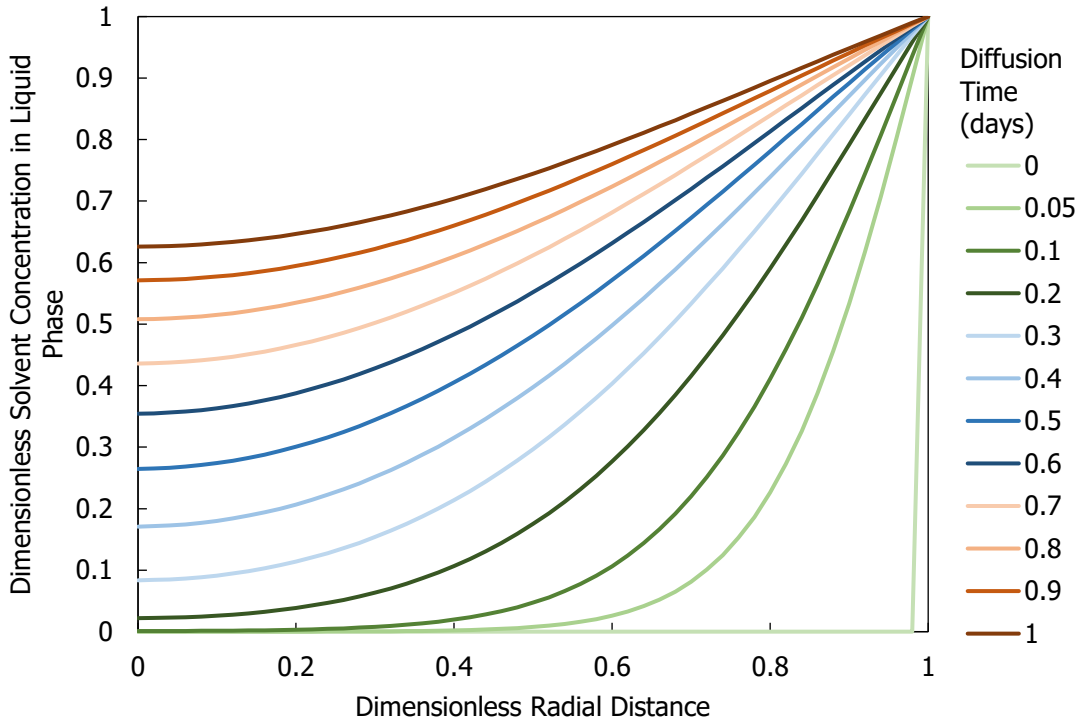

Fig. 4. 6—Changing solvent concentration profile in a cylindrical coordinate system over 24 hours of diffusion time. This test uses Oil 1 from Table 6. 5 as the reservoir fluid, CO_2 as the solvent, and 5.0E-6 cm^2/s as the diffusion coefficient at 2,500 psia and 165°F.

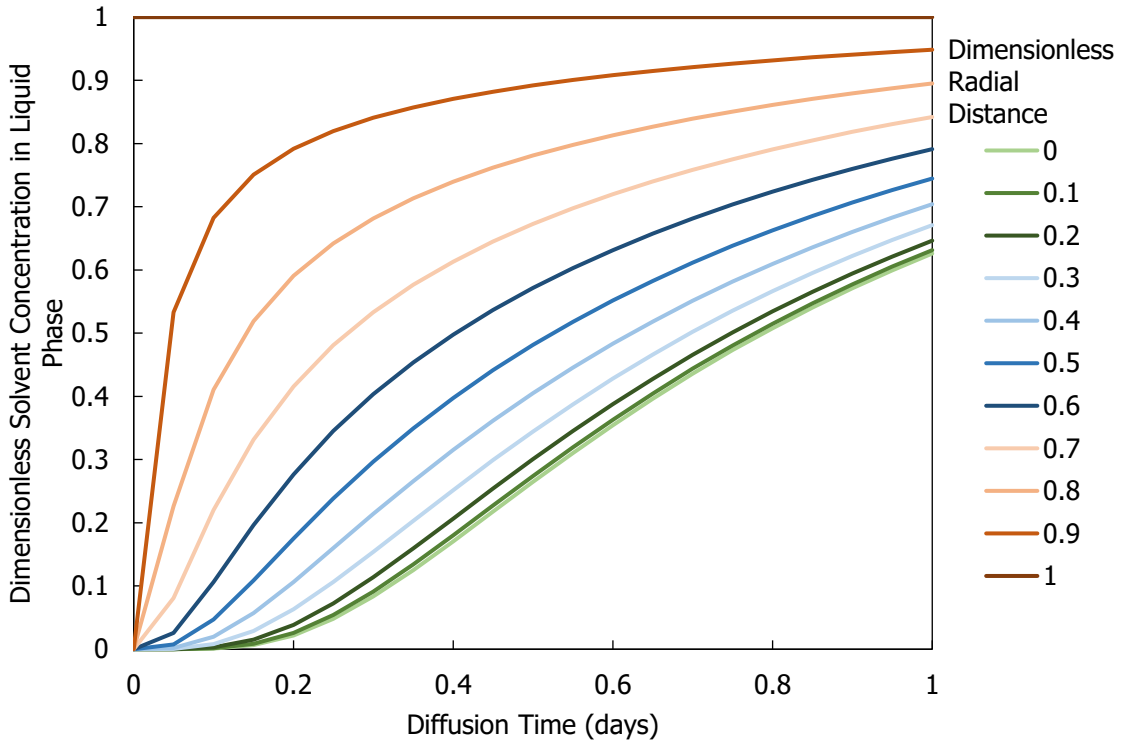

Fig. 4. 7—Changing solvent concentration profile in a cylindrical coordinate system at varying radii. This test uses Oil 1 as the reservoir fluid, CO_2 as the solvent, and 5.0E-6 cm^2/s as the diffusion coefficient at 2,500 psia and 165°F.

We can observe the solvent concentration profile over a specific time at a diffusion coefficient from simulating the diffusion process. An example of this can be found in **Fig. 4. 6** and **Fig. 4. 7** for the cylindrical coordinate system and in **Fig. 4. 9** and **Fig. 4. 10** for Cartesian coordinate system. Observing in dimensionless variables is more appropriate for the solvent concentration and the distance. It shows that the solvent concentration can reach the maximum concentration after a certain period.

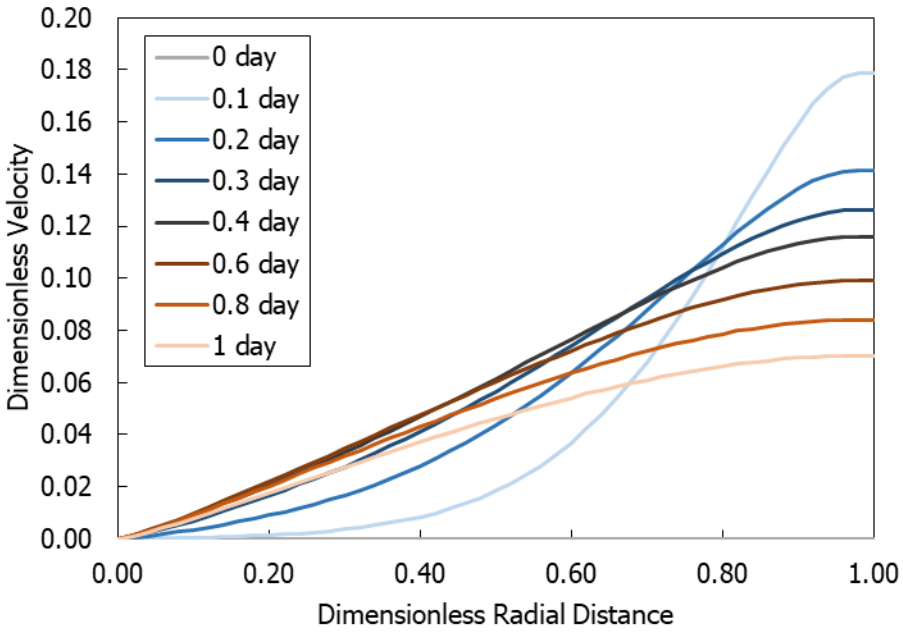

Fig. 4. 8— Dimensionless velocity profile in a cylindrical coordinate system over 24 hours of diffusion time. This test uses Oil 1 as the reservoir fluid, CO_2 as the solvent, and 5.0E-6 cm^2/s as the diffusion coefficient at 2,500 psia and 165°F.

When we consider the convective term, we can observe the dimensionless velocity profile in **Fig. 4. 8** for the cylindrical coordinate system and **Fig. 4. 11** for Cartesian coordinate system. Both figures imply that the velocity fluctuation dissipates after a certain period. The crossover of the dimensionless velocity indicates that the velocity approaches to zero faster at earlier times where the diffusive flux is faster. It causes the solvent concentration falls to zero faster at earlier times. Also, larger dimensionless velocity closest to the source approaches to zero more rapidly.

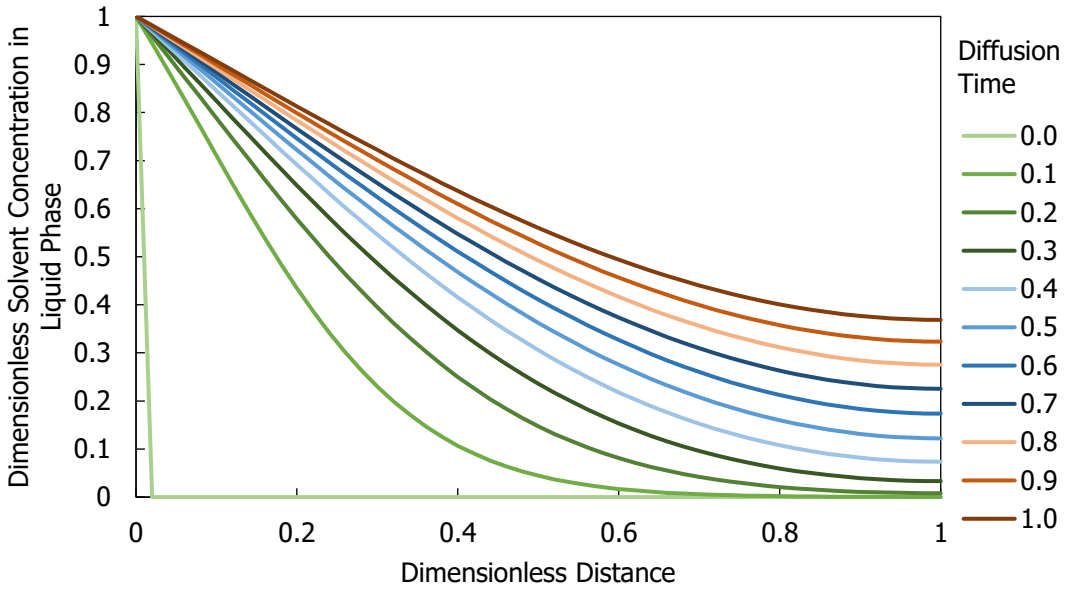

Fig. 4. 9—Changing solvent concentration profile in a Cartesian coordinate system over 24 hours of diffusion time.

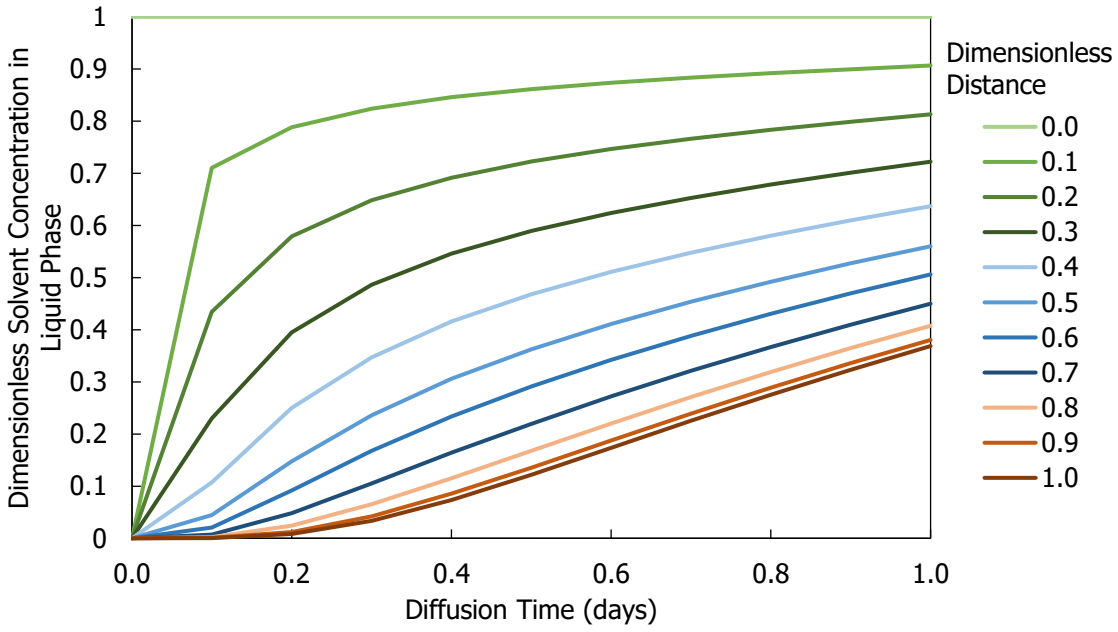

Fig. 4. 10—Changing solvent concentration profile in a Cartesian coordinate system at varying distance from the source of the solvent.

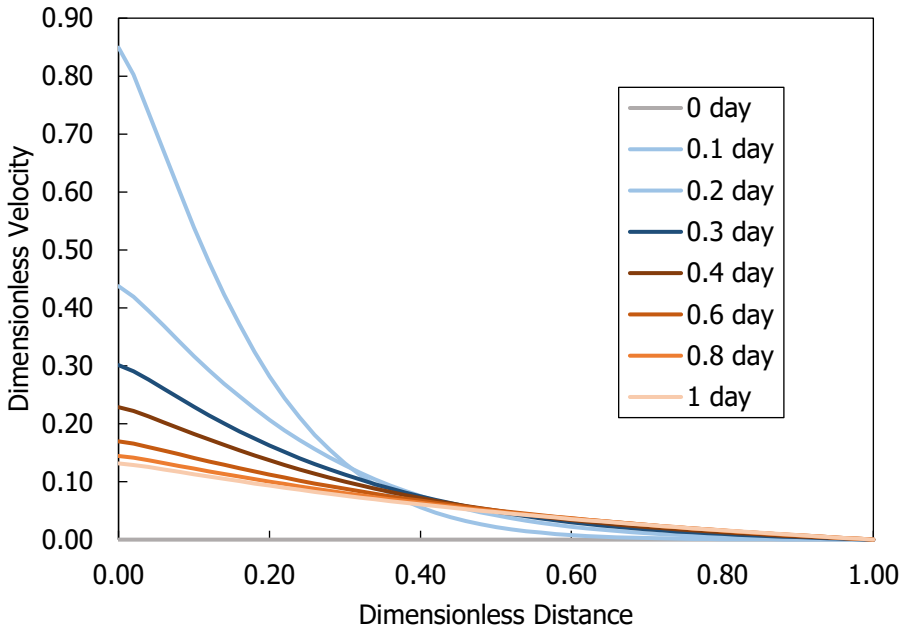

Fig. 4. 11—Dimensionless velocity profile in a Cartesian coordinate system over 24 hours of diffusion time. This test uses Oil 1 as the reservoir fluid, CO_2 as the solvent, and 5.0E-6 cm^2/s as the diffusion coefficient at 2,500 psia and 165°F.

The diffusion process in Cartesian system takes longer to achieve the same recoveries as in the cylindrical system as implied from **Fig. 4. 12**. With the same effective diffusion coefficient, same stimulated reservoir volume (SRV), and same flow distance ($r_0 = x_0$), the recovery factor in cylindrical system is higher than the recovery in Cartesian system over the same period. However, the recovery per unit contact area in Cartesian system is higher after about 14 hours than that in cylindrical system. The solvent takes longer to penetrate into the matrix in Cartesian system than in cylindrical system. It is one of the challenges in scaling up the lab experiment into the field. The contact area of the core flooding experiment is higher than the ones in the field. Thus, the lab experiment can overestimate the recovery results.

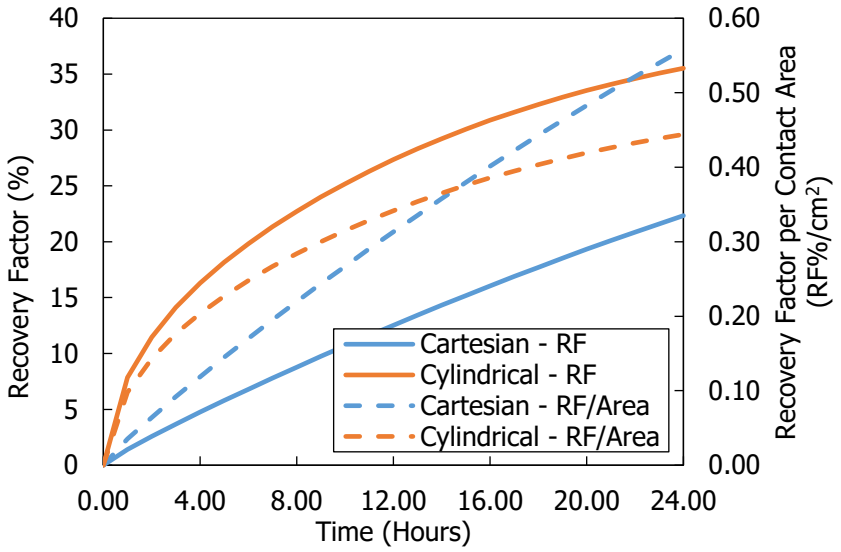

Fig. 4. 12—Recovery factor in Cartesian (blue line) and cylindrical (orange line) coordinate system over time in hours. This test uses Oil 1 as the reservoir fluid, CO_2 as the solvent, and 5.0E-6 cm^2/s as the effective diffusion coefficient at 2,500 psia and 165°F.

Since the fluid dictates the diffusion coefficient, D_{eff}, and is dictated by the pressure, temperature, and the EOS, the dimensionless solvent concentration over time and space would not change with pressure for the same diffusion coefficient. We need to observe the change in solvent concentration, recovery factor, and amount of solvent used at various diffusion coefficients.

When we compare the effect of diffusion coefficients on the concentration profile within same period, **Fig. 4. 13** shows, as expected, that the solvent concentration increases with higher effective diffusion coefficient. Also, **Fig. 4. 14** shows the concentration at the same radius over time. The solvent concentration with diffusion coefficient 1.00E-6 is

significantly lower and more gradual than the other profiles. It indicates that a higher diffusion coefficient may not change the concentration significantly as the lower one.

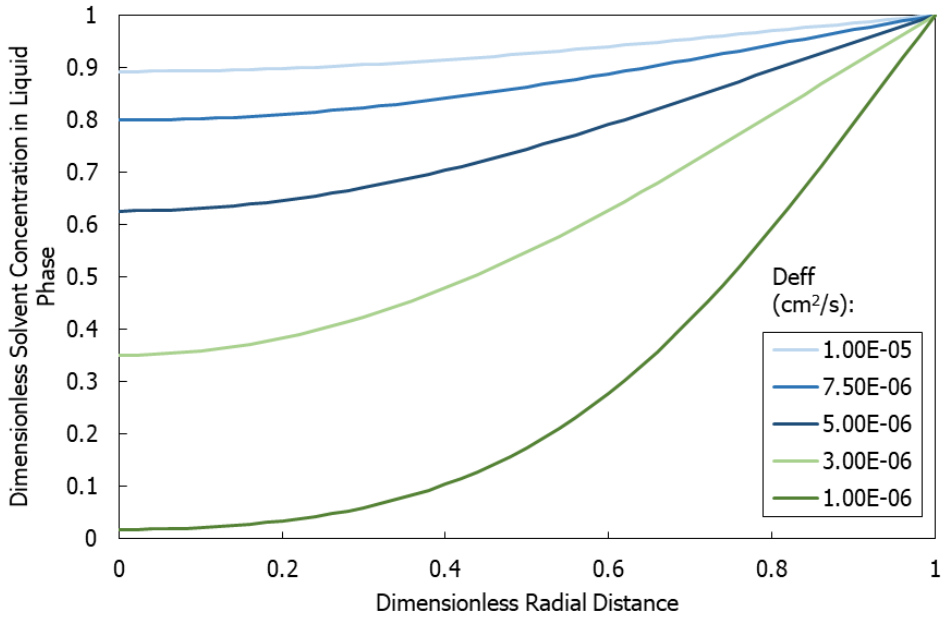

Fig. 4. 13—Concentration profile after 24 hours diffusion time using different effective diffusion coefficient. The test uses Oil 1 (Table 6. 5) as the reservoir fluid and CO_2 solvent at 2,500 psia and 165 °F.

In **Fig. 4. 15**, a higher diffusion coefficient affects the recovery positively. This analysis coincides with the increasing solvent concentration with a higher diffusion coefficient. The swelling factor increases with solvent concentration in the liquid phase at the same pressure, which means larger excess volume to recover. Other than recovery factor, the solvent's gross utilization in **Fig. 4. 16** is lower using a higher diffusion coefficient, but the pore volume injected is higher at a higher diffusion coefficient. The solvent stored in the matrix is calculated based on the integral of the concentration gradient times the pore volume. Gross utilization factor is the total volume of solvent used (stored and reproduced) divided by the total amount of oil produced in standard condition. Pore

volume injected is the total volume of solvent used per total pore volume in the matrix. The reason for the phenomena in **Fig. 4. 16** is that the solvent permeates into the matrix (higher concentration gradient) and is stored more at higher diffusion coefficient. It also means that higher diffusivity leads to larger mass of solvent can be stored in the matrix in liquid form, but it still allows higher oil production.

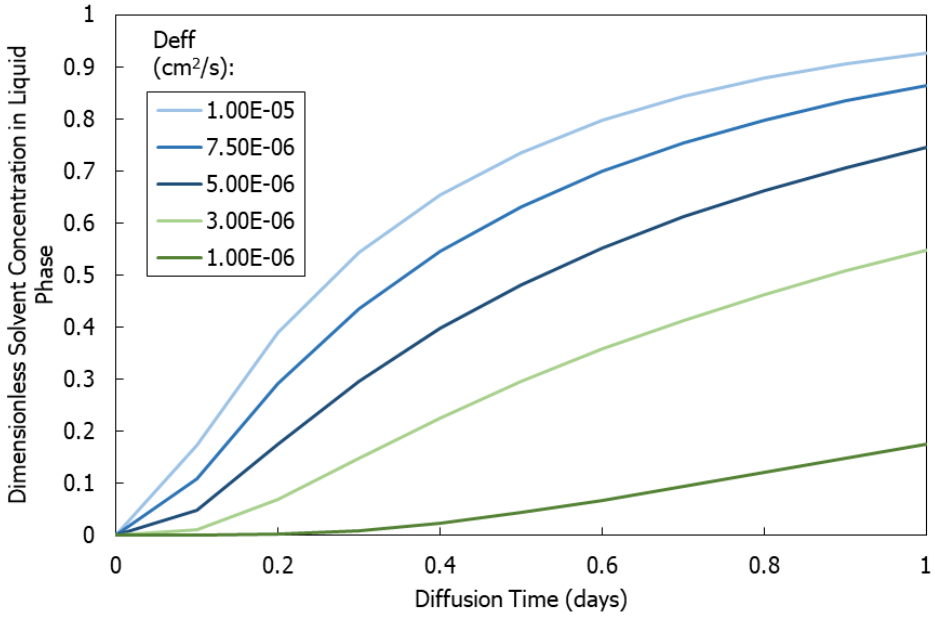

Fig. 4. 14—Solvent concentration over 24 hours diffusion time at dimensionless radial distance of 0.5, or the midpoint, using different effective diffusion coefficient. The test uses Oil 1 from Table 6. 5 as the original oil and CO_2 as the solvent at 2,500 psia and 165°F.

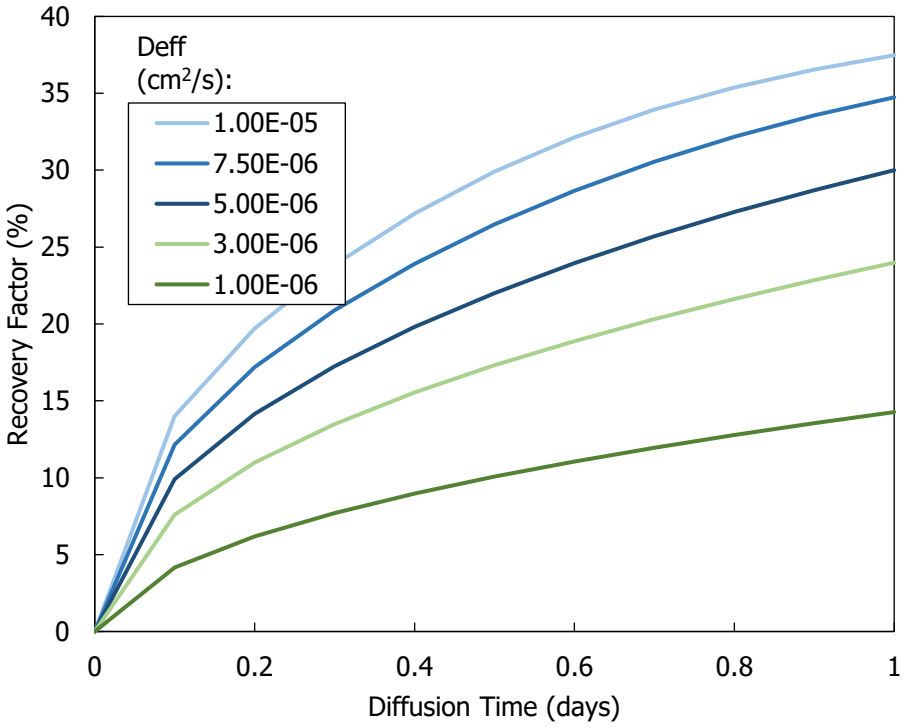

Fig. 4. 15—Recovery factor after 24 hours of soaking time using different effective diffusion coefficient. The test uses Oil 1 as the original oil and CO_2 as the solvent at 2,500 psia and 165 °F.

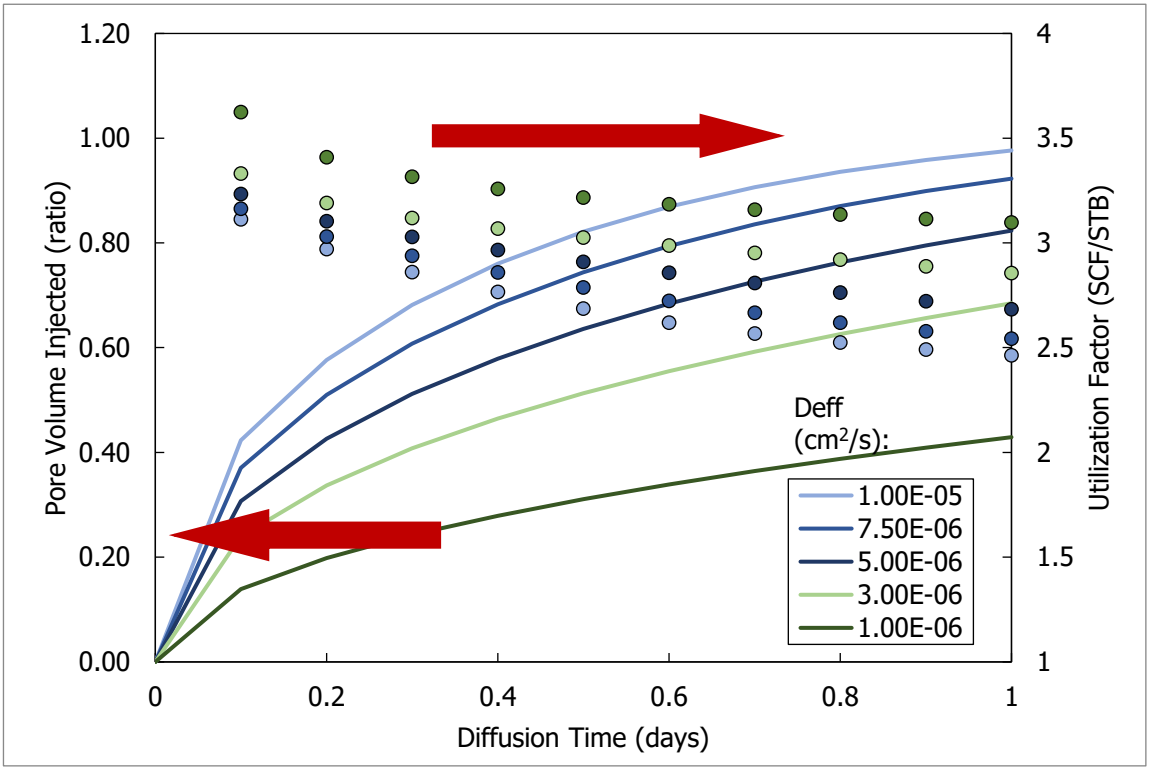

Fig. 4. 16—Pore volume injected (lines) and gross utilization factor in SCF/STB (markers) after 24 hours of soaking time using different effective diffusion coefficient. The test uses Oil 1 as the original oil and CO_2 as the solvent at 2,500 psia and 165 °F.

Fig. 4. 17 and **Fig. 4. 18** presents the recovery factor, solvent used, and pore volume injected at various pressure and temperature at the same diffusion coefficient and diffusion time. The trend in **Fig. 4. 19** is similar to the maximum swelling factor in Fig. 4. 3 because of the way the recovery is calculated as shown in Eq.(4. 20) to Eq.(4. 25). We can conclude that higher pressure does not yield to higher recovery factor when we restrict to same effective diffusion coefficient. However, the effective diffusion coefficient realistically changes with pressure. So, comparing the recovery factor at different pressures is invalid when using the same diffusivity constant. In order to determine the diffusion coefficient,

we need to match the recovery factor from a published data with our estimation using the corresponding diffusion coefficient.

In order to see the effect of pressure and temperature on the diffusion coefficient we need laboratory data that can match the recoveries with the simulation results. This topic is discussed in Chapter V.

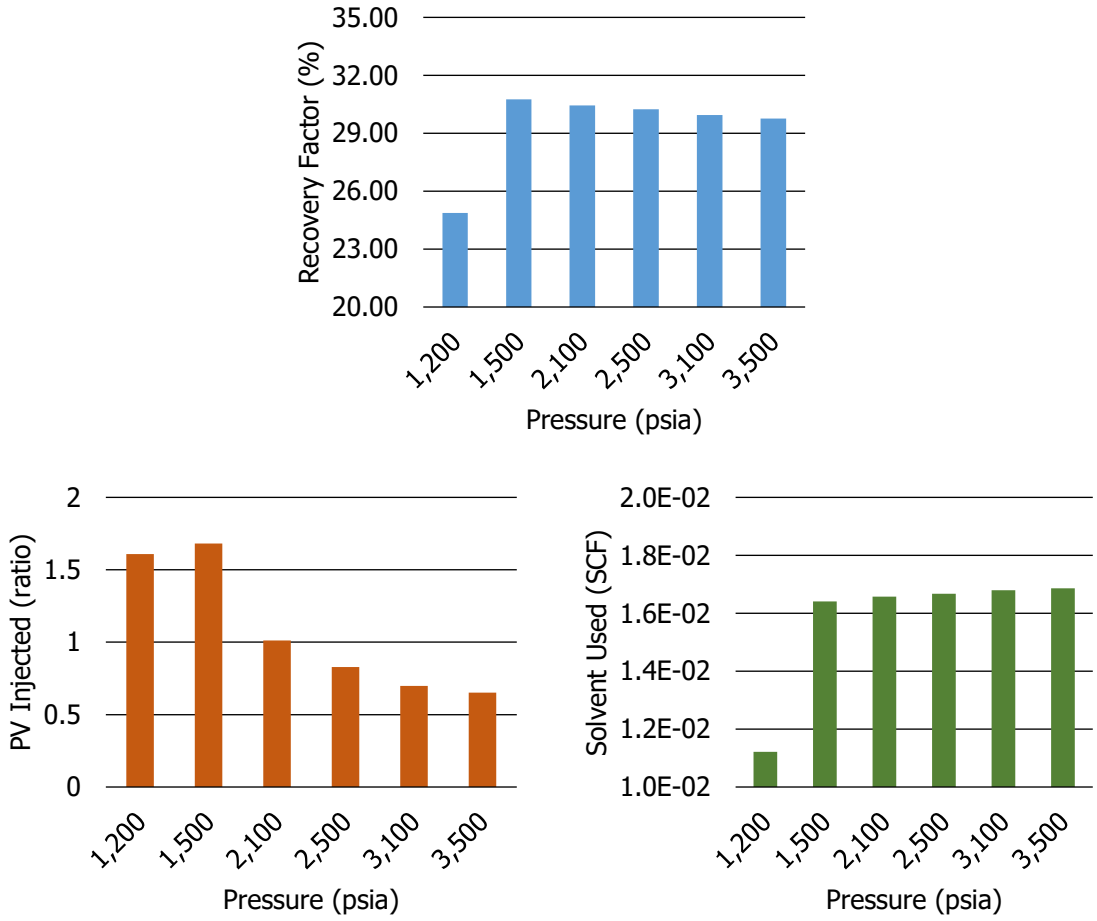

Fig. 4. 17—Effect of constant pressure on the recovery factor (top), the amount of solvent used (right), and the pore volume injected (left) after 24 hours of diffusion time using effective diffusion coefficient of 5.0E-6 cm^2/s and temperature of 165 °F. The test uses Oil 1 as the reservoir fluid and pure CO_2 as the solvent.

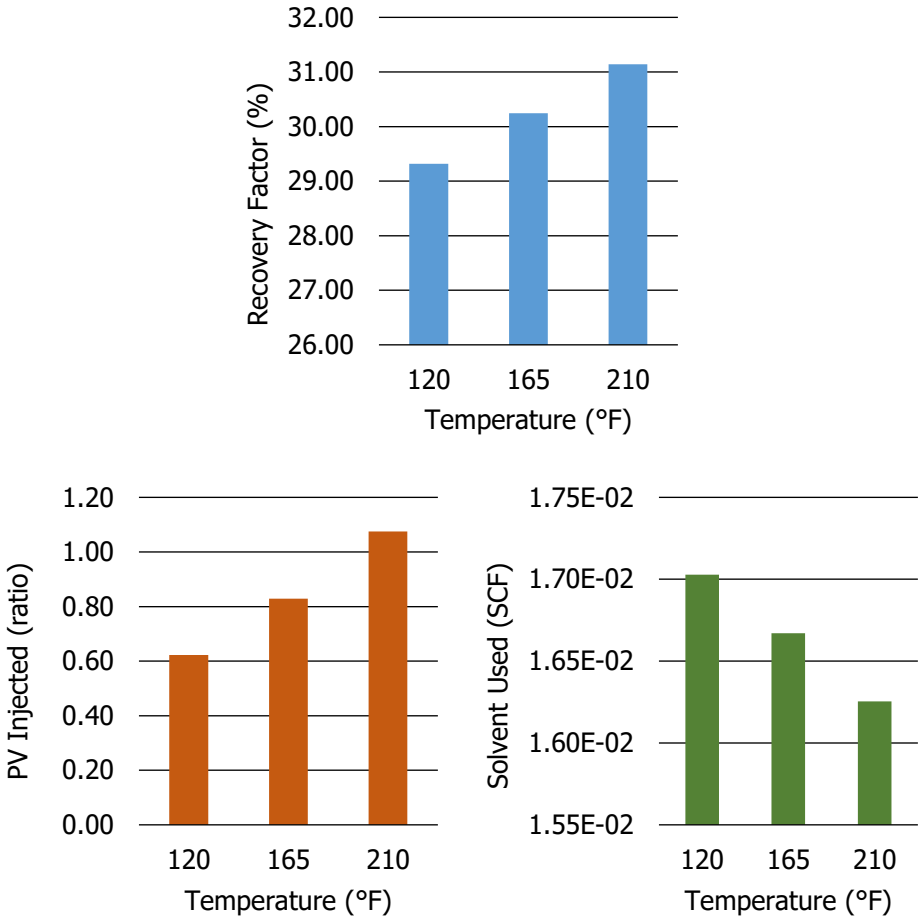

Fig. 4. 18—The effect of temperature on the recovery factor (top), the amount of solvent used (right), and the pore volume injected (left) after 24 hours of diffusion time using an effective diffusion coefficient of 5.0E-6 cm^2/s and pressure of 2,500 psia. The test uses Oil 1 as the reservoir fluid and pure CO_2 as the solvent.

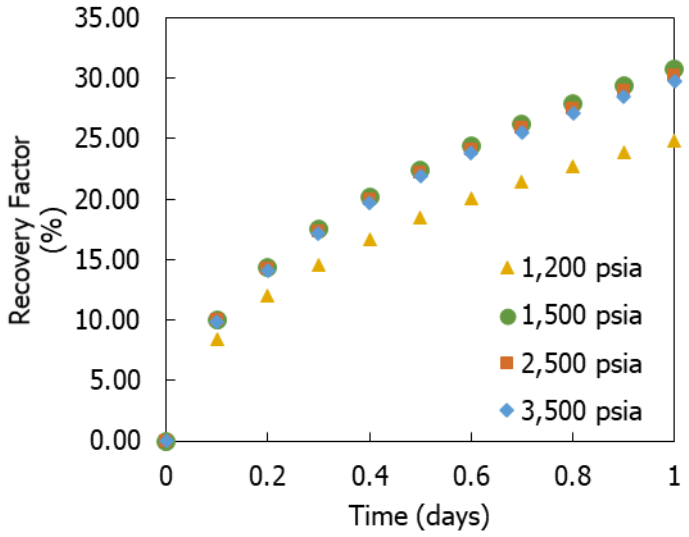

Fig. 4. 19—Effect of pressure on the recovery factor after 24 hours of diffusion time using effective diffusion coefficient of 5.0E-6 cm^2/s. The test uses Oil 1 as the reservoir fluid and pure CO_2 as the solvent.

Another similarity in recovery to the swelling factor trend is when we change the solvent component used. The type of solvent used dramatically affects the performance of the solvent injection process. Using nitrogen as the solvent is not recommended as **Fig. 4. 20** shows, the oil recovery using nitrogen, N_2, is around 5% as opposed to the 32% obtained using carbon dioxide, CO_2 at the same effective diffusion coefficient. Tovar et al. (2018a) also obtained almost zero recovery from using nitrogen solvent in his huff-soak-puff experiment, which validates our model. The pore volume injected (PVI) increases with oil recovery. Pore volume injected is defined by the total amount of solvent used per pore volume where the amount of solvent used are calculated based on the solvent concentration in liquid phase of the produced and stored oil-solvent mixtures. The maximum solvent concentration in liquid phase of CO_2 is larger than that of N_2, which explains the trend in Fig. 4. 20. If the pore volume injected of nitrogen were increased, the

nitrogen and oil mixture would only be partially miscible. Partially miscible condition changes the driving mechanism, but we only focus on miscible condition in this study.

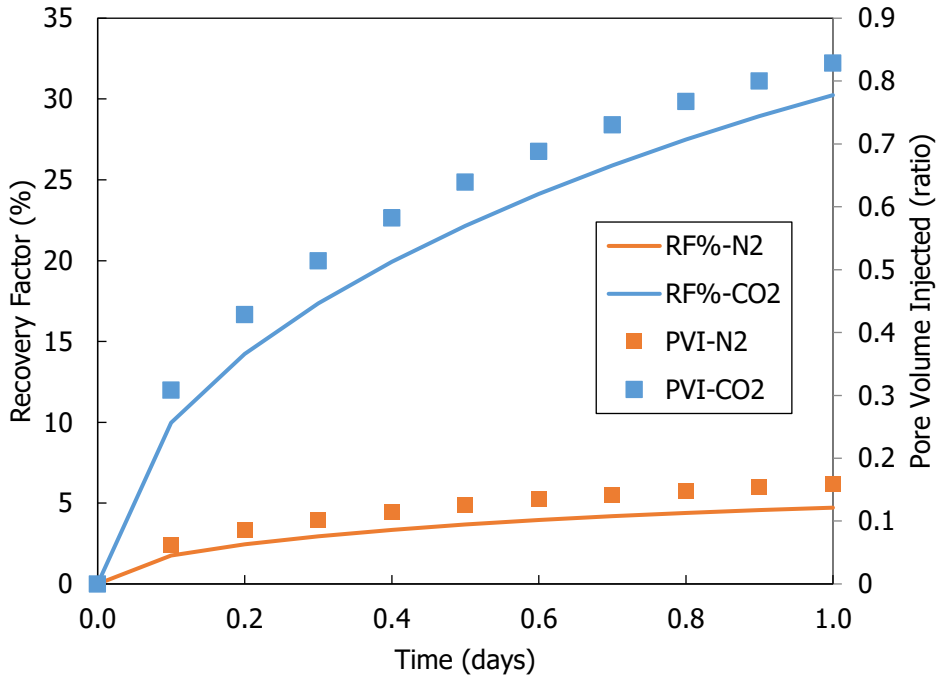

Fig. 4. 20—The effect in recovery factor and pore volume injected with pure CO_2 and pure N_2 at 2,500 psi after 24 hours of soaking time.

To prove that the primary mechanism is molecular diffusion, we present **Fig. 4. 21**. The oil swelling creates the velocity difference that requires the convective term into the diffusion equation. Without the convective term, the oil swelling only affects the excess production of the oil and solvent mixture. As depicted in Fig. 4. 21, the difference in recovery factor between with and without convection term in the diffusion model is more significant at a lower effective diffusion coefficient. However, the difference is relatively small. Also, the recovery is slightly higher when we only consider molecular diffusion term

than when we additionally add convective term. The convective term is added because we assume the swelling induces the velocity at the opposite direction if the flow. It hinders the diffusion process and lowers the recovery.

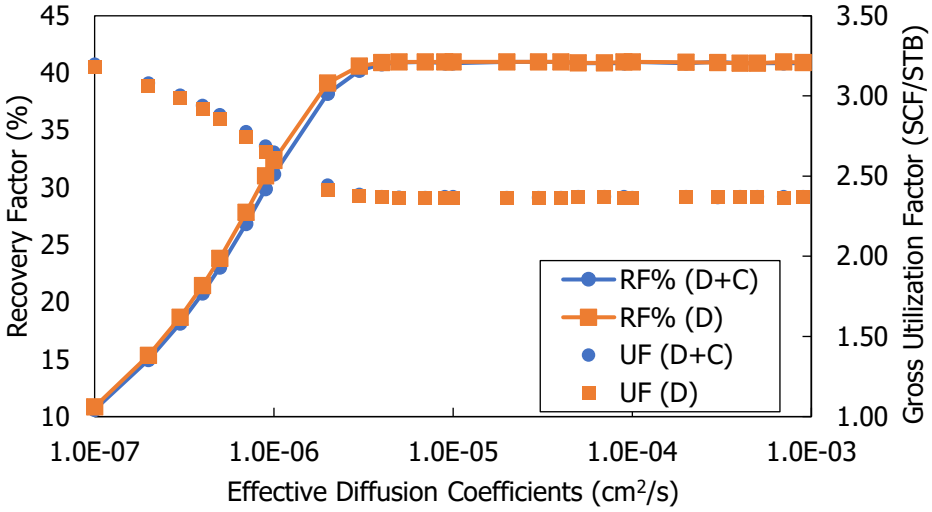

Fig. 4. 21—The effect in recovery factor and gas utilization with convective term (D+C) and without the convective term (D) at 3,500 psi after 132 hours of soaking time.

CHAPTER V

VALIDATION OF MODEL AND APPLICATION

This chapter discusses the validity and the recommended application of the models used in the study. Our MMP estimation results in Chapter III are compared to the MMP estimations from a commercial simulator. The diffusion model is tested using experimental setup by Tovar et al. (2018a) and compared according to the recovery data. We explain the limitations and emphasize the underlying assumptions in our models.

5.1 MMP Estimation

The results of the MMP estimation using multiple-mixing-cells method are presented in **Table 3. 2** to **Table 3. 4**. The MMP comparison is only appropriate for the bulk case since commercial simulators have not implemented the capillary pressure effect in their MMP estimation algorithm. We use slim-tube simulation in a commercial PVT simulator, *PVTSim Nova 4*, as the reference MMP estimation method for bulk condition. The MMP obtained from slim-tube simulation is described in **Fig. 5. 1** and **Fig. 5. 2**. The MMP lies in the intersection between the two extrapolated lines, which indicates the sharp increase in recovery factor.

For pure CO_2 solvent in synthetic oil case in Table 3. 2 with bulk MMP of 2,268 psia, the reference MMP is 2,190 psia, as shown in **Fig. 5. 1**. For Table 3. 3 for pure CO_2 in Eagle Ford Fluid with bulk MMP of 2,330 psia, the reference MMP is 2,300 psia. The result using 50 contacts has the least error for both cases. For Table 3. 4 for pure CO_2 in Eagle Ford Fluid with bulk MMP of 2,790, the reference MMP is 2,730 psia, as shown in

Fig. 5. 2. Although the difference is not as significant from 50 to 75 contacts, the 75 contacts case still has the closest value to the reference MMP. Thus, higher number of contacts produces more accurate results.

The drawback of this method is that the sufficient minimum number of contacts cannot be predicted because it highly depends on the fluid composition. Another disadvantage is that adding the coupled EOS with capillary pressure increases the computational time, especially when involving more fluid components. Also, the trial pressure is determined by linear extrapolation that tends to overestimate the MMP. We also tried to test using Oil 1 from **Table 6. 5** as the original oil with CO_2 solvent, but the MMP cannot be found because the fluid has high amount of heavy components and very low bubble point pressure.

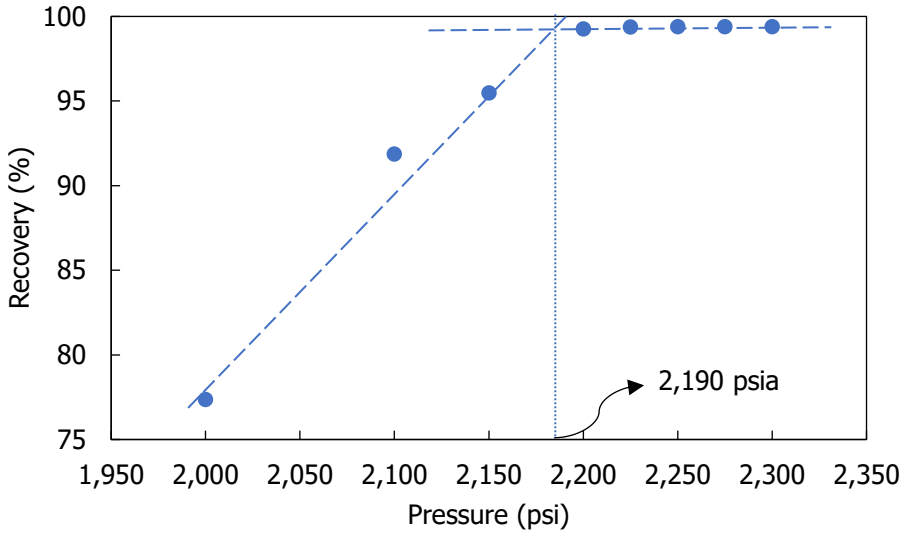

Fig. 5. 1—Slim-tube simulation result from *PVTSim Nova 4* for the pure CO_2 injection to the synthetic oil at 200°F. The intersection at 2,190 psia is the MMP estimation.

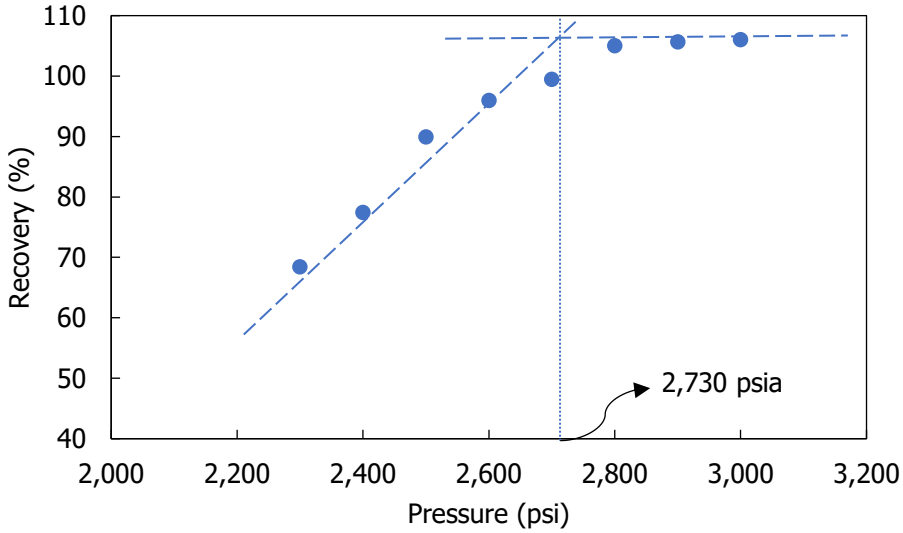

Fig. 5. 2—Slim-tube simulation result from *PVTSim Nova 4* for the CO_2/CH_4 injection to the synthetic oil at 200°F. The intersection at 2,730 psia is the MMP estimation.

5.2 Matching Effective Diffusion Coefficients

The following approach involves matching the recovery data from the existing experimental data (Tovar et al. 2018b) by finding the appropriate effective diffusion coefficient. We simulated one of Tovar's huff-soak-puff experiments, as described in **Fig. 5. 3**, and matched the recovery factor at the end of the stage, or after all 4 cycles in this case. Tovar et al. used 100% oil saturated core samples and CO_2 solvent for the constant pressure huff-soak-puff experiment. The applied temperature was 165°F while varying pressure were tested for different samples, ranging from 1,000 psia to 3,500 psia. To resemble the propped fractures, they used glass beads surrounding the core sample.

Our results are summarized in **Fig. 5. 4**. **Fig. 5. 5** shows the flow chart of finding the effective diffusion coefficient. In the PVT Simulator, we would use 84 hours of soaking time to simulate the 4 cycles of 21 hours soaking time. The first cycle in the lab tends to produce more oil than the following cycles whereas the simulation have less sharp decrease between each cycle. The recovery factor does not have linear relationship to the number of cycles and soaking hours. The "puff" or the production period is a possible reason for the difference in recoveries from the simulation in each cycle. In Tovar's experiment, the oil-CO_2 mixture after the soaking period is produced by sweeping the oil mixture with a fresh CO_2, as shown in Fig. 5. 3. Sweeping with a new batch of CO_2 makes the CO_2 that is originally mixed with oil from the soaking period to be untraceable. So, the amount of CO_2 used is not accurately recorded.

Another observation is that the CO_2 requirement in the first cycle from the simulation is much less than the available volume. The available volume is the fracture

pore volume plus the core pore volume. In this sample of Tovar's experiment setup with the glass beads as the fractures, the available volume would be 24.1 cc. However, our result show that the first cycle would require 0.6 cc of CO_2 solvent under 3,100 psi and 165°F. Since the amount of CO_2 solvent is not recorded by Tovar, we cannot validate the amount of CO_2 used from our simulation.

The fracture volume is limiting the amount of CO_2/solvent used in each cycle to obtain a certain recovery factor. If so, the contact surface area needs to be increased in the field to enlarge the fracture volume, such as through microfractures, but this is out of the scope of our study. Although we can control the size of the SRV and soaking time, the complex fracture network is too simplified in this stage of study. The next challenge would be to predict the surface contact area to simulate the diffusion process from the fracture to the matrix because the amount of solvent in each cycle of a huff-soak-puff process is limited to the fracture volume and the contact area per cycle, which can limit the recovery factor per cycle.

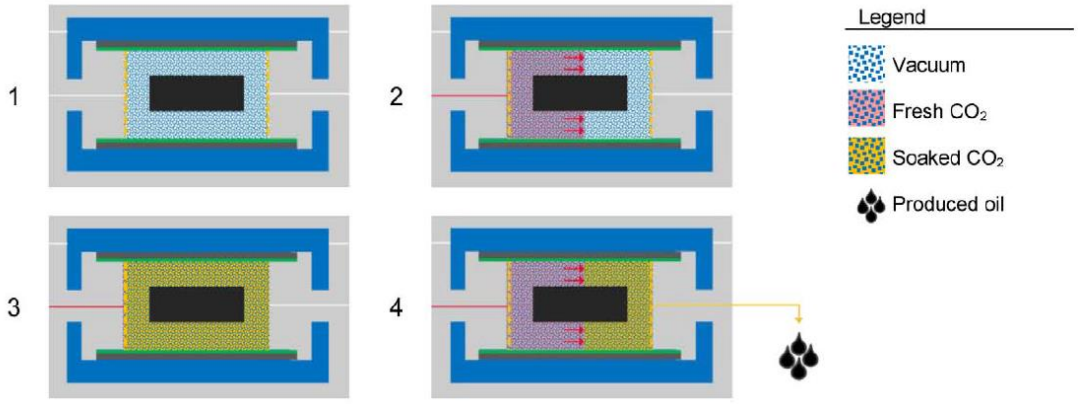

Fig. 5. 3—Adapted figure of the constant pressure huff-n-puff experimental setup by Tovar et al. (2018a). The stages consist of (1) putting the core under vacuum, (2) injecting fresh CO_2, (3) soaking with CO_2, and (4) displacing soaked cored by fresh CO_2.

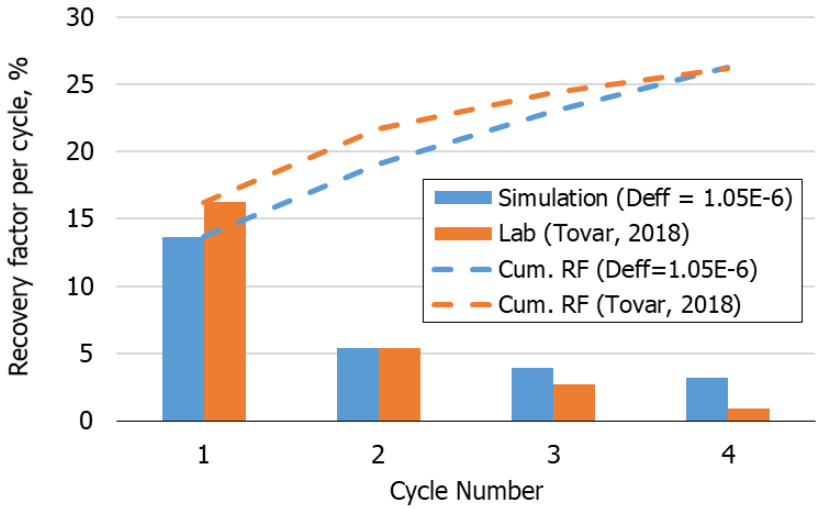

Fig. 5. 4—The recovery factor after 4 cycles of 21 hours soaking time between experimental result from Tovar et al. (2018a) and our matching simulation using an effective diffusion coefficient of 1.05E-6 cm^2/s.

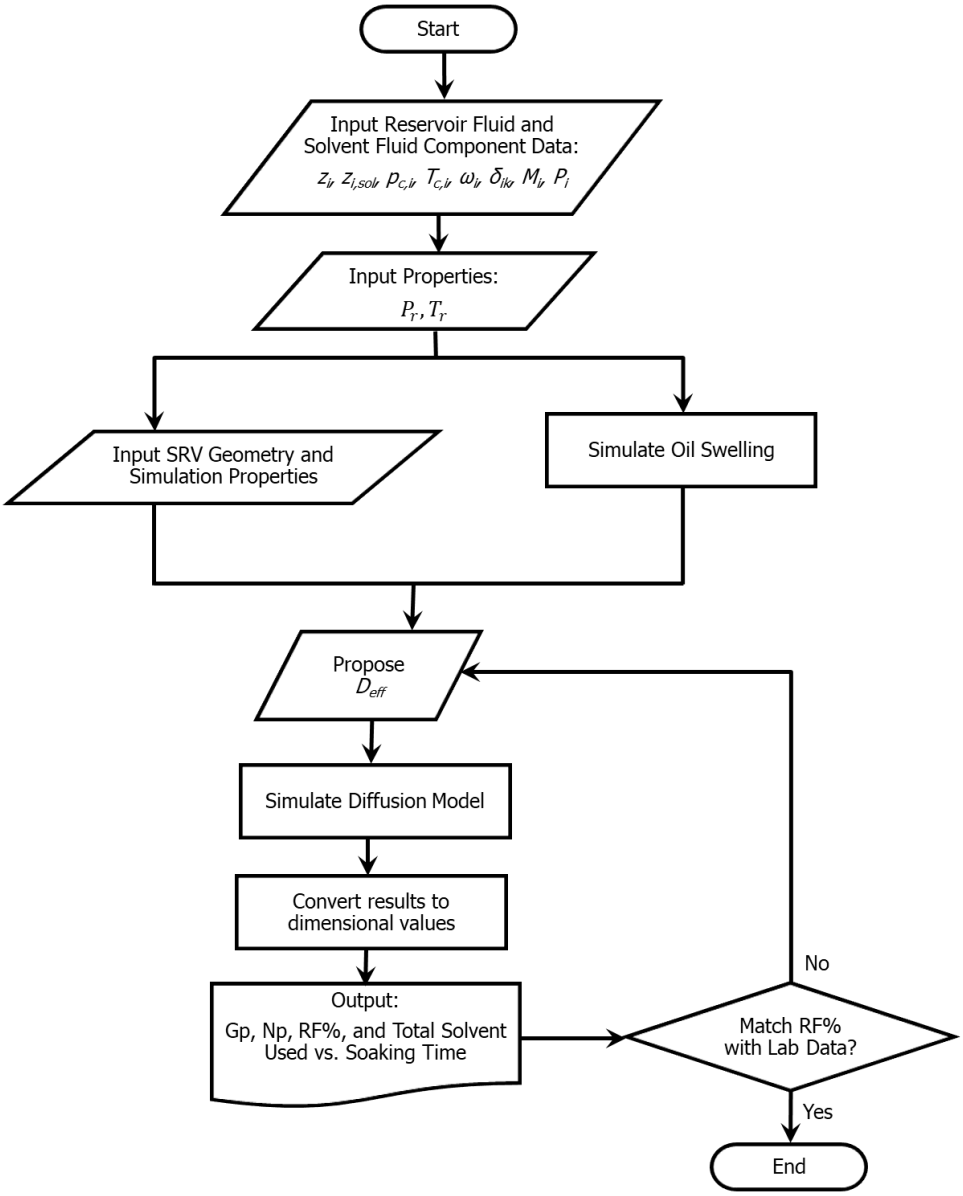

Fig. 5. 5—Condensed flow chart of the diffusion model simulation to estimate the effective diffusion coefficient using an existing laboratory data.

CHAPTER VI

FLUID COMPOSITIONS

Chapter VI includes the fluid compositions and the EOS parameters of the fluids mentioned in this thesis. **Table 6. 1** and **Table 6. 3** are used in Chapter III for the MMP estimates along with the binary interaction coefficients in **Table 6. 2**. The fluid composition and its binary interaction coefficients used in Chapter IV for the diffusion model is listed in **Table 6. 5** and **Table 6. 6**. If the volume shift parameter and Parachor number are not provided by the author, we use correlations by Miqueu et al. (2003) for the volume shift parameter and by Alkan and Luan (1993) for the Parachor.

Table 6. 1—Synthetic oil composition and component properties (Wang and Orr 1997).

Component	z_i	M_i (lb/lb-mol)	$p_{c,i}$ (psia)	$T_{c,i}$ (°F)	ω_i	s_i	P_i
C_1	0.20	16.04	667.8	-116.63	0.0104	-0.1540	77
n-C_4	0.15	58.1	550.7	305.65	0.201	-0.06413	180
n-C_{10}	0.65	134	305.7	652.1	0.490	0.803	505.8

Table 6. 2—Binary interaction coefficients for Synthetic oil and the solvent used in the tests (Wang and Orr 1997).

Component	C_1	n-C_4	n-C_{10}	CO_2
C_1	0.0	-	-	-
n-C_4	0.027	0.0	-	-
n-C_{10}	0.042	0.008	0.0	-
CO_2	0.100	0.1257	0.0942	0.0

Table 6. 3—Eagle Ford volatile oil composition and component properties (Ramirez & Aguilera 2014). All binary interaction coefficients are zero.

Component	z_i	M_i (lb/lb-mol)	$p_{c,i}$ (psia)	$T_{c,i}$ (°F)	ω_i	s_i	P_i
CO_2	0.0091	44.01	1069.9	87.60	0.225	-0.0577	78
N_2	0.0016	28.01	492.5	-232.8	0.040	-0.1356	41
C_1	0.3647	16.043	667.4	-116.9	0.008	-0.1540	77
C_2	0.0967	30.07	708.5	89.70	0.098	-0.1002	108
C_3	0.0695	44.1	615.9	205.6	0.152	-0.0850	150.3
C_4-C_6	0.1255	66.869	532	346.2	0.200	-0.0682	206.9
$C_{7+,1}$	0.2	107.76	430.6	561.1	0.345	-0.0072	337
$C_{7+,2}$	0.1	198.52	263.1	824.8	0.645	0.1191	613.1
$C_{7+,3}$	0.0329	335.11	147	1072.3	1.067	0.2968	1075.16

Table 6. 4—Simplified Eagle Ford volatile oil composition and component properties from Table 6. 3. All binary interaction coefficients are zero.

Component	z_i	M_i (lb/lb-mol)	$p_{c,i}$ (psia)	$T_{c,i}$ (°F)	ω_i	s_i	P_i
C_1	0.35	16.043	667.4	-116.9	0.008	-0.1540	77
C_2	0.10	30.07	708.5	89.70	0.098	-0.1002	108
C_3	0.10	44.1	615.9	205.6	0.152	-0.0850	150.3
Pseudo1	0.12	66.869	532	346.2	0.200	-0.0682	206.9
Pseudo2	0.19	107.76	430.6	561.1	0.345	-0.0072	337
Pseudo3	0.14	198.52	263.1	824.8	0.645	0.1191	613.1

Oil 1 in **Table 6. 5** is an analog of Tovar's experiment. **Table 6. 6** is the binary interaction coefficients used in this thesis. Tovar utilized gas chromatography to identify the fluid composition based on weight percent from his experiment. We then characterized and lumped the fluid components and matched the fluid's density and API gravity.

Table 6. 5—Oil 1 composition and component properties

Component	z_i	M_i (lb/lb-mol)	$p_{c,i}$ (psia)	$T_{c,i}$ (°F)	ω_i	s_i	P_i
Pseudo 1	0.0138	46	616.0	206.1	0.1517	-0.050	229.0
Pseudo 2	0.5672	107	413.2	573.5	0.3379	0.035	342.4
Pseudo 3	0.2648	275	204.9	958. 9	0.7803	0.174	613.9
Pseudo 4	0.0654	402	159.1	1,114.8	1.0420	0.173	803.4
Pseudo 5	0.0887	472	145.7	1,176.1	1.1552	0.180	1,360.3

Table 6. 6—Binary interaction coefficients for Oil 1 and the solvents used in the tests.

Component	N_2	CO_2	Pseudo 1	Pseudo 2	Pseudo 3	Pseudo 4	Pseudo 5
N_2	0.0	-	-	-	-	-	-
CO_2	0.0	0.0	-	-	-	-	-
Pseudo 1	0.1	0.0	0.0	-	-	-	-
Pseudo 2	0.1	0.0	0.0	0.0	-	-	-
Pseudo 3	0.1	0.0	0.0	0.0	0.0	-	-
Pseudo 4	0.1	0.0	0.0	0.0	0.0	0.0	-
Pseudo 5	0.1	0.1	0.0	0.0	0.0	0.0	0.0

CHAPTER VII

CONCLUSIONS AND RECOMMENDATIONS

8.1 Conclusions

Based on the research presented in this thesis, we conclude the following:

- This study enables to quickly predict the performance a gas-assisted EOR project and assess the impact of key design variables, such as injection pressure, solvent/oil combinations, soaking time, and effective diffusion coefficient.
- Our MMP estimations show a trend in decreasing MMP value under confinement and with lower pore diameter by considering capillary pressure in the VLE for confined state. Thus, MMP is expected to be lower in shale reservoirs than in conventional reservoirs.
- In molecular diffusion dominated flow, the diffusivity constant, or effective diffusion coefficient, controls the oil recovery based on the excess volume due to the oil-solvent mixture expansion and dictates the rate of the solvent penetrating into the matrix.
- The diffusion model simulates constant pressure huff-soak-puff experiment where the recovery factor over a soaking period can be matched to estimate an effective diffusion coefficient. This is a practical and fast prediction for the performance of a gas-assisted EOR process dominated by molecular diffusion within the matrix in liquid shale reservoirs.
- PVT and fluid behavior analysis are crucial parts in EOR project, especially in tight plays, because the solvent and oil composition at reservoir condition affect the degree

of deviation of the fluid properties in confined state, such as MMP and oil swelling, from those in bulk state.

- Carbon dioxide acts as a more reliable solvent to increase the oil swelling and recovery and to decrease the MMP rather than nitrogen.

8.2 Recommendations for Future Work

This study is an attempt to understand the fluid transport and behavior, specifically the miscibility condition and the solubility of the solvent-oil mixture, in gas-assisted recovery in liquid-rich shale reservoirs although our research is far from being mature. Thus, we recommend some future work to help this study:

- The computational time to find the MMP with capillary pressure can be minimized. The method to find the next trial pressure can be optimized to approach the MMP faster.
- The robustness of the MMP simulation is also limited since the accuracy drops when the oil is a dead oil or the bubble point is too low. One of the possible solutions is to use negative space flash K-values algorithm from Whitson and Michelsen (1989).
- In addition to matching the oil recovery with experimental data, the solvent used per cycle in the simulation has to be comparable with the experiment data to fully apply our diffusion model. The solvent in the experiment needs to be traceable and recorded.
- It does not take account the oil shrinking, oil evaporation into gas phase, and the two-phase phenomena. The effect of viscosity may be studied as well.
- In scaling up the diffusion process, there are more challenges in the dynamic reservoir condition in the field that complicates the diffusion process, such as:
    - The geometry of the fracture is more complex than our planar model. We would need to consider microfractures and other possible fracture propagation model and increase the contact area without increasing the SRV.
    - The flow in the fracture to the matrix may not be diffusion-dominated due to the presence of pressure gradient.

- Our model would not be valid for reservoirs with high pressure gradient.

REFERENCES

Ahmadi, K., & Johns, R. T. 2011. Multiple-Mixing-Cell Method for MMP Calculations. *SPE Journal* ***16*** (4): 733 - 742. SPE-116823-PA. https://doi.org/10.2118/116823-PA

Alkan, H., & Luan, G. 1993. Estimation of Parachors from Critical Properties. *Society of Petroleum Engineers*. SPE-27633-MS. https://doi.org/10.2118/27633-MS

Araújo, S. V. 2014. *Diffusion and Swelling of CO_2/Light Oil Mixtures using Pressure Decay and CT-Scan*. MS Thesis, University of Campinas. São Paulo, Brazil.

Baek, S., & Akkutlu, I. Y. 2019. Produced-Fluid Composition Redistribution in Source Rocks for Hydrocarbon-In-Place and Thermodynamic Recovery Calculations. *SPE J* ***24*** (3): 1395–1414. SPE-195578-PA. https://doi.org/10.2118/195578-PA

Christiansen, R. L., & Haines, H. K. 1987. Rapid Measurement of Minimum Miscibility Pressure with the Rising-Bubble Apparatus. *SPE Res Eng* ***2*** (4): 523–527. https://doi.org/10.2118/13114-PA

Czernia, B. T. 2018. *Development of Mechanistic Model for Capillary Pressures and Relative Permeabilities to Estimate Oil and Gas Recoveries for Unconventional Reservoirs under Depletion and Gas Injection*. MS Thesis, Texas A&M University. College Station, Texas, USA.

Du, F., & Nojabaei, B. 2019. Estimating Diffusion Coefficients of Shale Oil, Gas, and Condensate with Nano-Confinement Effect. SPE Eastern Regional Meeting, Charleston, West Virginia, USA. 15-17 October. SPE-196589-MS https://doi.org/10.2118/196589-MS.

Earle, S. 2015. *Physical Geology* (1st ed.). BCcampus. https://opentextbc.ca/geology/chapter/20-3-fossil-fuels/

EIA. 2019. *Annual Energy Outlook with Projections to 2050*. U. S. D. o. Energy.

Enick, R. M., Holder, G. D., & Morsi, B. I. 1988. A Thermodynamic Correlation for the Minimum Miscibility Pressure in CO_2 Flooding of Petroleum Reservoirs. *SPE Res Eng* ***3*** (1): 81-92. SPE-14518-PA. https://doi.org/10.2118/14518-PA

Fernø, M. A., Hauge, L. P., Uno Rognmo, A., et al. 2015. Flow Visualization of CO_2 in Tight Shale Formations at Reservoir Conditions. *Geophysical Research Letters* ***42*** (18): 7414–7419. https://doi.org/10.1002/2015GL065100

Fuller, E. N., Schettler, P. D., & Giddings, J. C. 1966. New Method for Prediction of Binary Gas-Phase Diffusion Coefficients. *Industrial & Engineering Chemistry* ***58*** (5): 18-27. https://doi.org/10.1021/ie50677a007

Grogan, A. T., Pinczewski, V. W., Ruskauff, G. J., et al. 1988. Diffusion of CO_2 at Reservoir Conditions: Models and Measurement. *SPE Res Eng* ***3*** (1): 93–102. https://doi.org/10.2118/14897-PA

Hawthorne, S. B., Gorecki, C. D., Sorensen, J. A., et al. 2013. Hydrocarbon Mobilization Mechanisms from Upper, Middle, and Lower Bakken Reservoir Rocks Exposed to CO_2. SPE Unconventional Resources Conference Canada, Calgary, Alberta, Canada. 5-6 November. SPE-167200-MS. https://doi.org/10.2118/167200-MS.

Hoteit, H., & Firoozabadi, A. 2009. Numerical Modeling of Diffusion in Fractured Media for Gas-Injection and Recycling Schemes. *SPE J* ***14*** (2): 323–337. SPE-103292-PA. https://doi.org/10.2118/103292-PA

Jensen, F., & Michelsen, M. L. 1990. Calculation of first contract and multiple contact minimum miscibility pressures. *In Situ* ***14*** (1): 1-17.

Jessen, K., Michelsen, M. L., & Stenby, E. H. 1998. Effective Algorithm for Calculation of Minimum Miscibility Pressure. European Petroleum Conference, The Hague, Netherlands. 20-22 October. SPE-50632-MS https://doi.org/10.2118/50632-MS.

Jessen, K., & Orr, F. M. 2008. On Interfacial-Tension Measurements to Estimate Minimum Miscibility Pressures. *SPE Res Eval & Eng* ***11*** (5): 933-939. SPE-110725-PA. https://doi.org/10.2118/110725-PA

Jia, B., Tsau, J. S., & Barati, R. 2019. A review of the current progress of CO_2 injection EOR and carbon storage in shale oil reservoirs. *Fuel* ***236***: 404-427. https://doi.org/10.1016/j.fuel.2018.08.103

Johns, R. T., Dindoruk, B., & Orr, F. M. 1993. Analytical Theory of Combined Condensing/Vaporizing Gas Drives. *SPE Advanced Technology Series* ***1*** (2): 7-16. SPE-24112-PA. https://doi.org/10.2118/24112-PA

Johns, R. T., Dindoruk, B., & Orr, F. M. 1993. Analytical Theory of Combined Condensing/Vaporizing Gas Drives. *SPE Advanced Technology Series 1* ***1*** (2): 7–16. https://doi.org/10.2118/24112-PA

Leverett, M. C. 1941. Capillary Behavior in Porous Solids. *Trans.* ***142*** (1): 152-169. SPE-941152-G. https://doi.org/10.2118/941152-G

Li, Z., & Dong, M. 2009. Experimental Study of Carbon Dioxide Diffusion in Oil-Saturated Porous Media under Reservoir Conditions. *Industrial & Engineering Chemistry Research* ***48*** (20): 9307-9317. https://doi.org/10.1021/ie900145c

Lie, S. H. 2013. *Diffusion as an Oil Recovery Mechanism During CO_2 Injection in Fractured Reservoirs*. MS Thesis, University of Bergen. Bergen, Norway.

Metcalfe, R. S., Fussel, D. D., & J.L., S. 1972. A Multicell Equilibrium Separation Model for the Study of Multiple Contact Miscibility in Rich-Gas Drives. *SPE J* ***13*** (3): 147–155. SPE-3995-PA. https://doi.org/10.2118/3995-PA

Miqueu, C., Mendiboure, B., Graciaa, A., et al. 2003. Modelling of the surface tension of pure components with the gradient theory of fluid interfaces: a simple and accurate expression for the influence parameters. *Fluid Phase Equilibria* ***207*** (1-2): 225-246. https://doi.org/10.1016/S0378-3812(03)00028-1

Moortgat, J., & Firoozabadi, A. 2013. Fickian Diffusion in Discrete-Fractured Media from Chemical Potential Gradients and Comparison to Experiment. *Energy & Fuels* ***27*** (10): 5793—5805. https://doi.org/10.1021/ef401141q

Orr, F. M., Johns, R. T., & Dindoruk, B. 1993. Development of Miscibility in Four-Component CO_2 Floods. *SPE Res Eng* ***8*** (2): 135–142. SPE-22637-PA. https://doi.org/10.2118/22637-PA

Péneloux, A., Rauzy, E., & Fréze, R. 1982. A Consistent Correction for Redlich-Kwong-Soave Volumes. *Fluid Phase Equilibria* ***8*** (1): 7-23. https://doi.org/10.1016/0378-3812(82)80002-2

Peng, D. Y., & Robinson, D. B. 1976. A New Two-Constant Equation of State. *Industrial & Engineering Chemistry Fundamentals* ***15*** (1): 59-64. https://doi.org/10.1021/i160057a011

Perkins, L. R., & Geankoplis, C. J. 1969. Molecular diffusion in a ternary liquid system with the diffusing component dilute. *Chemical Engineering Science* ***24*** (7): 1035-1042. https://doi.org/10.1016/0009-2509(69)80075-8

Rachford, J. H. H., & Rice, J. D. 1952. Procedure for Use of Electronic Digital Computers in Calculating Flash Vaporization Hydrocarbon Equilibrium. *J Pet Technol* ***4*** (10): 19. SPE-952327-G. https://doi.org/10.2118/952327-G

Ramirez, J., & Aguilera, R. 2014. Factors Controlling Fluid Migration and Distribution in the Eagle Ford Shale. Calgary, Alberta, Canada. 30 September-2 October. SPE-171626-MS https://doi.org/10.2118/171626-MS.

Rao, D. N. 1997. A new technique of vanishing interfacial tension for miscibility determination. *Fluid Phase Equilibria* ***139*** (1-2): 311-324. https://doi.org/10.1016/S0378-3812(97)00180-5

Reid, R. C., Prausnitz, J. M., & Sherwood, T. K. 1977. *The Properties of Gases and Liquids* (3 ed.). McGraw-Hill, Inc.

Renner, T. A. 1988. Measurement and Correlation of Diffusion Coefficients for CO_2 and Rich-Gas Applications. *SPE Res Eng* ***3*** (2): 517–523. SPE-15391-PA. https://doi.org/10.2118/15391-PA

Riazi, M., & Dauber, T. E. 1987. Characterization parameters for petroleum fractions. *Industrial & Engineering Chemistry* ***26*** (4): 755-759. https://doi.org/10.1021/ie00064a023

Scheibel, E. G. 1954. Liquid Diffusivities. *Industrial & Engineering Chemistry* ***46*** (9): 2007. https://doi.org/10.1021/ie50537a062

Sigmund, P. M. 1976. Prediction of molecular diffusion at reservoir conditions. Part I-measurement and prediction of binary dense gas diffusion coefficients. *J. Can. Pet. Technol* ***15***: 48-57.

Stimpson, B. C. 2017. *Impacts of Confined Space on Production from Tight Reservoirs*. MS Thesis, Texas A&M University. College Station, Texas, USA.

Stimpson, B. C., & Barrufet, M. A. 2016. Effects of Confined Space on Production from Tight Reservoirs. SPE Annual Technical Conference and Exhibition, Dubai, UAE. 26-28 September. SPE-181686-MS https://doi.org/10.2118/181686-MS.

Teklu, T. W., Alharthy, N., Kazemi, H., et al. 2014. Vanishing Interfacial Tension Algorithm for MMP Determination in Unconventional Reservoirs. SPE Western North American and Rocky Mountain Joint Meeting, Denver, Colorado. 17-18 April. SPE-169517-MS https://doi.org/10.2118/169517-MS.

Tovar, F. D., Barrufet, M. A., & Schechter, D. S. 2018a. Gas Injection for EOR in Organic Rich Shale. Part I: Operational Philosophy. SPE Improved Oil Recovery Conference, Tulsa, Oklahoma, USA. 14-18 April. SPE-190323-MS https://doi.org/10.2118/190323-MS.

Tovar, F. D., Barrufet, M. A., & Schechter, D. S. 2018b. Gas Injection for EOR in Organic Rich Shales. Part II: Mechanisms of Recovery. SPE/AAPG/SEG Unconventional Resources Technology Conference, Houston, Texas, USA. 23-25 July. URTEC-2903026-MS https://doi.org/10.15530/URTEC-2018-2903026.

Wang, L. S., Lang, Z. X., & Guo, T. M. 1996. Measurement and Correlation of the Diffusion Coefficients of Carbon Dioxide in Liquid Hydrocarbons under Elevated Pressures. *Fluid Phase Equilibria* ***117***: 364-372. https://doi.org/10.1016/0378-3812(95)02973-7

Wang, Y., & Orr, F. M. J. 1997. Analytical calculation of minimum miscibility pressure. *Fluid Phase Equilibria* ***139*** (1-2): 101-124. https://doi.org/10.1016/S0378-3812(97)00179-9

Whitson, C. H., & Michelsen, M. L. 1989. The Negative Flash. *Fluid Phase Equilibria* ***53***: 51-71. https://doi.org/10.1016/0378-3812(89)80072-X

Wilke, C. R., & Chang, P. 1955. Correlation of Diffusion Coefficients in Dilute Solutions. *AIChe* ***1*** (2): 264-270. https://doi.org/10.1002/aic.690010222

Wilson, G. M. 1969. A Modified Redlich-Kwong EOS, Application to General Physical Data Calculations. American Institute of Chemical Engineers 65th National Meeting, Paper No. 15C.

Yu, W., Lashgari, H. R., Wu, K., et al. 2015. CO_2 injection for enhanced oil recovery in Bakken tight oil reservoirs. *Fuel* ***159***: 354-363.

Zhang, K., Dong, X., Li, J., et al. 2016. Effect of Nanoscale Pore Confinement on Multi-Component Phase Equilibrium. SPE/AAPG/SEG Unconventional Resources Technology Conference, San Antonio, Texas, USA. 1-3 August. URTEC-2456191-MS https://doi.org/10.15530/URTEC-2016-2456191.

APPENDIX A

DERIVATIONS

A.1 Diffusion Equation for Cylindrical System

In Chapter IV, we discuss the derivation of the diffusion equation in Cartesian coordinate. This appendix explains the derivation in cylindrical coordinate. Eq. (4. 5) is the equation for diffusion process without the velocity fluctuation in cylindrical system. When the convective term is added, the expanded term of Eq. (4. 8) becomes Eq. (A. 1) for 1-D cylindrical system.

$$\frac{\partial c}{\partial t} = \frac{D_{eff}}{r}\frac{\partial}{\partial r}\left(r\frac{\partial c}{\partial r}\right) - \frac{c}{r}\frac{\partial}{\partial r}(ru) - u\frac{\partial c}{\partial r} \tag{A. 1}$$

The change in velocity in discretized form is defined in Eq. (A. 2).

$$u_{r+\Delta r,t+\Delta t} = \sum_{0}^{r+\Delta r} \Delta u_{r,t+\Delta t} \tag{A. 2}$$

where,

$$\begin{aligned} \Delta u_{r+\Delta r,t+\Delta t} &= \frac{\Delta V_e}{2\pi(r+\Delta r)h\Delta t} \\ &= \frac{\phi \Delta r}{(r+\Delta r)\Delta t}\left[f\left(\frac{c_{r+\Delta r}^{t+\Delta t} + c_r^{t+\Delta t}}{2}\right) - f\left(\frac{c_{r+\Delta r}^{t} + c_r^{t}}{2}\right)\right] \end{aligned} \tag{A. 3}$$

The change in liquid volume (ΔV_e), or the swelling, is described in Eq. (A. 4). The volume expansion of oil is calculated based on the cell pore volume and swelling factor within the cell.

$$\Delta V_e = \phi h[\pi(r+\Delta r)^2 - \pi r^2]\left[f\left(\frac{c_{r+\Delta r}^{t+\Delta t} + c_r^{t+\Delta t}}{2}\right) - f\left(\frac{c_{r+\Delta r}^{t} + c_r^{t}}{2}\right)\right] \quad \text{(A. 4)}$$

The boundary condition and initial condition is shown in Eq. (A. 5) and Eq. (A. 6).

Boundary Conditions:

$$c = c_0 \text{ at } r = r_0$$
$$u = 0, \frac{\partial c}{\partial r} = 0 \text{ at } r = 0 \quad \text{(A. 5)}$$

Initial Conditions:

$$c = c_0 \text{ at } r = r_o, t = 0$$
$$c = c_i \text{ at } r < r_o, t = 0 \quad \text{(A. 6)}$$
$$u = 0 \text{ at } r = 0, t = 0$$

To solve the diffusion equation, we need to utilize dimensionless variable. The definition of each variables is found in Eq. A. 7.

$$\bar{u} = \frac{u}{D_{\text{eff}}/r_0};\ \bar{r} = \frac{r}{r_0};$$
$$\tau = \frac{t}{{r_0}^2/D_{\text{eff}}};\ \bar{c} = \frac{c - c_i}{c_0 - c_i} \quad \text{(A. 7)}$$

Then, we substitute the dimensionless variables into the Eq. (A. 1). The dimensionless form becomes Eq. (A. 8) and Eq. (A. 9).

$$\frac{\partial \bar{c}}{\partial \tau} = \frac{1}{\bar{r}}\frac{\partial}{\partial \bar{r}}\left(\bar{r}\frac{\partial \bar{c}}{\partial \bar{r}}\right) - \frac{\bar{c}}{\bar{r}}\frac{\partial}{\partial \bar{r}}(\bar{r}\bar{u}) - \bar{u}\frac{\partial \bar{c}}{\partial \bar{r}} \quad \text{(A. 8)}$$

$$\frac{\partial \bar{c}}{\partial \tau} = \frac{1}{\bar{r}}\frac{\partial \bar{c}}{\partial \bar{r}} + \frac{\partial^2 \bar{c}}{\partial \bar{r}^2} - \bar{c}\frac{\partial \bar{u}}{\partial \bar{r}} - \bar{c}\frac{\bar{u}}{\bar{r}} - \bar{u}\frac{\partial \bar{c}}{\partial \bar{r}} \quad \text{(A. 9)}$$

The velocity difference becomes Eq. (A. 10). Boundary and initial conditions would be Eq. (A. 11) and Eq. (A. 12).

$$\Delta\bar{u}_{\bar{r}+\Delta\bar{r},\tau+\Delta\tau} = \frac{\phi\Delta\bar{r}}{(\bar{r}+\Delta\bar{r})\Delta\tau}\left[f\left(\frac{\bar{c}_{\bar{r}+\Delta\bar{r}}^{\tau+\Delta\tau}+\bar{c}_{\bar{r}}^{\tau+\Delta\tau}}{2}(c_0-c_i)\right)\right. \\ \left. - f\left(\frac{\bar{c}_{\bar{r}+\Delta\bar{r}}^{\tau}+\bar{c}_{\bar{r}}^{\tau}}{2}(c_0-c_i)\right)\right] \quad \text{(A. 10)}$$

Dimensionless Boundary Conditions:

$$\bar{c} = 1 \text{ at } \bar{r} = 1$$
$$\bar{u} = 0, \frac{\partial\bar{c}}{\partial\bar{r}} = 0 \text{ at } \bar{r} = 0 \quad \text{(A. 11)}$$

Dimensionless Initial Conditions:

$$\bar{c} = 1 \text{ at } \bar{r} = 1, \tau = 0$$
$$\bar{c} = 0 \text{ at } \bar{r} < 1, \tau = 0 \quad \text{(A. 12)}$$
$$\bar{u} = 0 \text{ at } \bar{r} = 0, \tau = 0$$

The recovery from excess swollen volume is calculated as follows:

$$V_{s,total}(P_{res}, T_{res})(t) = \sum_{i=1}^{Ncell}\left(f\left(c_i^t\right)-1\right)\left(r_{i+1/2}{}^2 - r_{i-1/2}{}^2\right) * V_p \quad \text{(A. 13)}$$

$$V_{sol,stored}(P_{res}, T_{res}) = \int_0^1 c(\bar{r}^2)d\bar{r}^2 * V_p \quad \text{(A. 14)}$$

A.2 Finite Difference Method to Solve Diffusion Equation

In Chapter IV, we solve the diffusion equation using a finite difference method. This appendix provides the setup of the matrix for the Cartesian coordinate. We use first forward difference expansion for time discretization in Eq. (A. 15) and centered difference expansion for space discretization in Eq. (A. 16) to Eq. (A. 18).

$$\frac{\partial \bar{c}}{\partial \tau} = \frac{1}{\Delta \tau}(\bar{c}_i^{n+1} - \bar{c}_i^n) + O(\Delta \tau) \tag{A. 15}$$

$$\frac{\partial \bar{c}}{\partial \bar{x}} = \frac{1}{2\Delta \bar{x}}(\bar{c}_{i+1}^{n+1} - \bar{c}_{i-1}^{n+1}) + O(\Delta \bar{x}^2) \tag{A. 16}$$

$$\frac{\partial \bar{u}}{\partial \bar{x}} = \frac{1}{2\Delta \bar{x}}(\bar{u}_{i+1}^{n+1} - \bar{u}_{i-1}^{n+1}) + O(\Delta \bar{x}^2) \tag{A. 17}$$

$$\frac{\partial^2 \bar{c}}{\partial \bar{x}^2} = \frac{1}{\Delta \bar{x}^2}(\bar{c}_{i+1}^{n+1} - 2\bar{c}_i^{n+1} + \bar{c}_{i-1}^{n+1}) + O(\Delta \bar{x}^2) \tag{A. 18}$$

Then, the discretized partial differential equation in Eq. (A. 9) is simplified into Eq. (A. 19).

$$a_i \bar{c}_{i-1}^{n+1} + b_i \bar{c}_i^{n+1} + d_i \bar{c}_{i+1}^{n+1} = e_i, \quad i = 0,1,2,3, \dots, N \tag{A. 19}$$

where the coefficients are defined as in Eq. (A. 20) to Eq. (A. 23).

$$a_i = -\frac{\Delta \tau}{\Delta \bar{r}^2} - \bar{u}\frac{\Delta \tau}{\Delta \bar{r}} + \frac{1}{\bar{r}}\frac{\Delta \tau}{\Delta \bar{r}} \tag{A. 20}$$

$$b_i = 1 + \frac{\Delta \tau}{2\Delta \bar{r}}(\bar{u}_{i+1}^{n+1} - \bar{u}_{i-1}^{n+1}) - \frac{\Delta \tau}{\bar{r}_i}\bar{u}_i^{n+1} + \frac{2\Delta \tau}{\Delta \bar{r}^2} \tag{A. 21}$$

$$d_i = -\frac{\Delta \tau}{\Delta \bar{r}^2} + \bar{u}\frac{\Delta \tau}{\Delta \bar{r}} - \frac{1}{\bar{r}}\frac{\Delta \tau}{\Delta \bar{r}} \tag{A. 22}$$

$$e_i = \bar{c}_i^n \tag{A. 23}$$

We apply the discretization into the boundary condition, which becomes Eq. (A. 24) and Eq. (A. 25). After substituting Eq. (A. 25) into Eq. (A. 19), we have Eq. (A. 26) that derives into Eq. (A. 27) and Eq. (A. 28).

$$\left.\frac{\partial \bar{c}}{\partial \bar{x}}\right|_{\bar{x}=1} = 0 = \frac{1}{2\Delta \bar{x}}\left(\bar{c}_N^{n+1} - \bar{c}_{N-2}^{n+1}\right) \tag{A. 24}$$

$$\bar{c}_N^{n+1} = \bar{c}_{N-2}^{n+1} \tag{A. 25}$$

$$(a_{N-1} + d_{N-1})\bar{c}_{N-2}^{n+1} + b_{N-1}\bar{c}_{N-1}^{n+1} = e_{N-1} \tag{A. 26}$$

$$\bar{c}|_{\bar{x}=0} = 1 = \bar{c}_0^{n+1} \tag{A. 27}$$

$$b_1\bar{c}_1^{n+1} + d_1\bar{c}_2^{n+1} = e_1 - a_1 \tag{A. 28}$$

Therefore, our system of equations become Eq. (A. 29).

$$\begin{bmatrix} b_1 & d_1 & 0 & 0 & 0 \\ a_2 & b_2 & d_2 & 0 & 0 \\ 0 & a_3 & b_3 & d_3 & 0 \\ 0 & 0 & \ddots & \ddots & \ddots \\ 0 & 0 & 0 & a_{N-1} + d_{N-1} & b_{N-1} \end{bmatrix} \begin{bmatrix} \bar{c}_1^{n+1} \\ \bar{c}_2^{n+1} \\ \bar{c}_3^{n+1} \\ \vdots \\ \bar{c}_{N-1}^{n+1} \end{bmatrix} = \begin{bmatrix} e_1 - a_1 \\ e_2 \\ e_3 \\ \vdots \\ e_{N-1} \end{bmatrix} \tag{A. 29}$$